Récupération d'énergie vibratoire large bande à partir de transducteurs piézoélectriques

Yipeng Wu

UNIVERSITÉ DE GRENOBLE

THÈSE

Pour obtenir le grade de

DOCTEUR DE L'UNIVERSITÉ DE GRENOBLE

Spécialité : **Sciences pour L'ingénieur**

Arrêté ministérial : 7 août 2006

Présentée par

Yipeng WU

Thèse dirigée par **Adrien Badel**
et codirigée par **Fabien Formosa & Amen Agbossou**

préparée au sein **du Laboratoire SYstème et Matériaux pour la MEcatronique (SYMME)**
et de **l'école doctorale Science et Ingéniérie des Systèmes de l'Environnement et des Organisations (SISEO)**

Récupération d'énergie vibratoire large bande à partir de transducteurs piézoélectriques

Thèse soutenue publiquement le **7 octobre 2014**,
devant le jury composé de :

M. Claude Richard
Professeur, INSA Lyon, Président
M. Elie Lefeuvre
Professeur, IEF Paris Sud, Rapporteur
M. Dejan Vasic
Maître de conférences (HDR), SATIE Université de Cergy-Pontoise, Rapporteur
M. Mickaël Lallart
Maître de conférences, INSA Lyon, Invité
M. Adrien Badel
Maître de conférences, SYMME Université de Savoie, Directeur de thèse
M. Fabien Formosa
Maître de conférences, SYMME Université de Savoie, Co-Directeur de thèse
M. Amen Agbossou
Professeur, LOCIE Université de Savoie, Co-Encadrant de thèse

Acknowledgements

First of all, I express sincere appreciation to my direct supervisor Adrien Badel, for his careful guidance, technical help, and for sharing with me his experience and expertise in the field of vibration energy harvesting. His original ideals are the engines of the success of this thesis.

To my co-direct supervisor Fabien Formosa, for his continuous encouragement, for his enough patience to review my articles, and for sharing with us his amazing designs in mechanical engineering.

Extend my endless gratitude to my supervisor professor Amen Agbossou, for giving me an opportunity to pursue my doctor degree in University of Savoie and offering me the freedom to research on such an interesting subject.

To my work partner Weiqun Liu, we are working together in the same project for three years. Our academic support and inspiring discussions make us grow a lot in different aspects of scientific research.

I would like to thank my friends in laboratory SYMME (SYstème et Matériaux pour la MEcatronique), for their help in my research and life.

Additionally, I would also like to thank my parents, for their constant support and for always treating my education with the highest importance.

Most heart felt gratitude goes to my wife Lan Li. She has been always loving, supportive, and understanding, for her support and partnership I will be always in debt.

Last but no means least, I am grateful for the reviewers of my thesis, professor Élie Lefeuvre and associate professor Dejan Vasic, for their participation and suggestions on the improvement of my work. I also give my great thanks to professor Claude Richard and associate professor Mickaël Lallart, for their participation and patience in my defense.

The study of my thesis is supported by the ARC Energies from the Rhône-Alpes Region and the French National Research Agency (ANR) under grant no. ARC-11-JS09-002-01 (REViLaBa Project).

Abstract

ENERGY harvesting technology describes the process of converting ambient energy surrounding a system into useful electrical energy through the use of a specific material or transducer. It has the ability to offer the prospect of powering autonomous electronic devices such as wireless sensor nodes without the use of conventional batteries. This thesis focuses on harvesting ambient vibration energy using piezoelectric materials, aims to address the challenge for the high performances of vibration energy harvesting devices (VEHDs) in the case of wideband vibrations.

A typical piezoelectric based VEHD mainly comprises a piezoelectric generator (PEG) that transforms mechanical vibration energy into electrical energy and an energy extraction circuit (EEC) that extracts and stores the generated energy into a storage element. Both of them need to be investigated and specially designed to enhance the power density in wideband vibrations.

Consequently, the thesis starts on studying and modeling a classical linear PEG, then an advanced piecewise-linear PEG using two symmetrical mechanical stoppers is proposed and compared with the linear one. Several key parameters of the proposed PEG are discussed under the forward sweeping mechanical excitation. The different performances between the two PEGs are also presented under three kind of excitation signals.

Hence, the thesis moves to study and model three EECs, which is also the major work of the thesis. Among them, standard EEC is the classical and simplest extraction circuit, but the energy conversion using this circuit is limited and strongly depends on the load. Synchronous electric charge extraction (SECE) EEC enhances the energy conversion of piezoelectric materials, it is also a load-independent circuit whose characteristic is very suitable for wideband vibrations. However, it introduces a complex switch control strategy that cannot be easily self-powered in stand-alone VEHDs. For this reason, we proposed a novel EEC named optimized synchronous electric charge extraction (OSECE) circuit. Not only the electronic circuitry and the switch control strategy are simplified, but also the energy conversion effectiveness is enhanced. The OSECE EEC is a load-weakly-dependent circuit, which is also a favorable characteristic for wideband vibration energy harvesting. The analytical expressions of the harvested powers using the above three EECs are derived and confirmed by the experimental results. Some additional energy losses in the nonlinear EECs are also listed and analyzed by using a simulation software.

Since the OSECE EEC optimizes its switch control strategy, two kinds of self-powered approaches based on the OSECE technique are proposed in chapter 4. One is an electronic approach that uses peak detector (PKD) circuits to drive the switches synchronously; the other is a mechanical approach that integrates mechanical stoppers used as synchronous

switches, so the switches are passively driven by the vibration itself. As a result, the second approach introduces an advanced VEHD which consists of the piecewise-linear PEG due to the mechanical stoppers and the nonlinear OSECE EEC.

Finally, a power management unit which can directly provide the standard direct current (DC) voltage for the electronic modules is presented. A demonstration platform for the vibration energy harvesting technology are developed and evaluated in the laboratory environment.

Résumé

La technologie de récupération d'énergie correspond au processus de conversion de l'énergie ambiante en énergie électrique utile à travers l'utilisation d'un matériau ou d'un transducteur spécifique. Cette énergie ambiante est présente généralement dans l'environnement du dispositif électronique autonome. L'exploitation de cette énergie peut permettre d'alimenter des dispositifs électroniques autonomes, sans l'utilisation de batteries conventionnelles. Parmi les différentes sources d'énergie ambiantes (solaire, flux d'air, flux thermiques, vibrations, etc.), les vibrations ambiantes sont une des sources d'énergie les plus répandue et suscitent ainsi un nombre croissant de travaux de recherche.

Cette thèse porte sur la conception d'un dispositif complet de récupération de l'énergie des vibrations qui est adapté à des vibrations ambiantes large bande à partir de transducteurs piézoélectriques. Le système comprend un générateur piézoélectrique qui transforme l'énergie vibratoire mécanique en énergie électrique et un circuit d'extraction qui extrait et stocke l'énergie générée dans un élément de stockage.

La première partie de la thèse présente une structure linéaire intégrant deux butées mécaniques symétriques. Les performances entre cette structure et une structure linéaire classique sont comparées dans plusieurs cas d'excitation. La raideur linéaire par-morceaux de la structure proposée permet d'agrandir considérablement la largeur de la bande fréquentielle de fonctionnement du générateur piézoélectrique.

La deuxième partie de la thèse propose un circuit d'extraction d'énergie avancé nommé OSECE (Optimized Synchronous Electrical Charge Extraction). Il s'agit d'une amélioration de la technique SECE (Synchronous Electrical Charge Extraction). Le circuit électronique et la stratégie de commande de commutation sont simplifiés, mais l'efficacité de conversion d'énergie est également accrue. En outre, le circuit de OSECE est une interface d'extraction faiblement dépendante de la charge, ce qui est une caractéristique favorable à la récupération d'énergie vibratoire large bande. Afin de rendre le circuit de OSECE capable de fonctionner de façon autonome, la troisième partie de la thèse propose deux méthodes d'autoalimentation dédiées à la technique OSECE. L'une est une approche électronique qui utilise des circuits de détection de maximum pour piloter les interrupteurs électroniques; l'autre est une approche mécanique qui intègre des butées mécaniques exploitées comme interrupteurs mécaniques synchrones, ceux-ci étant entraînés passivement par la vibration elle-même.

Enfin, une plate-forme de démonstration pour le dispositif de récupération de l'énergie de vibration est développée et mise en œuvre au laboratoire.

Contents

Abbreviations

AC	Alternating Current
BJT	Bipolar Junction Transistor
BSM	Buckled-Spring-Mass
CTE	Coefficient of Thermal Expansion
DAC	Digital-to-Analog Converter
DC	Direct Current
DIO	Digital Input/Output
DSSH	Double Synchronized Switch Harvesting
EEC	Energy Extraction Circuit
ESSH	Enhanced Synchronized Switch Harvesting
IC	Integrated Circuit
MEMS	Micro-Electro-Mechanical System
MOSFET	Metal-Oxide-Semiconductor Field-Effect Transistors
MPPT	Maximum Power Point Tracking
OSECE	Optimized Synchronous Electric Charge Extraction
PEG	Piezoelectric Generator
PID	Proportional-Integral-Derivative
PKD	Peak detector
POR	Power-on Reset
RMS	Root Mean Square
RMSHI	Random Mechanical Switching Harvester on Inductor
SCR	Silicon Controlled Rectifier
SECE	Synchronous Electric Charge Extraction
SPICE	Simulation Program with Integrated Circuit Emphasis
SR	Stochastic Resonance
SSD	Synchronized Switch Damping
SSDCI	Synchronized Switch and Discharging to a storage Capacitor through an Inductor
SSHI	Synchronized Switch Harvesting on Inductor
SSHI-MR	Synchronized Switch Harvesting on Inductor using Magnetic Rectifier
UVLO	Undervoltage Lockout
VEHD	Vibration Energy Harvesting Device
WDT	Watchdog Timer
WSN	Wireless Sensor Network

0

Résumé étendu en français

Contents

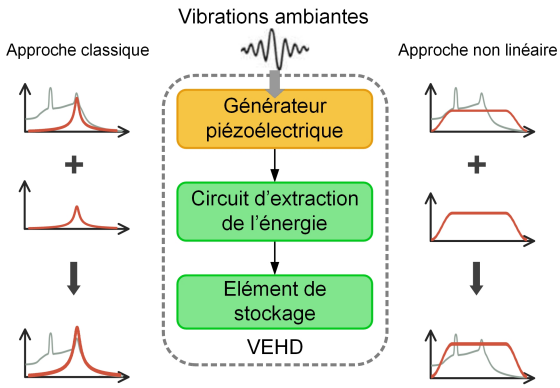

Figure 1: L'architecture d'un VEHD et sa réponse en fréquence en utilisant différentes approches (gris: spectre de la vibration, rouge: réponse du générateur)

0.1 Introduction

0.1.1 Motivation

Les réseaux de capteurs sans fil (WSN) ont de larges applications, telles que la surveillance de la santé des structures mécaniques, le contrôle du trafic, la mesure en milieu industriel, etc.. À l'heure actuelle, presque tous les nœuds dans les réseaux sont alimentés par des batteries électrochimiques. Ces batteries doivent être remplacées ou rechargées dès que l'énergie stockée est épuisée [4, 5]. Cependant, les nœuds de capteurs sans fil sont souvent utilisés dans des endroits isolés ou même intégrés dans des structures, l'accès à ces nœuds peut être très difficile, ce qui augmente considérablement le coût de l'entretien des réseaux. Pour pallier à cet inconvénient, l'exploitation de l'énergie ambiante environnant les nœuds pour créer des sources d'énergie permanentes est étudiée par un nombre croissant de chercheurs [6–10].

Cette technologie est appelée « récupération d'énergie », qui se définit comme un processus par lequel l'énergie des sources ambiantes potentielles (solaire, éolien, vibratoire, thermique, etc.), est convertie en énergie électrique, extraite et stockée pour rendre autonome des appareils électroniques de faible consommation [11]. Cette thèse se concentre sur la récupération de l'énergie de vibration ambiante en utilisant des transducteurs piézoélectriques.

0.1.2 Dispositif de récupération d'énergie vibratoire large bande

La Figure 1 donne l'architecture typique d'un dispositif de récupération d'énergie vibratoire (VEHD) piézoélectrique. Elle comprend essentiellement un générateur piézoélectrique (PEG) qui transforme l'énergie mécanique en énergie électrique et un circuit d'extraction d'énergie (EEC) qui extrait et stocke l'énergie générée.

La mise en œuvre la plus simple d'un VEHDs consiste à utiliser l'approche classique

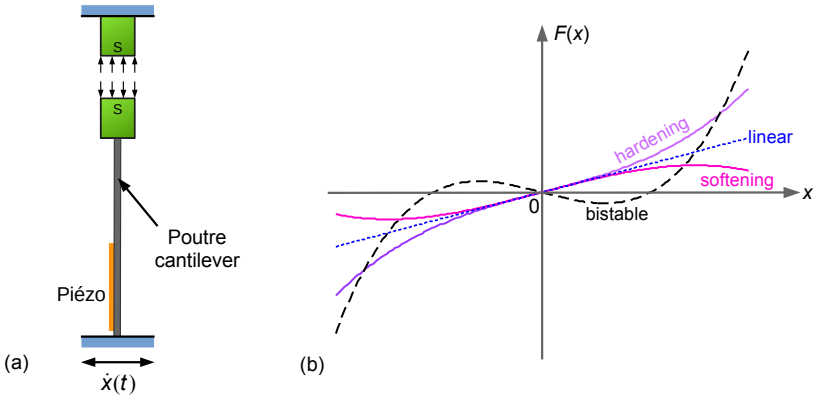

Figure 2: Un PEG non linéaire et l'évolution de la force de rappel en fonction du déplacement

(PEG linéaire plus EEC standard). Cependant, le PEG linéaire atteint d'excellentes performances uniquement lorsque la fréquence de vibration est fixe et correspond à sa fréquence de résonance. Si la fréquence d'excitation dérive légèrement, la puissance récupérée va considérablement diminuer. Comme la majorité des sources de vibrations dans un environnement réel présente des fréquences variables ou des spectres aléatoires, l'approche classique PEG n'est pas toujours optimale [46]. Ce problème existe aussi dans l'EEC standard parce que la stratégie adoptée, qui consiste à adapter l'impédance d'entrée de l'EEC à l'impédance de sortie du PEG afin de maximiser la puissance extraite, est difficile à réaliser. L'impédance de sortie capacitive du PEG dépend en effet de la fréquence des vibrations.

Théoriquement, les approches non linéaires appliquées à la fois pour le PEG et l'EEC peuvent résoudre les problèmes ci-dessus, comme le montrent les courbes schématiques de réponses fréquentielles de la Figure 1, où la vibration ambiante a un spectre de puissance élevée dans une large gamme de la fréquence. Si la fréquence de vibration varie dans cette gamme, le choix des méthodes non linéaires peut permettre d'obtenir une puissance élevée sur une large bande passante.

PEGs non linéaires

Le comportement non linéaire de la raideur d'un PEG peut permettre d'augmenter leur bande passante, permettant une récupération d'énergie efficace dans le cas de vibrations ambiantes large bande. Les approches les plus courantes pour la réalisation d'une telle raideur non linéaire sont les oscillateurs de type Duffing et les systèmes linéaires par-morceaux [46].

La Figure 2(a) montre un PEG utilisant un oscillateur de type Duffing qui se compose d'une poutre encastrée libre équipée d'un élément piézoélectrique, et de deux aimants [67, 72]. L'un est fixé à l'extrémité de la poutre tandis que le deuxième est fixe. Sous

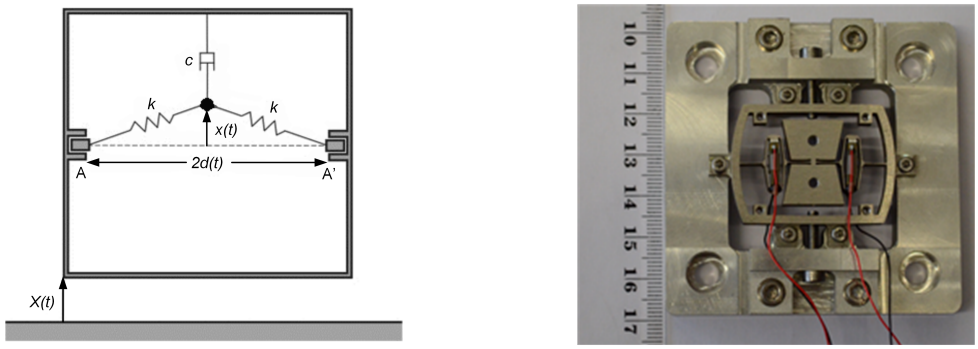

(a) Un modèle schématique d'oscillateur bistable [77]

(b) PEG bistable monobloc et son cadre pour le réglage initial du flambement [79]

Figure 3: Modèle bistable et une de ses mises en œuvre

excitations extérieures, l'aimant à l'extrémité libre de la poutre oscille et est soumis à l'action de l'autre aimant fixe. Dans ces conditions, la force de rappel exercée sur la poutre est une fonction non linéaire de sa flèche comme cela est représenté sur la Figure 2(b). L'effet et la nature de la non linéarité (bistable, raidissant, assouplissant) peuvent être modifiés par la conception du système. Si la force magnétique est attractive, la force de rappel diminue avec la flèche, ce qui détermine un comportement assouplissant; si la force magnétique est répulsive, et la distance entre les deux aimants est relativement grande, la force de rappel augmente avec la déviation, ce qui détermine un comportement raidissant. Ces deux types de forces de rappel conduisent à un seul point d'équilibre stable du système. Un tel oscillateur est appelé oscillateur monostable. Si la force magnétique est répulsive, et la distance entre les deux aimants est relativement proche, la structure aura une raideur négative pour les petites déviations et présente deux équilibres stables. Un tel oscillateur est alors généralement appelé oscillateur bistable [72].

La Figure 3(a) donne un modèle schématique d'un PEG bistable: une masse ponctuelle m avec deux ressorts linéaires de raideur k et de longueur à vide l ($l > d$). Lorsque le cadre est mis en vibration la position de la masse peut passer d'un état stable à l'autre, de manière relativement indépendante de la fréquence des vibrations, ce qui permet d'élargir la bande de fonctionnement [77]. Les premiers dispositifs bistables réalisés par la communauté scientifique mettaient en œuvre des poutres flambées ou des aimants [68, 70, 81, 84]. Cependant, l'établissement de modèles précis pour ces structures est complexe, ce qui rend difficile leur optimisation pour différents environnements. Nous avons proposé un nouveau prototype de PEG bistable basé sur un système masse-ressort, comme le montre la Figure 3(b). L'architecture est compacte et il est facile d'obtenir un modèle équivalent proche du modèle théorique initial représenté sur la Figure 3(a). Par conséquent, le générateur réalisé a pu être modélisé et analysé finement. Nous avons donné une expression normalisée, applicable à n'importe quelle échelle ce qui donne à l'étude un caractère générique. Une stratégie d'optimisation a également été présentée pour divers environnements vibratoires

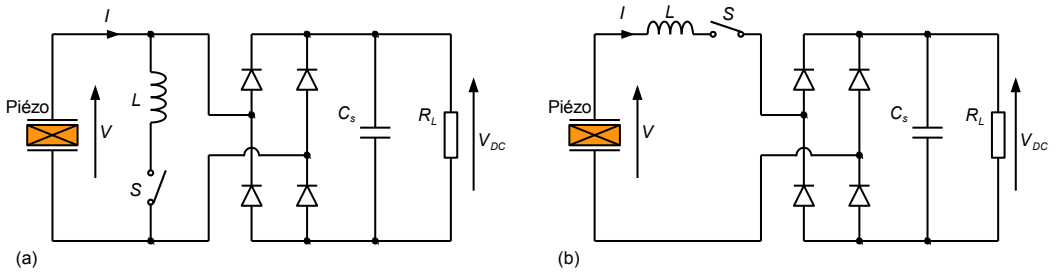

Figure 4: Circuits SSHI: (a) parallèles, (b) série

[69, 79, 85].

Pour un PEG linéaire par-morceaux, la force de rappel est linéaire par-morceaux. Cependant, le comportement de ces systèmes est globalement non linéaire. Une telle raideur linéaire par-morceaux peut être réalisée physiquement en ajoutant des butées mécaniques à un oscillateur linéaire classique, ce qui largi de façon significative la réponse fréquentielle, notamment dans le cas d'un balayage fréquentiel croissant (forward sweep) [86–88]. Les performances d'un PEG linéaire par-morceaux sont étudiées en détails dans la thèse.

EECs non linéaires

L'EEC standard se compose d'un redresseur en pont complet et d'un condensateur de lissage. Il s'agit du circuit d'extraction le plus simple. Toutefois, il présente une faible efficacité d'extraction et ses performances sont dépendantes de la charge électrique R_L. Les techniques d'extraction d'énergie non linéaires à l'aide d'interrupteurs synchrones sont de bonnes alternatives pour améliorer l'efficacité de la conversion d'énergie. Le premier EEC non linéaire à avoir été développé est appelé circuit SSHI (Synchronized Switch Harvesting on Inductor) [94], où un interrupteur synchrone et une bobine sont connectés au PEG en parallèle ou en série [34, 95], comme représenté sur la Figure 4. L'approche SSHI augmente l'amplitude de la tension piézoélectrique et la met en phase avec la vitesse de la vibration, ce qui permet d'extraire plus d'énergie à partir de la source de vibration. Cependant, les performances des circuits SSHI sont toujours fonction de la charge. La puissance maximale est obtenue pour une adaptation d'impédance spécifique.

Pour faire face à cet inconvénient, Lefeuvre et al. ont proposé la technique SECE (Synchronous Electric Charge Extraction), approche qui traite efficacement la question de l'adaptation d'impédance, tout en améliorant l'efficacité de l'extraction d'énergie [107]. Basée sur la technique de SECE, nous avons proposé la technique OSECE (Optimized Synchronous Electric Charge Extraction). Par rapport à la technique SECE, non seulement l'électronique et la stratégie de commande des interrupteurs sont simplifiées, mais l'efficacité de conversion d'énergie est également améliorée [112]. Les performances du circuit proposées ne sont pas totalement indépendantes de la charge, mais beaucoup moins

que les techniques standard et SSHI. Cette faible dépendance peut également être réduite en changeant le rapport de transformation du transformateur utilisé.

Les VEHDs sont des systèmes qui doivent fonctionner de façon autonome, de sorte que les interrupteurs synchronisés doivent être pilotés et alimenté par les VEHDs eux-mêmes. Ces circuits sont ainsi appelés EECs autoalimentés. En raison de la stratégie simple de commande des interrupteurs de l'approche OSECE, deux types d'EECs OSECE autoalimentés sont proposés dans la thèse. L'un est une approche électronique qui utilise un circuit détecteur de crête (PKD) pour piloter un interrupteur électronique synchrone [113]; l'autre est une approche mécanique qui intègre des butées mécaniques utilisées comme des interrupteurs synchrones, de sorte que les interrupteurs sont entraînés de façon passive par la vibration elle-même [122].

Élément de stockage d'énergie

La grande majorité des VEHDs ne peut de fournir de l'énergie de manière constante sur de longues périodes de temps. En outre, la consommation d'énergie du circuit alimenté peut être beaucoup plus élevée que la puissance récupérée pendant de courtes durées (par exemple lors des communications sans fil). Ainsi, l'ajout d'un élément de stockage, qui accumule l'énergie récupérée, puis fournit de l'énergie électrique aux modules électroniques par l'intermédiaire d'une unité de gestion de l'énergie, est nécessaire. Les batteries rechargeables et les condensateurs sont généralement choisis comme éléments de stockage d'énergie.

Cette thèse présente une plate-forme de démonstration des technologies de récupération d'énergie vibratoire, pour laquelle nous avons sélectionné un condensateur électrolytique comme élément de stockage. Une fonction complexe UVLO (UnderVoltage LockOut) et un régulateur de tension à haut rendement sont nécessaires pour fournir une tension stable pour le dispositif alimenté.

0.2 PEGs et leurs modèles théoriques

0.2.1 PEG linéaire

Un PEG linéaire simple peut être constitué par une poutre en porte à faux avec un élément piézoélectrique collé, comme représenté sur la Figure 5. La poutre est capable d'amplifier la vibration ambiante, à condition que le spectre de la vibration d'excitation corresponde à sa fréquence de résonance. Pour un comportement électromécanique linéaire, un système {masse M + ressort K_{S0} + amortisseur D_0 + élément piézoélectrique} à un seul degré de liberté mécanique peut fournir une description pertinente. Bien que ce modèle ne corresponde pas directement à la structure en porte à faux, il donne une description fidèle du comportement de la structure. La simplicité du modèle analytique permet de calculer des grandeurs mécaniques dans le domaine linéaire élastique, ainsi que

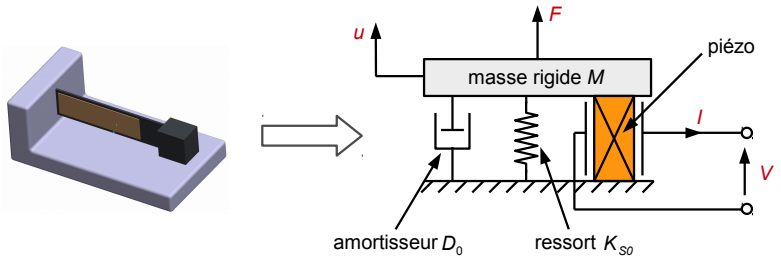

Figure 5: PEG linéaire et son modèle électromécanique

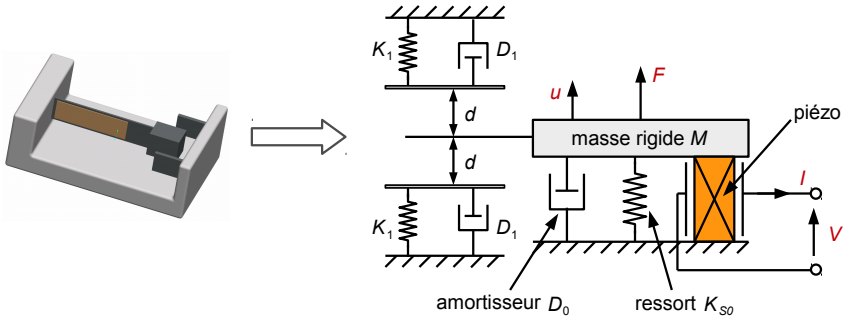

Figure 6: PEG linéaire par-morceaux et son modèle électromécanique

les grandeurs électriques [34].

D'après les équations piézoélectriques, la relation entre les variables mécaniques (u, Fp) et les variables électriques (I, V) peut être exprimée par l'équation 1, où K_p est la raideur en court-circuit des éléments piézoélectriques, α est le coefficient traduisant l'effet piézoélectrique, C_0 est la capacité de l'élément piézoélectrique bloqué. L'équation dynamique du système peut être exprimée par l'équation 2, où K_0 est la raideur équivalente du système en court-circuit $(K_0 = K_{S0} + K_p)$.

$$\begin{cases} F_p = K_p u + \alpha V \\ I = \alpha \dot{u} - C_0 \dot{V} \end{cases} \tag{1}$$

$$M\ddot{u} = F - K_0 u - D_0 \dot{u} - \alpha V \tag{2}$$

0.2.2 PEG linéaire par-morceaux

Dans ce système, le mouvement relatif de la masse rigide peut être divisé en deux étapes. Dans la première étape, le déplacement de vibration u est inférieur à la distance limite d, le système a une raideur K_0 et un amortissement D_0. Lorsque la position de la masse rigide atteint la limite d, l'extrémité de la poutre et l'une des butées sont en contact. Dans cette deuxième étape, la rigidité de l'ensemble devient $K_0 + K_1$ et l'amortissement du système $D_0 + D_1$ [88]. L'équation dynamique de ce PEG linéaire par-morceaux est alors donnée par l'équation 3.

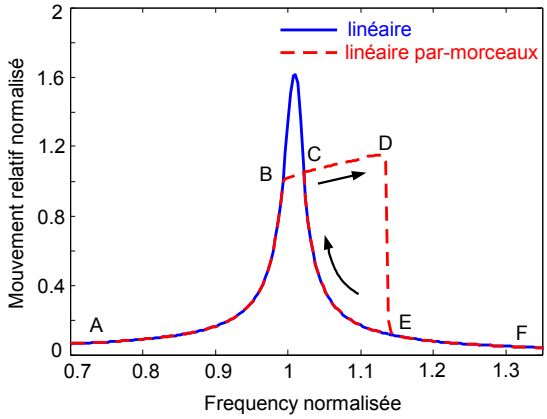

Figure 7: Les réponses en fréquence des PEGs

$$\begin{cases} M\ddot{u} = F - (K_0 + K_1)\,u + K_1 d - (D_0 + D_1)\,\dot{u} - \alpha V & u \geqslant d \\ M\ddot{u} = F - K_0 u - D_0 \dot{u} - \alpha V & -d < u < d \\ M\ddot{u} = F - (K_0 + K_1)\,u - K_1 d - (D_0 + D_1)\,\dot{u} - \alpha V & u \leqslant -d \end{cases} \tag{3}$$

0.2.3 Réponses en fréquence des deux PEGs

Pour obtenir les réponses en fréquence des deux PEGs, les logiciels MATLAB et SIMULINK (The MathWorks©) sont utilisés pour résoudre numériquement les équations dynamiques. Les paramètres ci-dessous sont utilisés pour la simulation:

- L'accélération γ est un balayage fréquentiel croissant d'un signal sinusoïdal de 1g d'amplitude.
- Les éléments piézoélectriques dans le PEG sont en circuit ouvert.
- Le coefficient d'amortissement de la poutre est $\xi_0 = 0.01$, celui des butées est $\xi_1 = 0.02$, le coefficient de couplage piézoélectrique est $k_m = 0.1$.
- Les premières fréquences de résonance de la poutre et des butées sont respectivement de 87 Hz et 200 Hz.

Les courbes de réponse en fréquence sont présentées sur la Figure 7, où les fréquences sont normalisées par la première fréquence de résonance de la poutre cantilever. On voit clairement que dans le cas linéaire, le déplacement de grande amplitude de vibration est limité à une bande passante très étroite, légèrement plus large que les points B à C. Alors que dans le cas linéaire par-morceaux, la bande passante de fonctionnement est considérablement prolongée au-delà du cas linéaire. En outre, trois des paramètres du système linéaire par-morceaux ont une forte influence sur la réponse en fréquence. Ceux sont: le coefficient d'amortissement des butées ξ_1, la rigidité des butées K_1, et la distance limite d [88]. Leurs effets sont étudiés en détails dans la thèse.

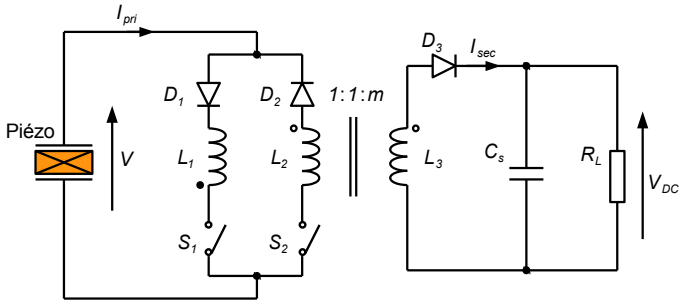

Figure 8: circuit OSECE

0.3 EEC avancée: circuit OSECE

Le circuit OSECE est un circuit dont les performances sont peu dépendantes de la charge, il s'agit d'une caractéristique favorable pour la récupération d'énergie vibratoire. La Figure 8 montre le schéma de l'EEC. Un transformateur à deux enroulements primaires et un enroulement secondaire divise ce circuit d'interface en deux parties. La partie gauche est très similaire au circuit SSDI (Synchronized Switch Damping on Inductor) [96], y compris le signal de commande de commutation. La partie droite est un circuit de charge, qui se compose d'un condensateur de lissage C_s et d'une résistance de charge R_L (qui représente l'impédance d'entrée du circuit à alimenter). En comparant avec l'approche SECE originale, certaines caractéristiques favorables de l'approche de OSECE peuvent être mises en avant:

- Une seule chute de tension due à la tension de seuil de la diode est présente du côté primaire.
- Le pôle négatif de l'élément piézoélectrique et le circuit de charge peuvent avoir une masse commune, ce qui simplifie grandement la mise en œuvre du VEHD (par exemple un capteur piézoélectrique peut partager une masse commune avec l'élément piézoélectrique générateur).
- Au cours de la phase d'extraction d'énergie, une fraction de la charge électrique stockée dans l'inductance circule en retour vers le matériau piézoélectrique par l'intermédiaire de l'interrupteur. Ceci permet d'établir une tension initiale sur l'élément piézoélectrique qui augmente la densité d'énergie électrique produite par le PEG [110].

La Figure 9 montre les formes d'onde typiques de la technique OSECE pour une période d'oscillation complète. Lorsque le déplacement atteint un extremum (maximum ou minimum), les états des interrupteurs sont inversés, les charges électriques accumulées sur l'élément piézoélectrique sont transférées à l'inductance primaire L_1 ou L_2 (Figure 8). Lorsque la valeur du courant I_{pri} atteint sa valeur maximale, toutes les charges électriques ont été extraites et la différence de tension entre les électrodes de l'élément piézoélectrique est nulle. A ce moment, l'interrupteur est resté fermé et la diode est en état de conduction,

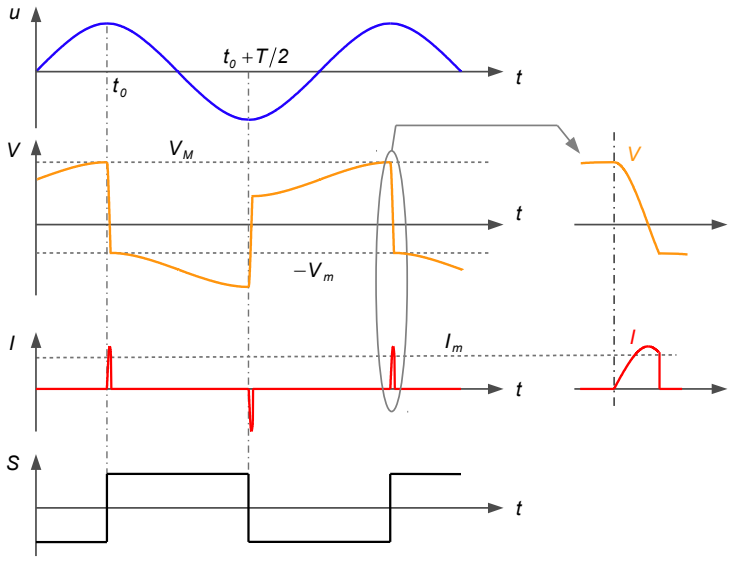

Figure 9: Formes d'onde du déplacement (u), de la tension (V), du courant (I), et du signal de commande de l'interrupteur pour la technique OSECE (S)

l'énergie stockée dans l'inductance primaire L_1 (ou L_2) repart en partie vers le matériau piézoélectrique, avec une polarisation opposée. On obtient ainsi une tension initiale sur l'élément piézoélectrique de manière similaire à la technique d'injection initiale d'énergie [110]. Lorsque la tension aux bornes de l'inductance secondaire atteint V_{DC}, l'élément piézoélectrique est en circuit ouvert de nouveau parce que la diode en série avec l'interrupteur de commutation est polarisée en inverse. L'énergie restante stockée le transformateur est alors transférée vers le circuit de charge via le secondaire du transformateur.

0.3.1 Comparaison et discussion des performances

On suppose pour l'instant que l'amplitude de vibration de la masse inertielle du PEG reste constante quelle que soit la puissance récupérée. Cette hypothèse correspond soit à des structures dont on impose le déplacement, soit à des structures très faiblement couplées ou encore à des structures excitées loin de leurs fréquences de résonance. Dans ces conditions, la Figure 10 donne la puissance récupérée pour les trois EECs considérées en fonction de la résistance de charge. Les traits pleins sont les prédictions théoriques, les points correspondent à des mesures expérimentales. Les courbes montrent que les performances des deux techniques standard et OSECE dépendent de la charge, mais la dépendance de l'approche OSECE est beaucoup plus faible. En raison de la faible efficacité de la conversion d'énergie dans l'EEC standard, la puissance récupérée maximale est de 2 mW. L'utilisation de SECE permet d'augmenter la puissance récupérée (5 mW) et de la rendre plus indépendante de la charge. Même si la puissance récupérée en utilisant OSECE est plus sensible à la charge que dans le cas de la technique SECE, elle est toujours plus élevée, sauf pour des résistances supérieures à 500 kΩ.

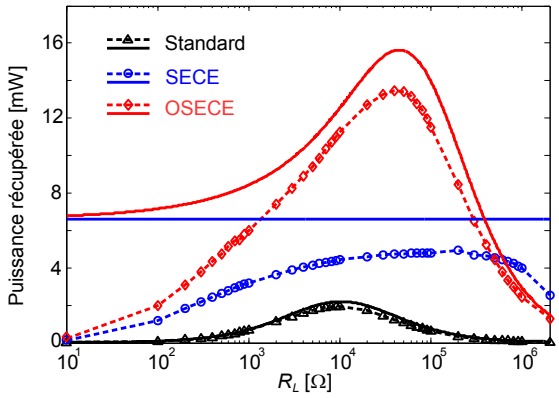

Figure 10: Puissances récupérées en fonction de la résistance de charge

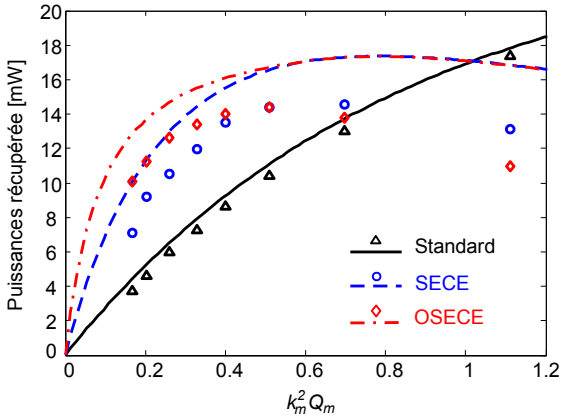

Figure 11: Puissances récupérée en fonction de la figure de mérite $k_m^2 Q_m$

On suppose maintenant que le PEG est excité à sa fréquence de résonance par une force harmonique d'amplitude constante. Dans ce cas, en raison de l'effet d'amortissement provoqué par le processus de récupération d'énergie, l'amplitude de vibration de la masse inertielle est modifiée en fonction du facteur de couplage électromécanique. La Figure 11 donne les puissances récupérées en fonction de la figure de mérite électromécanique du VEHD. Comme prévu, la technique OSECE permet de récupérer une même quantité d'énergie que les autres approches pour une faible valeur de $k_m^2 Q_m$, ce qui implique un besoin plus faible en matériau piézoélectrique pour une même quantité d'énergie (volume et coût optimisés). D'un autre point de vue, si le PEG est une structure électromécanique faiblement couplée (par exemple $k_m^2 Q_m$ est inférieur à 0,52), l'utilisation du circuit OSECE conduit à une plus grande puissance récupérée. Il est intéressant de noter qu'une interface d'adaptation en tension est généralement nécessaire à la suite du circuit standard, qui induirait des pertes supplémentaires qui ne sont pas prises en compte dans cette étude. Ceci renforce encore l'intérêt du circuit OSECE développé.

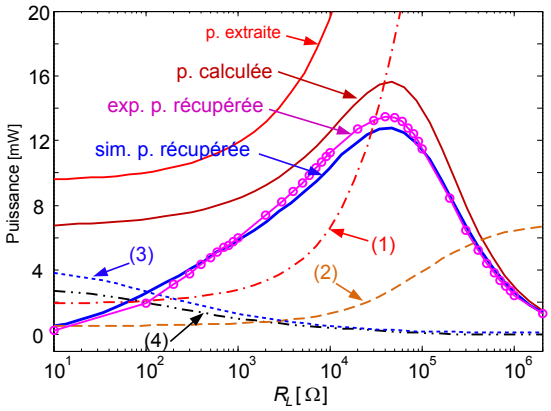

Figure 12: Pertes électriques dans le circuit OSECE: (1) pertes résistives dans le primaire du transformateur, (2) puissance perdue en raison des diodes primaires, (3) perte de puissance due à la résistance série dans l'enroulement secondaire, (4) puissance perdue en raison de la diode du secondaire

0.3.2 Évaluation des pertes électriques dans le circuit OSECE

En comparant les résultats expérimentaux avec les prédictions théoriques sur les Figures 10 et 11, il convient de noter qu'il existe des pertes d'énergie dans le circuit OSECE, en particulier pour une faible résistance de charge. Ces pertes sont principalement dues à la tension de seuil de la diode du secondaire et à la résistance de l'enroulement secondaire du transformateur. Ces comportements non linéaires ne peuvent pas être simplement pris en compte dans le modèle théorique. La Figure 12 montre les résultats de la simulation de l'approche OSECE à l'aide du logiciel SPICE (Simulation Program with Integrated Circuit Emphasis). Les puissances récupérées expérimentales et simulées sont en très bon accord. On voit clairement qu'il existe quatre sources de pertes d'énergie dans le circuit:

- Le facteur de qualité du circuit primaire (pris en compte dans le calcul analytique proposé précédemment).
- Les diodes primaires.
- La résistance série dans l'enroulement secondaire.
- La diode secondaire.

Pour les petites valeurs de résistance de charge, les pertes d'énergie se trouvent principalement sur le côté secondaire du transformateur. Pour les valeurs élevées de la résistance, l'énergie extraite devient très grande, mais une grande partie est perdue par le facteur de qualité Q_I et, dans une moindre mesure, dans la diode du primaire.

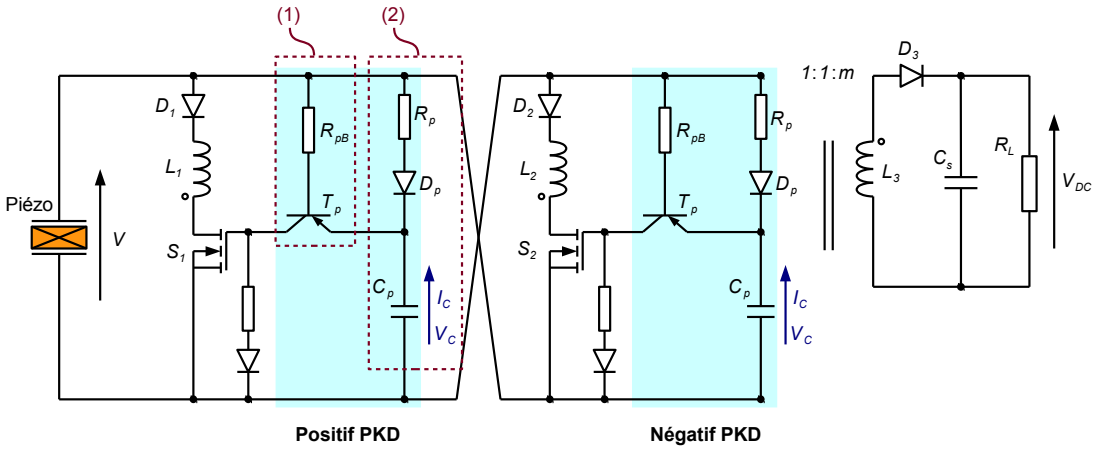

Figure 13: Circuit OSECE autoalimenté électronique: (1) circuit comparateur; (2) détecteur d'enveloppe

0.4 Circuits OSECE autoalimentés

0.4.1 Approche électronique

Selon le principe de la technique OSECE, les interrupteurs S_1 et S_2 sont utilisés pour inverser la tension piézoélectrique aux extrema de déplacement. Les interrupteurs électroniques nécessitent une alimentation et un signal de contrôle pour être correctement pilotés. Dans le circuit électronique autoalimenté proposé, les interrupteurs sont commandés par deux circuits identiques PKD, branchés en parallèle de l'élément piézoélectrique utilisé pour la récupération d'énergie, comme le montre la Figure 13. Chaque PKD est constitué d'un comparateur et d'un détecteur d'enveloppe. Cette approche ne nécessite pas d'éléments piézoélectriques supplémentaires pour générer le signal de commande de commutation. Cependant, il est à noter que l'utilisation de ce type de PKDs induit un retard de phase systématique entre la tension de crête et le temps de commutation réel, les circuits de PKD consomment également une partie de l'énergie extraite, la puissance récupérée finale est logiquement inférieure à celle du circuit OSECE idéal.

Les expressions théoriques du retard de phase de l'interrupteur et la consommation d'énergie du circuit PKD sont déterminées dans la thèse. Elles sont données dans les équations suivantes, où la différence de tension $(V_{max} - V_M)$ correspond à la tension totale de seuil du transistor T_p et de la diode D_p dans le circuit PKD, V_{max} est la tension piézoélectrique maximale.

$$\varphi = \arccos\left(1 - \frac{(V_{max} - V_M)\, C_0}{\alpha u_M}\right) \tag{4}$$

$$E_p = \left(2 + \frac{C_p}{C_0}\right) \frac{1}{2} C_p V_{max}^2 \tag{5}$$

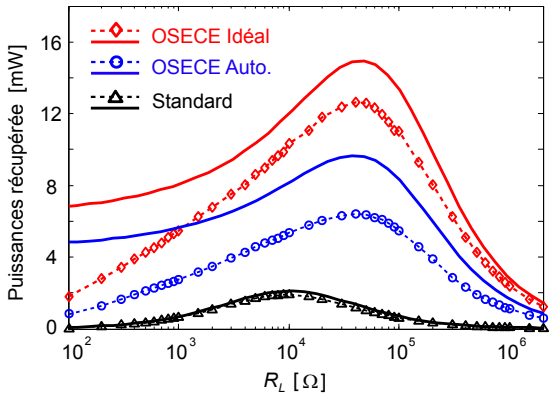

Figure 14: Puissances récupérée en fonction de la résistance de charge

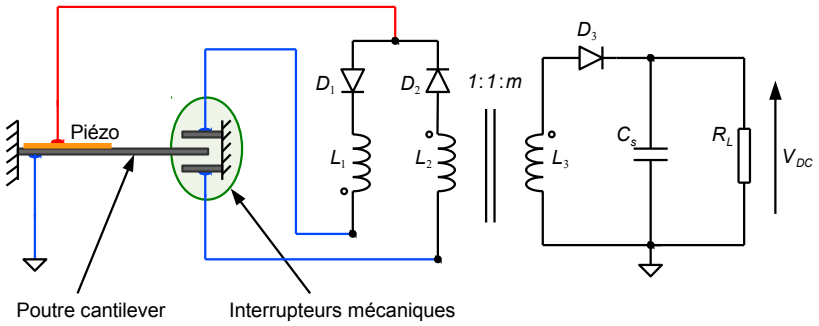

Figure 15: Circuit de OSECE autoalimenté mécanique

La Figure 14 compare les puissances récupérées entre les EECs OSECE idéal et autoalimenté. Les lignes sont les prédictions théoriques et les points sont des mesures expérimentales. En utilisant les approches OSECE, les puissances récupérées restent dépendantes de la charge, tout en étant toujours supérieure à $1,9$ mW (puissance maximale récupérée avec l'EEC standard) pour presque toute la gamme de résistance de charge, ce qui confirme le potentiel de l'approche proposée. Les circuits PKD ne consomment environ que 10% de la puissance extraite, la différence entre les puissances récupérées entre les circuits OSECE idéal et autoalimenté proviennent principalement du déphasage φ.

0.4.2 Approche mécanique

La Figure 15 montre un circuit OSECE autoalimenté mécanique, ainsi qu'un PEG linéaire par-morceaux. La plupart du temps, l'élément piézoélectrique est dans un état de circuit ouvert, de sorte que la tension piézoélectrique est proportionnelle au déplacement de la vibration. Lorsque la poutre entre en contact avec une des butées, le déplacement des vibrations atteint la course limite (maximum ou minimum), de sorte que la tension piézoélectrique est maximale. Etant donné que la poutre et les butées réalisés en matériaux conducteurs forment des interrupteurs mécaniques dans le circuit OSECE, l'interrupteur synchrone correspondant dans le circuit électrique est alors fermé. Les charges électriques

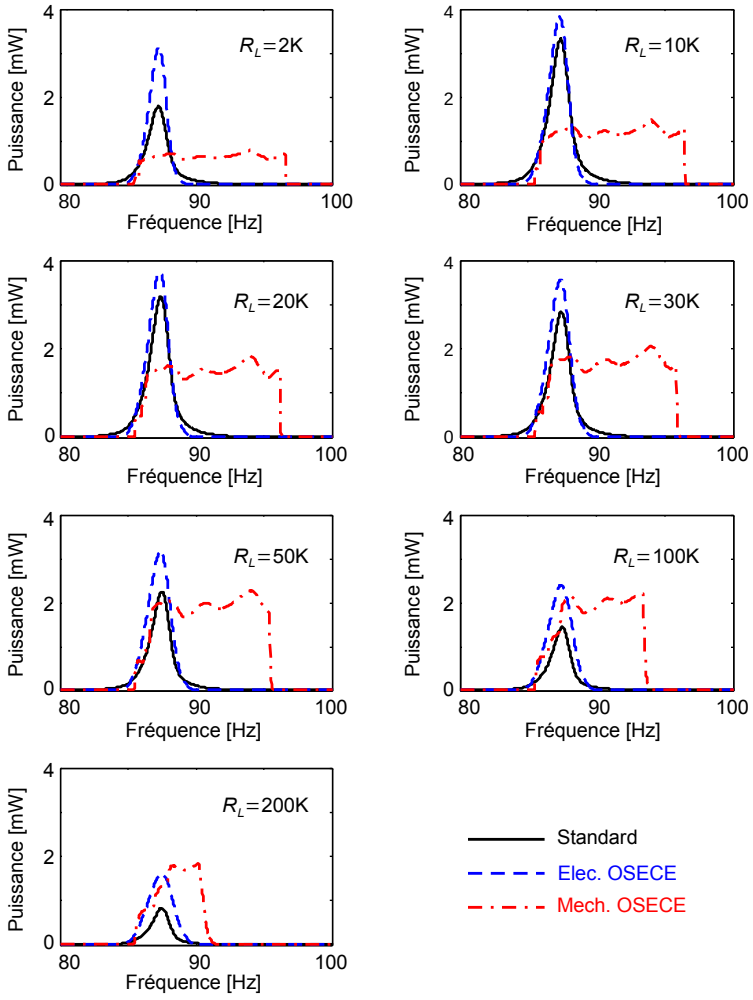

Figure 16: La comparaison des puissances récupérée en utilisant différents EECs

accumulées sur l'élément piézoélectrique sont transmises à l'inductance primaire L_1 (ou L_2), conduisant à la phase d'extraction de l'énergie de l'approche OSECE telle que présentée dans la section précédente. Après cette phase, la butée et la poutre sont toujours en contact (car la butée est élastique et se déforme), mais la diode en série avec l'interrupteur de fermeture devient polarisée en inverse. L'énergie extraite stockée dans le transformateur est ensuite transférée au circuit de charge. En outre, les butées mécaniques, symétriques ici, limitent l'amplitude de vibration du PEG. Ce type de VEHDs se comporte ainsi de manière similaire au cas où la masse inertielle a une amplitude de vibration constante, ce qui est une caractéristique favorable à l'approche OSECE.

0.4.3 Comparaisons expérimentales et discussion

La Figure 16 montre les puissances récupérées dans les cas de trois EECs différents (standard, OSECE autoalimenté de manière électronique, OSECE autoalimenté de manière mécanique) en fonction de la fréquence d'excitation. L'excitation est une accélération sinu-

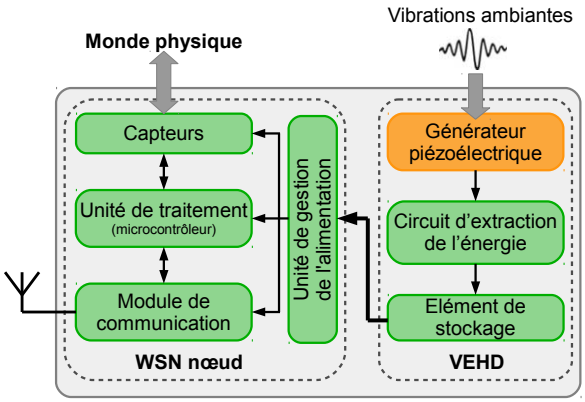

Figure 17: L'architecture d'un nœud de capteurs sans fil autoalimenté

soïdale d'amplitude égale à 1,2g dont la fréquence suit un balayage en fréquence croissant. En comparant les sept graphiques, il est clairement démontré que la puissance récupérée avec l'EEC standard dépend fortement de la charge, alors qu'en utilisant les techniques OSECE, la dépendance est beaucoup plus faible. En outre, la puissance récupérée en utilisant l'approche OSECE autoalimentée électroniquement est supérieure à celle utilisant l'EEC standard; pour l'approche OSECE autoalimentée mécaniquement, même si l'amplitude de la vibration est limitée, une puissance plus élevée peut être récupérée, en particulier lorsque la résistance de charge est supérieure à 50 kΩ. Par ailleurs, en raison de la raideur linéaire par morceaux du PEG, l'approche OSECE autoalimentée de manière mécanique est plus appropriée pour des vibrations à large bande.

0.5 Nœud de capteurs sans fil autoalimenté

L'alimentation de nœuds de capteurs sans fil autoalimentés est l'une des applications de premier plan pour les technologies de récupération d'énergie vibratoire. Dans cette thèse, nous avons donc développé un démonstrateur de nœud de capteurs sans fil autoalimenté afin de montrer la faisabilité d'une alimentation à l'aide d'un VEHD. L'architecture de ce nœud est représentée sur la Figure 17.

0.5.1 Unité de gestion de l'alimentation

Dans le nœud de capteurs, un condensateur électrolytique est choisi pour stocker l'énergie récupérée. Étant donné que, dans le cas général, la puissance récupérée et la puissance consommée évoluent de manière désynchronisée dans le système, la tension aux bornes du condensateur peut varier dans une large plage d'amplitude. Cependant, les sous-modules alimentés dans le nœud doivent fonctionner à une tension d'alimentation nominale, ce qui signifie que la tension d'alimentation doit être stable et à une valeur appropriée. Un régulateur de tension à haut rendement réalise cette fonction. Dans ce nœud, nous avons sélectionné un LTC3588-1 fabriqué par Linear Technology© comme unité de

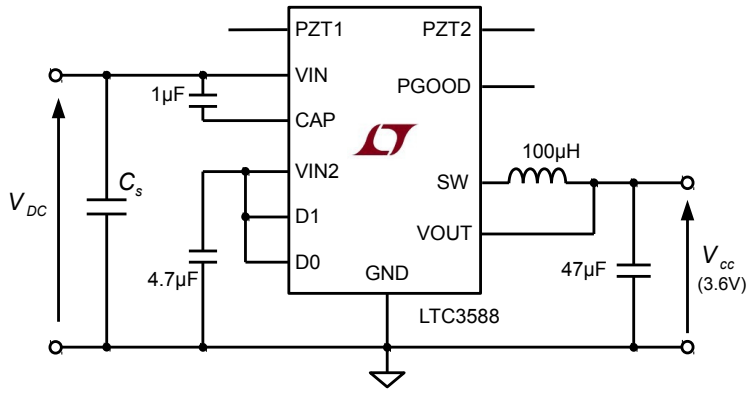

Figure 18: Circuit schématique de l'unité de gestion de l'alimentation

gestion de l'alimentation. Ce circuit est spécialement conçu pour la récupération d'énergie piézoélectrique. Ici, nous utilisons exclusivement les fonctions de UVLO et de régulation de tension intégré dans la puce (un pont redresseur est également présent dans la puce pour implémenter l'EEC standard, mais nous ne l'utilisons pas) [140].

La figure 18 représente le circuit schématique de l'unité de gestion de l'alimentation basée sur le circuit LTC3588-1. Le condensateur C_s est un condensateur électrolytique qui stocke l'énergie obtenue à partir de l'EEC OSECE. La valeur de la capacité de stockage C_s doit être spécialement calculée sur la base de la consommation d'énergie pratique. D0 et D1 sont des bits de sélection de la tension de sortie V_{cc}. Dans cette figure, elles sont reliées au potentiel haut VIN2, ce qui signifie que la tension de sortie est fixée à $3,6$ V; si elles sont reliées à la masse, la tension de sortie sera fixée à $1,8$ V.

Il est intéressant de noter que le circuit LTC3588-1 intègre un EEC standard faible perte. Toutefois, afin de pouvoir récupérer l'énergie de manière plus efficace, dans ce projet, nous utilisons l'EEC OSECE pour remplacer l'EEC standard intégrée. Concrètement, En utilisant la technique OSECE, le condensateur C_s pourra être chargé à une tension bien plus grande avec l'EEC OSECE qu'avec l'EEC standard.

0.5.2 Nœud de capteurs sans fil

Dans le réseau de capteurs simple réalisé, un seul nœud de capteurs sans fil autoalimenté reçoit directement la commande et envoie les données de mesure des capteurs au nœud coordinateur, sans nœud routeur. Après que le nœud de capteurs ait reçu des données de commande du coordinateur, il va éventuellement se reconfigurer, faire l'acquisition des données des capteurs sélectionnés, traiter ces mesures, et envoyer les données physiques vers le nœud coordinateur. Le nœud de capteurs peut mesurer trois grandeurs physiques: l'accélération (suivant les 3 axes), la température et la tension d'alimentation.

Il existe trois principales sources de consommation d'énergie dans un nœud de capteurs sans fil:

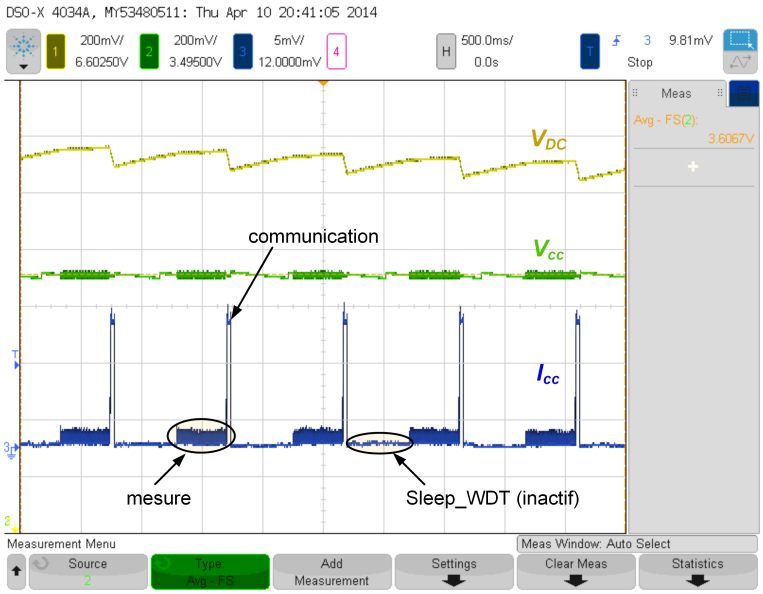

Figure 19: Les formes d'onde des tensions et des courants dans le nœud de capteurs en fonctionnement normal

- Phase inactive, le nœud reste en sommeil ou en mode de repos, n'attend que certaines commandes spéciales à une fréquence très faible.
- Fonctionnement normal en phase active, mesure des échantillons, stockage et traitement éventuel des mesures (calcul de la valeur efficace de l'accélération par exemple).
- Communication par radio en phase active, le nœud reçoit ou envoie des paquets de données au coordinateur.

Grace aux progrès des technologies des semi-conducteurs, la consommation d'énergie en phase inactive est très faible, la deuxième source de consommation d'énergie reste relativement réduite. Cependant, dans le troisième cas, la consommation d'énergie est sensiblement plus élevée.

La Figure 19 montre les formes d'onde du courant de sortie I_{cc} du système de gestion de l'alimentation ainsi que les tensions de sortie et de stockage. Dans cette configuration, le nœud de capteur fonctionne en continu. Pour le calcul de la valeur efficace de l'accélération, le réglage sélectionné est de 200 échantillons mesurés à la fréquence d'échantillonnage de 500 Hz. La durée inactive (Sleep_WDT) entre deux cycles de mesures est établie à 512 ms. On voit clairement que la consommation de puissance maximale dans le nœud est due à la communication sans fil, la valeur du courant absorbé est environ 7 fois supérieure à celle due à la mesure. Pendant le temps correspondant à la communication sans fil, la tension de stockage V_{DC} du dispositif décroit de manière drastique. Afin de concevoir un nœud de capteurs sans fil de faible puissance, il est ainsi nécessaire de réduire la fréquence de la communication sans fil.

La Figure 20 montre l'évolution temporelle des tensions d'alimentation et de stockage

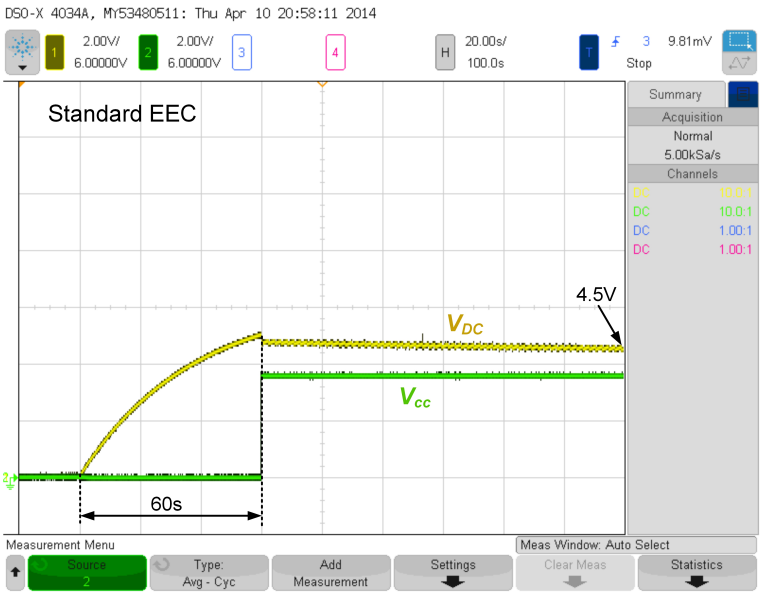

(a) EEC standard

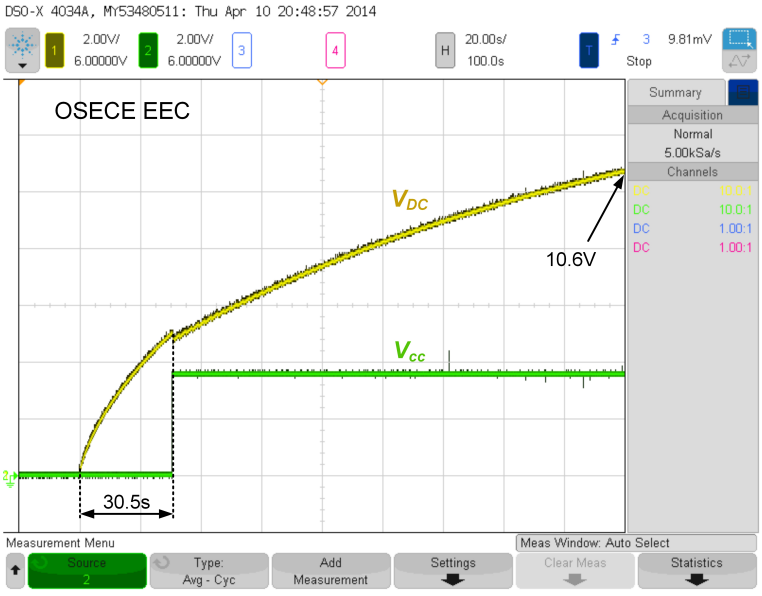

(b) EEC OSECE

Figure 20: Evolution temporelle des tensions d'alimentation et de stockage dans le nœud autoalimenté

dans le nœud de capteurs sans fil autoalimenté. Dans la figure 20(a), l'EEC standard intégré dans le circuit LTC3588-1 est sélectionné. Dans ces conditions, l'unité de gestion de l'alimentation ne peut pas fournir la puissance pendant les 60 premières secondes. Cependant, en utilisant l'EEC OSECE, ce temps de latence est réduit à $30,5$ s environ. De plus, en utilisant l'approche OSECE, la puissance récupérée est toujours supérieure à la puissance consommée, ce qui conduit à une tension de stockage de plus en plus grande, à l'opposé de ce que l'on observe lorsque la technique standard est utilisée. Si la puissance requise du nœud augmente, l'énergie stockée plus grande permettra d'alimenter les modules électroniques pendant une durée beaucoup plus longue.

0.6 Conclusion

Cette thèse étudie principalement une technique d'extraction d'énergie avancée nommée OSECE qui est adapté pour récupérer l'énergie de vibrations large bande. Les puissances récupérées sont théoriquement calculées et discutées. Pour mettre en œuvre le circuit OSECE dans des applications pratiques, deux stratégies pour l'auto-alimentation sont également développées et analysées. Si les interrupteurs synchrones sont réalisés à l'aide d'interrupteurs électroniques, nous choisissons une approche électronique utilisant des circuits PKD. Les circuits PKD permettent de détecter les extrema de déplacement des vibrations et de fournir l'énergie électrique pour piloter les interrupteurs de manière adéquate. En outre, une approche d'auto-alimentation « mécanique » dédiée à OSECE est également proposée. Cette fois, les interrupteurs synchrones sont composés d'une poutre vibrant réalisée en matériau conducteur et deux butées en cuivre. Ces interrupteurs sont commandés de façon passive par la vibration elle-même, ce qui évite le développement de stratégies de commande de commutation complexes, notamment dans le cas de vibrations aléatoires. Enfin, un nœud de capteurs sans fil autoalimentés a été développé, et a permis de démontrer l'intérêt de l'approche OSECE et la possibilité d'utiliser les technologies de récupération d'énergie vibratoire pour l'alimentation de capteurs autonomes communicants.

1

General introduction and literature review

Contents

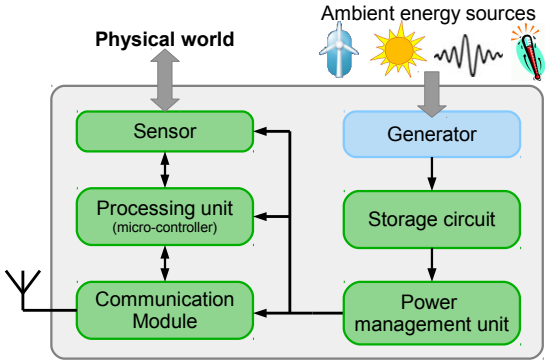

Figure 1.1: Typical architecture of battery-less wireless sensor nodes

1.1 Motivation

"Everything will become a sensor"; this is a global trend to increase the amount of information collected from equipment, buildings, environments, etc., enabling us to interact with our surroundings, to forecast failures or to better understand some phenomena [1]. In recent years, due to the low cost of microprocessors, a transformative advance in the field of sensor technology has been the development of smart sensor systems. The definition of a smart sensor may vary, but typically at a minimum a smart sensor is the combination of a sensing element with processing capabilities provided by a microprocessor [2, 3]. Nevertheless, the intelligence of this kind of smart sensors is still limited in many complex systems. In this case, engineers prefer to preprocess the sampling data in the smart sensor first, and then transmit the sensor data to the much more intelligent processing devices. The simplest solution of transmission is to use signal wires. But if the number of the sensors is huge and widely distributed in a system, this solution becomes awkward and costly. Thanks to the fast development of wireless communications industry and micro-electro-mechanical system (MEMS) design and fabrication, wireless sensor nodes have been proposed to compose the above sensors systems, which are also named wireless sensor networks (WSNs).

At present, almost all of these stand-alone nodes in the networks are powered by electrochemical batteries. Although the power consumption of electronic modules is reducing, the energy storage density of batteries is slowly increasing, these batteries still need to be replaced or replenished as soon as the storage energy is depleted [4, 5]. However, wireless sensor nodes are often used in remote locations or embedded into structures, access to the stand-alone sensor devices can be very difficult, which can significantly increase the maintenance cost of the wireless sensor systems. Moreover, millions of un-recycled batteries used every year also pose a huge negative impact on the environment. To overcome these drawbacks, it therefore becomes necessary to look for a permanent energy source to power these autonomous devices. Scavenging ambient energy surrounding the sensor devices is considered as a practical solution by numerous researchers [6–10].

Table 1.1: Typical data for various energy harvesting sources [12]

Power sources	Power density ($\mu w/cm^3$)	Condition
Solar	15000	Outside
	10	Inside
Temperature	40	Demonstrated from a 5 °C temperature differential
Air flow	380	Air velocity of 5 m/s and 5 percent conversion efficiency
Vibrations	200	10 ∼ 100 Hz, 1g

Figure 1.1 is a typical schematic architecture of battery-less wireless sensor nodes, which is also called self-powered wireless sensor node. In this node, an integrated generator made up of a particular material or transduction mechanism is a key component to convert ambient energy into usable electrical energy. Since the scavenging energy always exists in the surrounding environment, the energy harvesting technologies in stand-alone sensor nodes can provide a permanent power for following electronic modules. Consequently, the continuous lifespan of the sensor node is no longer limited by its storage energy [7].

1.2 Energy harvesting technologies

Energy harvesting is usually defined as a process by which energy is derived from a wide range of environmental sources, converted, extracted, and stored for small autonomous electronic devices. Energy harvester is a small-scale device and normally provides a very small amount of power [11], typically 10 μW ∼ 10 mW.

1.2.1 Ambient energies and their conversion principles

Solar energy, thermal energy, wind energy as well as vibration energy are four major examples that we can envisage as possible sources for harvesting electrical energy from any typical environment, whether indoor or outdoor. However, it is difficult to generalize regarding the typical power levels that are available from the above types of energy source, or which source is most suitable [7]. Fortunately, thanks to the advanced semiconductor technology, the average power consumption of these self-powered devices is usually very low and still keeps on reducing. Energy harvesting technologies that generate a small amount of power create opportunities for more and more applications.

Table 1.1 provides an indication of typical power levels along with the conditions assumed. From the data, it is clear shown that solar power in outdoor conditions is hard to beat. But from the view of the authors, the choice of energy source and method of implementation strongly depends on its application (the surrounding environment, the average

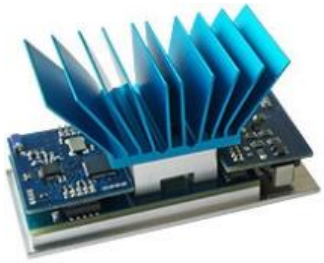

Figure 1.2: TE-power node of Micropelt

power consumption of the self-powered device, etc.) [7, 12].

Solar energy is probably the most well known energy source. The most prominent technologies of harvesting solar energy is to use converters based on photovoltaic effect [13, 14]. The converters are mainly composed of photovoltaic materials which convert solar radiation into direct current (DC) electricity. Texas Instruments Incorporated© already launched a solar energy harvesting development kit to help create a perpetually powered WSN*. However, the design of a solar energy harvester still involves complex tradeoffs due to the interaction of several factors such as the characteristics of the solar cells, average power consumptions in practical applications, extreme weather conditions, etc. A lot of advanced technical solutions are being proposed by the researchers who focus on this field [13, 15–17].

The convenient way for harvesting ambient thermal energy is the use of converters based on Seebeck effect [18]. The converters are made of solid state materials that have the property of providing a DC voltage when a thermal gradient is applied. But the voltage due to Seebeck coefficient is very low, typically in the order of 10^{-4} V/°C for the most common materials [19, 20]. Thus it is necessary to connect several thousand thermoelectric rods in series in order to obtain a higher output, a bulky heat sink is also usually required to maintain a thermal gradient. Figure 1.2 shows a self-powered wireless sensor node evaluation unit** launched by Micropelt©. Although this evaluation unit is the third generation product, the heat sink takes a huge part of the device, that enlarges the whole volume very much.

Wind energy has been harvested for more than one hundred years by means of large-scale wind turbines to generate orders of magnitude larger power output as compared to the power requirement of stand-alone sensor devices [21]. Wind energy is firstly converted into rotational kinetic energy and then electromagnetic transducers are used to generate electrical energy. For low-power electricity generation by harvesting wind energy, an evident approach is therefore to miniaturize wind turbine configurations, as done by Priya et al. [22], Myers et al. [23], Rancourt et al. [24], and Xu et al. [25].

*http://www.ti.com/tool/ez430-rf2500-seh

**http://www.micropelt.com/applications/te_power_node.php

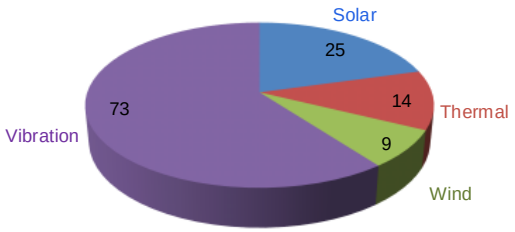

Figure 1.3: Pie chart of the published articles for each source of energy

Vibrations can be found in numerous applications including human motions, industrial plant equipment, transports such as automobiles, trains and aircrafts, and large-scale structures such as high buildings and bridges [8]. Converting the mechanical energy from ambient vibrations into electrical energy is performed by a transducer. Among these transduction systems, current solutions are mostly accomplished via electrostatic [1, 26], electromagnetic [27, 28], or piezoelectric methods [29–34]. However, the conversion efficiency depends, to a certain extent, on the applications and on the specific operating conditions.

1.2.2 Future trend of vibration energy harvesting

Although the energy harvesting selection of the above energy sources depends on the application (e.g. in direct sunlight condition, harvest solar energy is an excellent choice), vibration energy seems to be the most prevalent source of energy for energy harvesting applications and attract an increasing number of researchers.

According to the database of ScienceDirect*, publications with energy harvesting as keywords increased significantly in the last ten years. There are total 528 published articles which contain "energy harvesting" in the list of keywords since 2004. Selecting these articles as a sampling data, searching "vibration", "solar", "thermal" and "wind"/ "air flow" only in the field of keywords gets a total of 121 articles. Finally, Figure 1.3 gives the published numbers of the articles in each source of energy, respectively. It is clearly shown that more than half of the articles have "vibration" & "energy harvesting" in the list of keywords [30].

In addition, there exists a trend that some researchers prefer to convert thermal and wind energies into vibration energy first, and then transfer vibration energy into electrical energy in recent years. Though the energy conversion steps are doubled, they think that using vibration energy harvesters to generate electrical energy is more suitable for low-power, small-scale electronic devices.

As a thermal to electricity converter, a Seebeck device usually requires quite expensive materials such as bismuth telluride, developing a flexible device is rather complicated. Moreover, a heat sink which is an electrically passive component takes the biggest part

*http://www.sciencedirect.com/

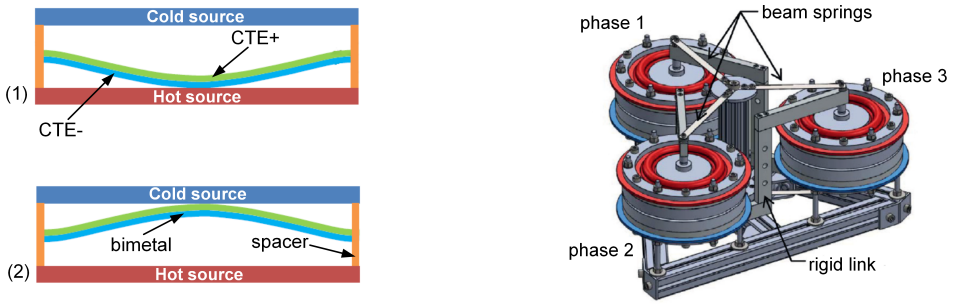

(a) Bimetal-based heat enegine [35]

(b) Free-piston Stirling engine [37]

Figure 1.4: Prototypes of the thermo-mechanical devices

of the volume. Due to these drawbacks, Boisseau et al. proposed a bimetal-based heat engine which converts a thermal gradient into mechanical oscillations [35]. A bimetal is made of two strips of different metals with different coefficients of thermal expansion (CTE) which are joined together. The CTE difference enables flat bimetallic strips to bend when heated up or cooled down, making bimetal transducers that convert temperature changes into mechanical movements. In the engine, they select a curved bimetal clamped in a cavity with hot source on the bottom and a cold source on the top, as shown in Figure 1.4(a). Two electrostatic converters integrated in the engine generate the electrical energy synchronously when the capacitances are changed due to the movement of the bimetal used as the two counter-electrodes. Puscasu et al. also proposed a similar bimetal-based heat engine hereafter, but they selected the piezoelectric material as a vibration-to-electricity converter [36]. At the same time, Formosa et al. proposed a prototype of a free-piston Stirling engine as shown in Figure 1.4(b). The device has a simple architecture and potentially high thermodynamic performances [37]. The miniaturization law for the structure has also been thoroughly studied in the reference [38].

Wind turbines based on electromagnetic conversion are efficient generators at large scales. However, reducing the size of a turbine to miniature scales disproportionally degrades its aerodynamic performance, increases its cut-in wind speed*, significantly lowers its efficiency, and in general complicates both its design and manufacturing [39]. For these issues, researchers have recently considered directly exploiting aeroelastic vibrations for converting wind energy into electrical energy. Some simple and scalable structures have been proposed as an alternative to small-scale wind turbines[21, 39–41]. Most of them are based on simple cantilevers with various tip body shapes attached to their free end, similar as that shown in Figure 1.5. When the uniform and steady air flows through the tip body at a sufficiently high flow speed, the wake of the tip body consists of a staggered array of traveling vortices known as "Karman Vortex Stree". An aerodynamic forces added on the tip body and a large temporal pressure fluctuations caused by vortex shedding di-

*Cut-in speed is the minimum wind speed at which energy can be harvested from the device.

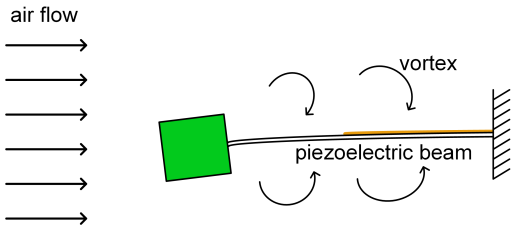

Figure 1.5: Simple wind energy harvester using piezoelectric converters

rectly make the cantilever beam vibrate. The piezoelectric layers bonded on the beam are strained dynamically due to the vibration, yielding the electrical energy is generated.

1.3 Wideband vibration energy harvesting device

As vibration energy harvesters, piezoelectric and electromagnetic generators present the advantage of harvesting high power levels with simple implementations [42]. This thesis focuses on piezoelectric conversion mainly because of the following reasons: piezoelectric materials can directly convert applied strain energy into usable electric energy; can be easily integrated into a small-scale system; and have high energy densities [43].

Figure 1.6 gives the typical architecture of a piezoelectric based vibration energy harvesting device (VEHD). It mainly comprises a piezoelectric generator (PEG) that transforms mechanical energy into electrical energy and an energy extraction circuit (EEC*) that extracts and stores the generated energy into a storage element.

The simplest implementation of VEHDs is to use conventional approach (linear PEG plus standard EEC). The most common geometric configuration used in the design of the linear PEG is a cantilever beam with bonded piezoelectric layers, and the standard EEC is composed of a full-bridge rectifier and a smoothing capacitor. The cantilever PEG is a classical oscillator that offers a very large average strain provided that the excitation vibration spectrum matches its resonance frequency [44]. It is also the simplest electromechanical oscillator which is easily realized and well suited for MEMS manufacturing [45]. However, the linear PEG only achieves its excellent performance when the vibration frequency is a stable value and matches its resonance frequency. If the excitation frequency slightly shifts, the harvested performance will dramatically decrease. Since the majority of practical vibration sources in the environment are present in frequency-varying or random patterns, the linear PEG is not always suitable to ambient vibrations [46]. This issue also exists in the standard EEC. From the previous literature [47], it can be seen that the extracted power directly using the standard EEC is usually limited and dependent on the load impedance. To maximize the extracted power, the matching impedance strategy that consists in matching the input impedance value of the EEC to the output impedance of the PEG is considered. However, the piezoelectric output impedance depends on the vibration

*EEC is also called interface circuit in most literature.

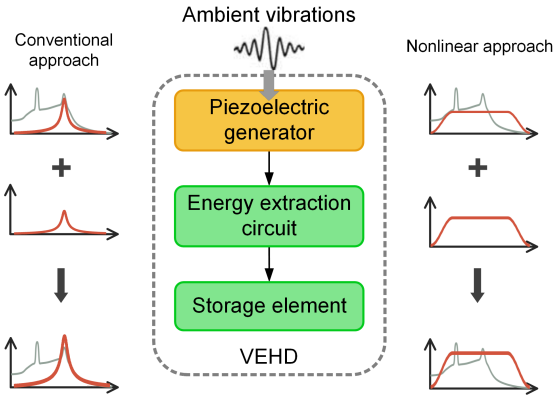

Figure 1.6: The architecture of a VEHD and its frequency response using different approaches

frequency due to its capacitive behavior, and the EEC cannot tune its input impedances sensitively, this matching impedance strategy is also inappropriate to wideband vibrations.

Theoretically, nonlinear approaches applied in both the PEG and the EEC are possible to solve the above issues existing in ambient wideband vibrations. See the theoretical frequency response curves shown in Figure 1.6, where the ambient vibration has a high power spectrum in a large range of the frequency. If the vibration frequency varies in this range, selecting the nonlinear approaches can make the VEHD always obtain the high power in a wide bandwidth. To achieve this goal, Chen et al. [48] and we [49] already proposed the experimentations which combine these two nonlinear approaches. Recent results show that, in some cases, for instance the system is not sensitive to the damping due to the energy harvesting process, the energy conversion of the proposed experimentations is greatly improved.

1.3.1 Piezoelectric generator

This subsection presents a main review of recent advances in PEGs suited for wideband vibrations. The state-of-the-art techniques in this field, covering resonance frequency tuning, multimodal energy harvesting, and nonlinear energy harvesting configurations, are introduced as well as the corresponding PEGs [46]. Among them, nonlinear energy harvesting techniques are specially presented.

Resonance frequency tuning techniques

In order to match a varying excitation frequency, researchers proposed the resonance frequency tuning techniques applied to the different electromechanical structures. The tuning process can be implemented actively or passively [50].

Figure 1.7(a) shows a passive method to tune the resonance frequency of the cantilever

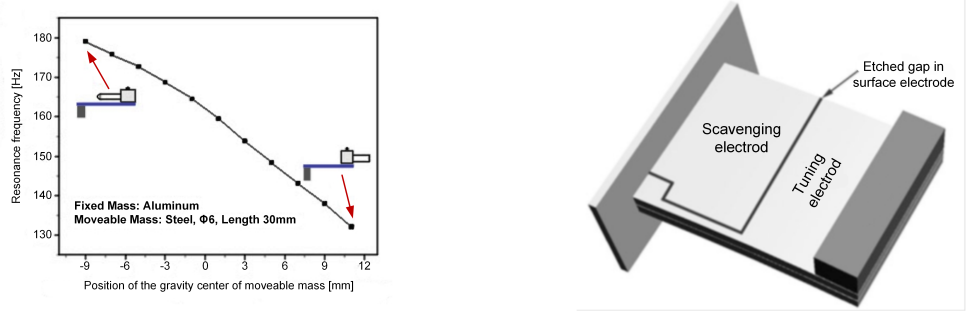

(a) Resonance frequency as a function of mass gravity center position [51]

(b) Piezoelectric resonance frequency tuning technique [50]

Figure 1.7: Resonance frequency tuning techniques used in linear PEGs

beam proposed by Wu et al. [51]. The tip mass of the beam is composed of a fixed part and a moveable part, the gravity center of the whole mass can be adjusted by driving the movable screw. This method amounts to change the equivalent length of the beam that has direct relationship with the resonance frequency. In addition, the mass of the fixed part should be much lighter than that of the movable screw, so that the adjustable distance of the mass gravity center can be increased. In this prototype, the adjustable resonance frequency range covers 130 $\sim$ 180 Hz by tuning the gravity center of the tip mass up to 21 mm, as illustrated in the figure. Such passive tuning technique was also proposed by Eichhorn et al. [52]. They presented a cantilever tunable structure by applying prestress at its free end. This method amounts to change the equivalent stiffness of the beam that is proportional to the squared of the resonance frequency. Nevertheless, these kinds of tunable designs usually require manual adjustment of the system parameters, which makes it difficult to implement automatically during operation.

One kind of active methods to tune the resonance frequency of the structure is shown in Figure 1.7(b). The electrode of the piezoelectric element is etched to create a scavenging and a tuning part. The active control voltage added on the tuning electrode can tune the equivalent stiffness of the structure, making the resonance frequency of the beam match the excitation frequency [50]. Although the required control power is larger than the harvested power in the proposed prototype, this simple active tuning idea is attracted by many researchers. Lallart et al. proposed a similar active resonance frequency tuning technique in which the self-detection of frequency changed and the self-actuation were implemented. This system was estimated to achieve a positive net power output in a range of 8.1 Hz near the original resonance of 112 Hz [53]. Generally speaking, active tuning methods using piezoelectric material are automatic and very convenient, but they provide the small tenability, and require continuous power input for resonance tuning, the tuning power may outweigh the harvested power in some cases (e.g. excitation frequency is far away from the original resonance of the structure).

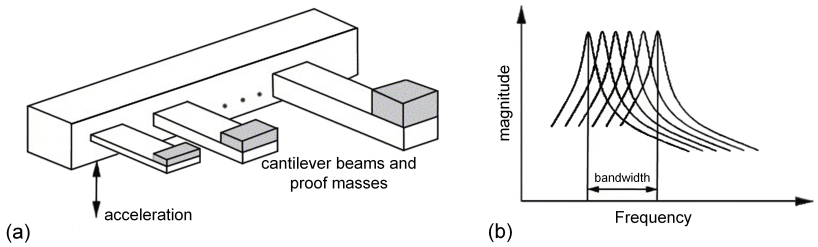

Figure 1.8: Cantilever arrays structure and its voltage-frequency response [61]

Multimodal energy harvesting techniques

Until now, resonance frequency tuning techniques are not efficient under some ambient vibrations whose frequencies are randomly or rapidly varying: passive techniques are not flexible; active techniques require additional power input which significantly reduces the harvested power. In these cases, multimodal energy harvesting techniques can provide a better performance. The piezoelectric harvesters are usually multiple degree-of-freedom systems or distributed parameter systems. Thus one of the vibrational models of the PEGs can be excited when the driving frequency approaches the corresponding natural frequency. If multiple vibration modes of the PEGs are utilized, a wider bandwidth can be covered for efficient energy harvesting [46, 54, 55].

Roundy et al. first proposed the idea of multiple degree-of-freedom system incorporating multiple proof masses attached on a clamped-clamped beam to achieve wider bandwidth [12]. Other than this work, most of the reported studies in the literature exploit a multimodal harvester with a cantilever beam configuration, in which the first two bending modes were used [56–58]. Nevertheless, the multiple bending modes of these PEGs are usually far away from one another and thus the effective bandwidth is discrete. Some advanced structures such as L-shaped beams [33], cut-out beams [59], and cantilevered meandering beams [60] can be considered to achieve close and effective resonant peaks, but only the first two modes can usually contribute to effective energy harvesting which also limits the bandwidth.

Different from the multiple modes of a single beam, cantilever arrays integrated in one PEG can achieve continuous wide bandwidth if the geometric parameters of the harvester are appropriately selected. Figure 1.8 shows one classical structure of these kinds of PEGs, as well as its voltage-frequency response [61]. The PEG consists of piezoelectric cantilevers of various lengths and tip masses attached to a common base. It is capable of resonating at various frequencies by properly selecting the length and tip mass of each beam and thus provides high voltage over a wide frequency range. Such similar devices were also proposed by Xue et al. [62], Ferrari et al. [63], Liu et al. [64]. However, in such array configuration, only one cantilever or a subset of the array is active and effective for energy harvesting; the power density of the whole PEG is affected. Moreover, due to the phase difference between

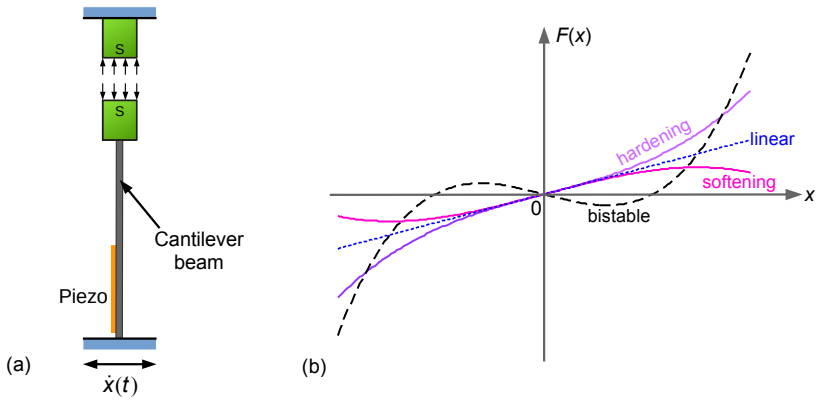

Figure 1.9: A classical nonlinear PEG and its variation of the restoring force due to the nonlinearity

cantilevers, more sophisticated EECs are required than that for a single-mode structure.

Nonlinear energy harvesting techniques

More recently, the intentional introduction of nonlinearities into the design of PEGs has been a topic that received wide attention. The nonlinear behavior may extend the bandwidth, allowing for efficient energy harvesting under the ambient wideband vibrations. As reported in the available literature, nonlinearities in PEGs are considered from two perspectives: nonlinear piezoelectric coupling [65, 66] and nonlinear stiffness [67–69]. The later one is relatively easier to achieve and control, so it attracted an increasing number of researchers [46]. The most common approaches to the realization of such nonlinear stiffness technique introduces Duffing-type PEGs and piecewise-linear PEGs.

For a Duffing-type PEG, the potential elastic energy function $U(x)$ can be expressed in equation 1.1. Consequently, the structure has the cubic nonlinear force expressed by equation 1.2, where x is the vibration displacement of the oscillator, a and b are linear and nonlinear stiffness coefficients, respectively [70, 71].

$$U(x) = -\frac{1}{2}ax^2 + \frac{1}{4}x^4 \tag{1.1}$$

$$F(x) = -ax + bx^3 \tag{1.2}$$

Figure 1.9(a) shows a classical Duffing-type PEG which consists of a piezoelectric cantilever beam and two magnets [67, 72], one is attached to the tip of the beam while the second magnet is fixed in the reference frame. Under external excitations, the tip magnet oscillates inside the potential of the other fixed magnet and the restoring force becomes a nonlinear function of the tip deflection as shown in Figure 1.9(b). The magnitude and nature of the nonlinearity can be altered through the design of the system. For instance, dependence of the restoring force on the tip deflection can be changed by changing the di-

rection of the magnetic force, or the distance between the two magnets, or their strength. If the magnetic force is attractive, the restoring force can decrease with the tip deflection, which determines the softening response ($a \leqslant 0,\ b < 0$); if the magnetic force is repulsive, and the distance between the two magnets is relatively far, the restoring force can increase with the deflection, which determines the hardening response ($a \leqslant 0,\ b > 0$). The above two kinds of restoring forces lead to one stable equilibrium point of the system, such oscillator is also called the monostable oscillator. If the magnetic force is repulsive, and the distance between the two magnets is relatively close, the structure will have a negative stiffness for small tip deflections and exhibit two additional equilibria that correspond to offset states ($a > 0,\ b > 0$), the Duffing-type oscillator is then generally called the bistable oscillator [72].

Ramlan et al. investigated the hardening mechanism of the nonlinear monostable PEG. Their numerical and analytical studies showed that ideally, the maximum amount of power harvested by a system with a hardening stiffness was the same as that harvested by a linear system, regardless of the degree of nonlinearity. However, such a device has a larger bandwidth over which the significant power can be harvested due to the shift in the resonance frequency [67]. Stanton et al. proposed a similar monostable device, in which the tip magnet was interacted with the fields of oppositely poled stationary magnets. By tuning the magnetic interactions, they investigated both hardening and softening responses. The experimental results showed that softening stiffness had an excellent performance during the frequency reverse sweep excitation. Such PEG allows the frequency response to be broadened bidirectionally if the magnetic interactions can be self-tuned [73].

The intentional inclusion of nonlinearities in monostable PEGs makes the device more tolerant to variations in the excitation frequency around its nominal value when compared to a linear device. For certain types of excitations, especially those that have an impulsive nature or slowly time-varying frequencies, there seems to be potential benefits in utilizing a monostable nonlinear PEG to improve performance [74, 75]. However, under random excitations such as a white noise excitation, performance improvements via the intentional inclusion of nonlinearities is questionable. Daqaq demonstrated that the hardening-type nonlinearity failed to provide any enhancement of output power over linear PEGs under white Gaussian excitations; while under colored Gaussian excitations, the expected output power even decreased [76].

The first investigation of bistability in the vibration energy harvesting literature appears to be a theoretical paper by McInnes et al.. They assumed a bistable PEG composed of a clamped-clamped beam which can buckle under a modest compressive load, leading to two symmetric equilibrium states. They also gave a equivalent model of this theoretical PEG: a single lumped mass m with two linear springs of stiffness k and natural length l ($l > d$), as shown in Figure 1.10(a). Finally, they demonstrated the benefit of the stochastic resonance (SR) phenomenon in an energy harvesting mechanism [77]. When the SR effect occurs,

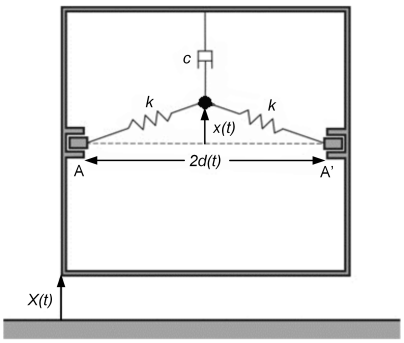

(a) A classical model of bistable oscillators [77]

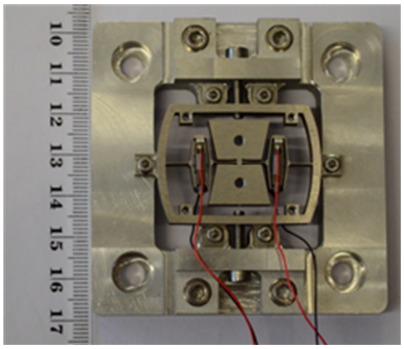

(b) Mono-block bistable PEG and its frame for initial buckling position tuning and clamping [79]

Figure 1.10: Bistable model and one of its implementations

the position of the system jumps randomly from one state to the other. The traditional SR is used to amplify a weak signal by an appropriate amount of noise. In an opposite point of view, this phenomenon could be used for energy harvesting if we suppose that the "noise" is provided by the environment excitation and a "weak signal" is added to a two-state-system [78].

One year later, such bistable energy harvesters were successfully implemented by Cottone et al. [70] and Erturk et al. [68]. Both groups created the bistable restoring force by using different magnet arrangements to induce a magnetoelastic buckling in a piezoelectrically laminated beam. Following the early efforts on the use of magnetoelastic potentials for creating bistability, numerous optimized structures were proposed later [80–82]. The main drawback of this kind of architectures is that it is relatively bulky due to the presence of the magnets, which decrease the power density. Moreover, the magnetic fields may interact with the powered electronics in some applications. So another bistable harvesters composed of buckled beams or plates have been proposed and implemented by Arietta et al. [83], Masana and Daqaq [84], Cottone et al. [31]. However, the accurate models of the above bistable PEGs are still very complicated, which makes it hard to undertake predictive simulation and thus optimize devices for different application environments. Different from the former bistable harvesters, we proposed a novel prototype of a bistable PEG based on a lumped spring-mass system in a buckled configuration more recently [69]. The architecture was compact and its equivalent model was more closed to the first theoretical model shown in Figure 1.10(a). Hence, the buckled-spring-mass (BSM) generator was precisely modeled and thoroughly analyzed. Based on the precise model, we gave a normalized expression which is applicable to any scale. An optimization strategy was also presented for various application environments [85]. Based on the former work, we finally proposed a mono-block miniaturized bistable PEG from the buckling effect, as shown in Figure 1.10(b). The performance under the real vibration signal from a driving car wheel

was investigated, the results clearly showed the wideband characteristics of the harvester device [79].

The potential benefits of the bistable PEGs are very much contingent to its ability to operate on the large-orbit inter-well periodic branch of solutions. When unique, this branch of solutions offers a wide bandwidth of frequencies for which the output power is large, making the harvesters insensitive to design tolerances and excitation's frequency drifts. In addition, under band-limited noise excitations, bistable harvesters have wider bandwidth and are less sensitive to the variations of the central frequency in the case of the colored noise as compared to monostable harvesters. However, bistable PEGs do not provide power enhancement in the case of white Gaussian excitation [72].

For a piecewise-linear PEG, the restoring force is actually piecewise-linear. However, the behavior of such systems is globally nonlinear. Such piecewise-linear stiffness can be physically realized by adding mechanical stoppers to conventional linear oscillators, which significantly increases the bandwidth for forward sweep [86–88]. In addition, we selected this kind of stoppers to protect the nonlinear oscillator, the additional stiffness introduced by the stoppers can also enlarge the operating bandwidth of the original nonlinear oscillator if the parameters are carefully designed [89]. The performances of a piecewise-linear PEG will be thoroughly studied in the next chapter.

Since most ambient vibrations are frequency-variant or random, the application of conventional linear resonating PEGs is usually limited. The above three kinds of techniques suited for ambient vibrations are summarized, especially the nonlinear energy harvesting techniques. However, there appears to be no "one-fits all" wideband vibration energy harvesting solution. A suitable technique for energy harvesting application should be selected according to the detailed excitation sources [46].

1.3.2 Energy extraction circuit

This subsection aims at presenting an up-to-date review of nonlinear EECs for vibration energy harvesting using piezoelectric materials. Moreover, a special focus on the load-independent or load-weakly-dependent EECs which are suitable for wideband vibrations will be thoroughly discussed in chapter 3.

Improved standard EECs

The electric signal generated from PEGs is an alternating current (AC) voltage, while the powered electronic devices generally require DC supply voltages. The simplest extraction circuit called standard circuit, which consists of a full-bridge rectifier and a smoothing capacitor, can achieve this function. However, due to its low efficiency and load-dependent drawbacks, in some more sophisticated and improved systems, the standard EEC is followed by a DC-DC converter used for impedance adaptation, a relatively complicated maximum power point tracking (MPPT) algorithm is used to ensure maximal energy conversion [90].

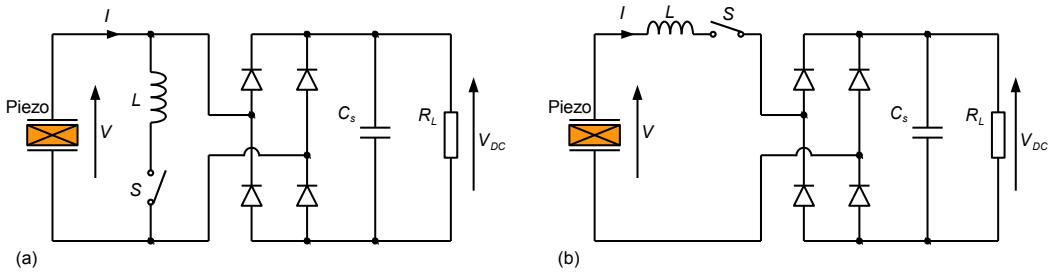

Figure 1.11: Parallel (a) and series (b) SSHI circuits

Such approach was first proposed by Ottman et al., the experimental results showed that the use of the DC-DC converter increased the harvested power by approximately 325% [91, 92]. It is worthy of note that in their approach, the converter only regulated the power flow from the PEG to the storage components. Additional DC-DC converter is also required to regulate the voltage in the power management unit and provide the standard DC voltage for the following electronic modules.

According to the schematic of the standard circuit, Vasic and Yao proposed a pulse width modulation EEC, where the full-bridge converter is composed of four electronic switches instead of diodes. The active switch components in the circuit can apply appropriate electrical boundary conditions at the piezoelectric element, make the output voltage be adaptive to the vibration velocity of the PEG. This approach can effectively maximize the harvested power of a dynamic electromechanical system in all excitation frequencies, which is a favorable technique for wideband vibration energy harvesting [93].

Nonlinear EECs

Besides the improved standard EECs, nonlinear energy extraction techniques using synchronous switches are another method to improve the efficiency of the energy conversion. Guyomar et al. proposed the synchronized switch harvesting on inductor (SSHI) technique in 2005 [94]. It seems to be the first and simplest nonlinear technique used to extract the electrical energy generated from PEGs. It consists in connecting an electrical switch and an inductor to a piezoelectric element in parallel or series [34, 95]. This technique is mainly derived from the so-called "synchronized switch damping" (SSD), a nonlinear technique earlier developed to address the problem of vibration damping on mechanical structures [96]. From the work of Badel et al. [95], the schematics of the two kinds of SSHI EECs are shown in Figure 1.11: Most of the time, the switch S is in open-circuit state. When the extreme displacements occur, the switch is closed for a brief time. In this duration, considering the capacitive behavior of the piezoelectric element which makes the resonance with the inductor, the piezoelectric voltage inverses. Accordingly, the SSHI approach increase the magnitude of the piezoelectric voltage and puts it in phase with the vibration velocity, which indicates that more energy is extracted from the vibration source. From the work of Badel et al., it was shown that for a weakly coupled PEG using this SSHI technique,

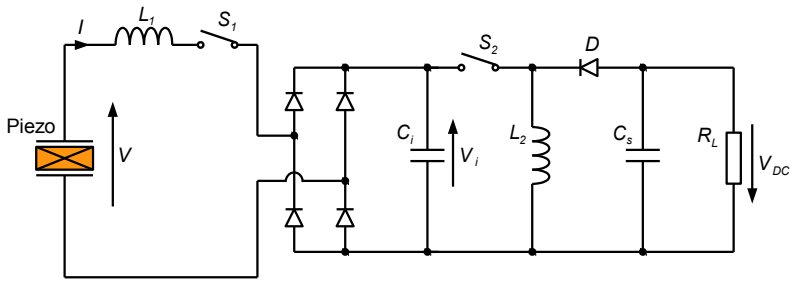

Figure 1.12: DSSH or ESSH circuit

if the quality factor of the circuits was high enough, the harvested power can be increased by over 400% under the constant vibration amplitude [34]. In addition, the operation principles of these two EECs are a little bit different from each other: the operations of the parallel-SSHI consist of inverting the voltage after an energy extraction process, while inversion and energy extraction occur at the same time for the series-SSHI [47]. Based on SSHI EECs, many researchers proposed their work of optimizations or applications [97–104]. An approach called "synchronized switch and discharging to a storage capacitor through an inductor" (SSDCI) was proposed by Wu et al., they used a similar architecture to the series-SSHI, but with a modified switch control strategy [105]. Another advanced approach named "synchronized switch harvesting on inductor using magnetic rectifier" (SSHI-MR) was proposed by Lallart et al., they selected a transformer composed of two primary inductors and one secondary inductor to replace the inductor and the full-bridge rectifier in the original series-SSHI EEC. This approach is very suitable for low piezoelectric output voltage. To combine SSHI-MR approach with the parallel-SSHI approach, they also proposed the hybrid SSHI approach at the same time, such hybrid approach permits widening the load bandwidth which is a good characteristic for wideband vibrations [106].

Synchronous electric charge extraction (SECE) EEC is a load-independent circuit and was proposed by Lefeuvre et al. in 2005. This approach successfully addresses the issue of impedance matching while enhancing the energy extraction effectiveness [107]. Detailed analysis of the SECE technique is presented in chapter 3. In this technique, the synchronous switching concept is used in a slightly different manner as in the SSHI technique. The inductor in the circuit can be considered as an intermediate energy storage element. The energy harvesting process is therefore performed in two steps. First, the energy available on the piezoelectric element is transferred to the inductor. Then the piezoelectric element is disconnected from the circuit and the energy stored in the inductor is transferred to the final storage element. This therefore prevents the direct connection of the piezoelectric element to the load, and thus leads to a harvested energy independent on the connected load [47]. Form this principle, Lallart et al. combined the series-SSHI approach with the SECE technique, and proposed the double synchronized switch harvesting (DSSH) technique, as shown in Figure 1.12. The approach consists first of transferring a part of

the generated energy to an intermediate storage capacitor C_i, and then transferring the energy on C_i to the inductor L_2 and finally to the storage capacitor C_s [108]. Similar to this EEC, Shen et al. proposed the enhanced synchronized switch harvesting (ESSH) approach, in which they optimized the second switch control strategy: when the second energy transfer process started, the switch S_2 would stop being closed as soon as a portion of the electric charge is removed from the capacitor C_i, i.e. the intermediate voltage V_i dropped to the preset voltage V_L* instead of 0 in the DSSH approach [109].

Initial energy injection EEC is another optimized approach based on the SECE technique [110]. The presentation of this approach is shown in the appendix of the thesis. In this approach, the harvested power is weakly dependent on the load. This is because a portion of the stored energy in the load circuit is injected to the piezoelectric element as soon as the SECE approach finishes extracting the generated energy. The injected energy introduced an initial voltage on the piezoelectric element which is a function of the storage voltage in the load circuit. The energy injection process enhances the available energy density on the piezoelectric element, and finally increases the energy extraction density. Accordingly, Becker et al. used an additional piezoelectric element integrated in the same structure as an injection generator, it provided an injection energy to the main piezoelectric element. Such design avoids the complicated energy injection circuit but almost has the same performance as the original initial energy injection EEC [111].

We propose the optimized synchronous electric charge extraction (OSECE) approach which is also a load-weakly-dependent EEC. Moreover, this dependency can be easily reduced by changing the turns ratio of the transformer. The approach is an improvement of the SECE technique. Not only the electronic circuitry and the switch control strategy are simplified, but the energy conversion effectiveness is also enhanced [112]. The theoretical model of this EEC and its performances will be clearly presented in the thesis.

Finally, in order to give a clear comparison of the above nonlinear EECs, based on the work of Guyomar and Lallart [47], we also propose a tentative visual description of the various EECs according to several factors, as shown in Table 1.2, where k and Q_m are, respectively, the coupling coefficient and mechanical quality factor of the PEG, the expression k^2Q_m represents the figure of merit of the electromechanical structure.

Implementation issues for nonlinear EECs

Generally speaking, the synchronous switches in the above nonlinear EECs are realized using bipolar junction transistors (BJTs) or metal-oxide-semiconductor field-effect transistors (MOSFETs) [113] or even silicon controlled rectifiers (SCRs) [114]. These electronic switches need to be correctly driven by the control signal as well as the electrical energy, which are produced by external devices in most literature. However, VEHDs are supposed to be stand-alone systems that operate autonomously. It is mandatory to achieve a to-

*V_L is selected by the optimization algorithm.

Table 1.2: Classification scores of EECs

EECs	Harvested energy		Load independent	Implementation
	low k^2Q_m	high k^2Q_m		
Standard	★☆☆☆	★★★★	★☆☆☆	★★★★
Parallel-SSHI	★★★★	★★★☆	★☆☆☆	★★★☆
Series-SSHI	★★★★	★★★☆	★☆☆☆	★★★☆
SSHI-MR	★★★★	★★★☆	★☆☆☆	★★☆☆
Hybrid SSHI	★★★★	★★★☆	★★☆☆	★★☆☆
SSDCI	★★☆☆	★★★☆	★★★☆	★★☆☆
SECE	★★☆☆	★★☆☆	★★★★	★★☆☆
DSSH/ESSH	★★★☆	★★★☆	★★★★	★☆☆☆
Initial energy injection	★★★★	★★☆☆	★★★☆	★☆☆☆
OSECE	★★★★	★★☆☆	★★★★	★★★☆

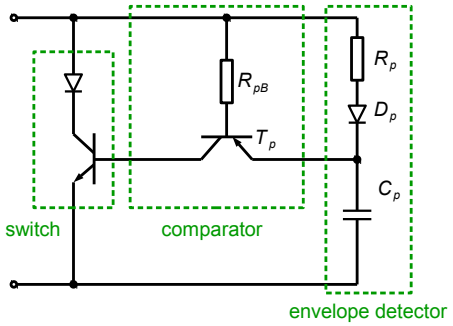

Figure 1.13: PKD circuit and the self-powered switch [115]

tally autonomous EEC for which the synchronized switches are driven and powered by the VEHD itself, such circuits are usually called the self-powered EECs, and the energy balance between the extracted energy and the required energy to drive the switches should be positive.

A peak detector (PKD) circuit shown in Figure 1.13 is a classical approach to achieve the self-powered function in some nonlinear EECs. It consists of a simple comparator and an envelope detector [115]. Normally, the envelope detector is an electronic circuit that provides an output voltage on the capacitor, which is the envelope of the input alternating signal [116]. But the input impedance of the comparator is far lower than those of traditional operational amplifier comparators. If the comparator operates, the electrical charge stored in the capacitor will be discharged to the base emitter junctions of T_p and the switch. Consequently, the voltage value on the capacitor will decrease instead of enveloping the input signal. However, this characteristic is especially suitable for the synchronous switching techniques [113]. Lallart et al. already used this PKD to drive the switches

in the advanced SSHI EEC suited for low piezoelectric output voltage in reference [117]. Nevertheless, this self-powered approach introduced the switching phase lag which reduced the efficiency of energy conversion. Liang and Liao thoroughly optimized this PKD circuit dedicated to the SSHI technique, and they gave the theoretical expression of the switching phase lag, which means the value of the phase lag cannot be neglected in the precise circuit model [118]. In chapter 4, we clearly explain the reason of this kind of switching phase lags, and also evaluate the theoretical power consumption of the PKD circuit. Finally, we show that the switching phase lag does not reduce the maximum harvested power under the constant excited acceleration amplitude, and the power consumption of the PKD circuit strongly depends on the value of the capacitor in the envelope detector [113].

Except the PKD approach, another self-powered approach is to use a zero-crossing detector. Different from the voltage peak detector, the zero-crossing detector should detect the zero velocity of the PEGs or said zero equivalent output current of the piezoelectric elements [119]. Chen et al. proposed such zero-crossing detector used for the SSHI EEC, the switching phase lag was reduced, but two additional piezoelectric elements were required to provide the switch control signal and power the zero-crossing detector circuit [120].

It is worthy of note that in some nonlinear EECs which need the accurate switching closing time (SECE, DSSH, ESSH and initial energy injection), the self-powered designs are hardly implemented by using the above analog approaches. However, the complex digital approaches are easier to provide the accurate duration to close switches. Shen et al. used a digital approach to drive the synchronous switches in the ESSH EEC, the switch control circuit consumed a constant power instead of being proportional to the extracted power, such design therefore has a big advantage in the VEHDs which have high harvested powers [109].

Recently, Giusa et al. proposed the use of mechanical switches in the SSHI circuit. The switches consist of a metal oscillator and two metal stoppers, so the switches are passively controlled by the vibration itself, avoiding the complex switching control strategies and the self-powered circuits [121]. This mechanical self-powered approach dedicated to the OSECE technique is also proposed in chapter 4 [122].

1.3.3 Energy storage element

The vast majority of VEHDs will not be able to supply energy at a constant rate over long periods of time. Moreover, the power consumption of the powered circuitry will be much higher than the harvested power in some short durations (e.g. during the wireless communications). So the addition of a storage element, which stores the harvested power first, and then supplies electrical energy for the self-powered electronic modules through the power management unit, is required. Obviously, batteries and capacitors are the mainstay of energy storage elements for over a century. Hence, both rechargeable batteries and capacitors are generally selected by researchers in the field of energy harvesting.

When using rechargeable batteries as the energy storage element, the rate and way in which the battery is charged can significantly influence the lifetime of the cells. In addition, limits such as available cell voltages must be considered. For instance, lithium-ion cells have nominal voltages of around 3.7 V [123], it is not possible to directly charge the cells if the piezoelectric output voltage is lower than 3.7 V. Consequently, complex energy extraction interfaces are required and must be carefully designed. However, as the battery voltage is relatively constant, the following voltage regulation is simple to be implemented or may not even be needed as long as the cells are carefully chosen [124].

Using capacitors, or using supercapacitors because of their higher energy storage density, for the storage element has the advantage that pushing energy into it is a relatively simple task with few constrains on how the capacitor is charged [125]. Because a storage capacitor is very tolerant to the rate at which energy is stored into and out of it. The interaction between the energy extraction interface and the storage capacitor can be considered as ignored. In other words, researchers are free to alter the operating mode of the EEC to optimize the operation of the transducer without taking into account how it affects the storage element. However, since capacitive storage has the wide voltage range over which it operates, the output voltage regulation for the following self-powered circuitry becomes much more complicated [124].

This thesis develops a demonstration platform for vibration energy harvesting technologies in chapter 5, in which we selected an electrolytic capacitor as a storage element. A complex undervoltage lockout (UVLO) function and a high efficient voltage regulation are also required to provide a relatively stable standard voltage for the self-powered device.

1.4 Thesis organization

This thesis mainly investigates two parts of a typical VEHD: PEG and EEC, especially the OSECE EEC suited for wideband vibrations. Considering the practical implementation of the OSECE EEC, two kinds of self-powered approaches are presented. Finally, a self-powered demonstration platform is developed and powered by VEHDs.

Chapter 1 presents the background introduction and literature review of wideband VEHDs.

Chapter 2 presents the investigation of two kinds of PEGs: linear and piecewise-linear PEG. The dynamic models and their comparisons are thoroughly studied. The piecewise-linear PEG is more suitable for ambient vibrations such as their frequencies are slowly time-varying or have impulsive natures. The additional benefits of the mechanical stoppers in the piecewise-linear PEG are also introduced.

Chapter 3 presents three typical EECs: standard, SECE and OSECE. The OSECE is a new nonlinear energy extraction technique which has favorable characteristics for

wideband vibrations. Moreover, comparing with the SECE approach, the circuit is easier to implement, the harvested power is also enhanced. The theoretical results in this chapter are well confirmed by the experimental results.

Chapter 4 proposed two self-powered OSECE circuits: electronic approach and mechanical approach. The different operating principles are theoretically analyzed. The advantages and drawbacks of the two self-powered approaches are experimentally compared.

Chapter 5 presents the development of a demonstration platform which is a prominent application of the energy harvesting technologies. It includes a power management unit, a self-powered wireless sensor node, and a coordinator node. The demonstration shows the advantages of the proposed OSECE approach, gives a great application potential of VEHDs.

Finally, the main innovation and contribution of this thesis are pointed out in the general conclusion.

2

Piezoelectric generators: modeling and comparative study

Contents

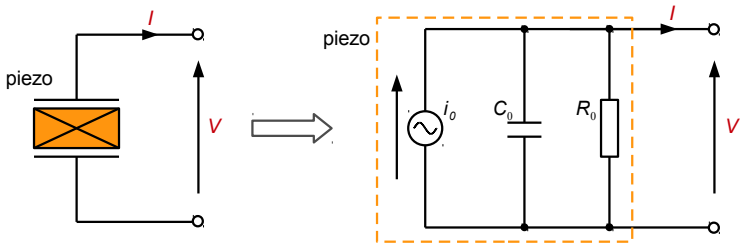

Figure 2.1: Equivalent circuit of a piezoelectric element integrated into a PEG

2.1 Introduction

Piezoelectricity is one of the most common ways of transforming mechanical energy into electrical energy. For energy harvesting application, it is realized by the use of an oscillating system composed of a mechanical oscillator, an integrated piezoelectric material, and a frame. This kind of oscillating structures is usually called PEG. When the frame of the PEG is in linked to a vibration source, the oscillator-frame distance varies. This distance variation induces an alternative strain on the piezoelectric material, an alternative voltage output is then directly obtained from the electrodes according to the direct piezoelectric effect.

There are several piezoelectric materials covering ceramics, single crystals, polymers, and thin films that can be integrated in PEGs [126]. If the poling axis and the mechanical strain axis are perpendicular to one another, the PEG uses the 31-mode of piezoelectricity*. On the other hand, if the poling and strain axes are coincident, the PEG is said to be operating in the 33-mode, typical example is the piezoelectric stack as depicted in the BSM PEG (Figure 1.10(b)).

Generally speaking, a PEG can be simply modeled as a current source i_0 proportional to the relative vibration velocity of the oscillator, connected in parallel with a clamped capacitance C_0 of the piezoelectric element, and its parasitic resistance R_0, see Figure 2.1 [119]. Assuming that the relative vibration displacement between the frame and the oscillator is u. The output current I and voltage V of a PEG are then described by equation 2.1. Here, α is a piezoelectric force-voltage coefficient which is an intrinsic property of a given PEG [94]. The value of R_0 is usually very large, hence the leakage current due to the parasitic resistance can be neglected in even simpler circuit model [127].

$$I = \alpha \dot{u} - C_0 \dot{V} - \frac{V}{R_0} \tag{2.1}$$

In this chapter, two typical PEGs, which will be selected to generate energy in the experiments of the thesis, are proposed and modeled. One is the linear model, the other is the piecewise-linear model. Both of them are mainly made up of a classical cantilever

*The 3- and 1- axes are the poling and strain directions respectively.

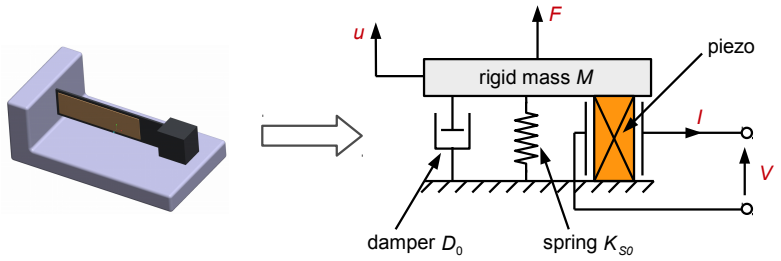

Figure 2.2: Linear PEG and its electromechanical model

beam with a bonded piezoelectric layer. The PEGs use the 31-mode of piezoelectricity. At last, some applied benefits of the mechanical stoppers are specially presented.

2.2 PEGs and their theoretical models

2.2.1 Linear PEG

A simplest linear PEG is a cantilever beam with a bonded piezoelectric layer, shown in Figure 2.2. The beam is able to amplify the ambient vibration, provided that the excitation vibration spectrum matches its resonance frequency. It means that the cantilever beam offers a high average strain in its material, due to the direct piezoelectric effect, the dynamic strain applied in the piezoelectric layer will then generate an alternating voltage output V across the piezoelectric electrodes.

In the linear electromechanical operating condition, a {mass M + spring K_{S0} + damper D_0 + piezoelectric} system with a single degree of freedom can provide a relevant description. Although this model does not directly correspond to the cantilever structure, it gives a faithful description of the structure behavior. The simplicity of the model allows the analytical calculation of the mechanical variables in the linearly elastic domain, as well as the electrical variables [34].

The schematic representation of the electromechanical model is shown in Figure 2.2, the rigid mass M undergoes the action of both external and internal forces: the external force F is the mechanical excitation applied to the structure, it corresponds to an inertial PEG driven at an external ambient acceleration γ, in which $F = M\gamma$; the internal force consists of a viscous force $D_0\dot{u}$ due to the damper, a restoring force $K_{S0}u$ due to the spring, and a electromechanical force F_p due to the to the elasticity and converse piezoelectric action of the piezoelectric element. The dynamic equilibrium equation of the system is then given by equation 2.2.

$$M\ddot{u} = F - F_p - K_{S0}u - D_0\dot{u} \tag{2.2}$$

According to the piezoelectric equations and equation 2.1, the relationship between the

Table 2.1: Energy terms definitions

$\int F\dot{u}\,\mathrm{d}t$	Provided energy
$\frac{1}{2}M\dot{u}^2$	Kinetic energy
$\frac{1}{2}K_0u^2$	Potential elastic energy
$\int D_0\dot{u}^2\,\mathrm{d}t$	Mechanical losses
$\int \alpha V\dot{u}\,\mathrm{d}t$	Transferred energy

mechanical variables (u, F_p) and the electric variables (I, V) can be finally expressed by equations 2.3, where K_p is the short-circuit stiffness of the piezoelectric layers. The leakage current due to the parasitic resistance R_0 is neglected here for later conciseness. As both stiffness act in the same way on the mass M, a global equivalent stiffness K_0 is defined in equation for short-circuit condition, a final dynamic equilibrium equation 2.5 is set to substitute equation 2.2.

$$\begin{cases} F_p = K_p u + \alpha V \\ I = \alpha\dot{u} - C_0\dot{V} \end{cases} \tag{2.3}$$

$$K_0 = K_{S0} + K_p \tag{2.4}$$

$$M\ddot{u} = F - K_0u - D_0\dot{u} - \alpha V \tag{2.5}$$

The energy equation 2.6 is obtained by multiplying both terms of equation 2.5 by the velocity and integrating over the time variable. It is clearly shows that the energy provided by the external exciting force F is divided into kinetic energy, potential elastic energy, mechanical losses, and the transferred energy, as respectively defined in Table 2.1. The transferred energy corresponds to the part of the mechanical energy which is converted into electrical energy. It is the sum of the electrostatic energy stored on the piezoelectric elements and the energy absorbed by the following EEC, as shown by equation 2.7.

$$\int F\dot{u}\,\mathrm{d}t = \frac{1}{2}M\dot{u}^2 + \frac{1}{2}K_0u^2 + \int D_0\dot{u}^2\,\mathrm{d}t + \int \alpha V\dot{u}\,\mathrm{d}t \tag{2.6}$$

$$\int \alpha V\dot{u}\,\mathrm{d}t = \frac{1}{2}C_0V^2 + \int VI\,\mathrm{d}t \tag{2.7}$$

The electromechanical coupling coefficient k describes the energy conversion between the electrical and mechanical forms in the structure. For a PEG in open-circuit subjected to a static stress, it is defined as the electrostatic energy divided by the total energy in the system. It can be expressed as equation 2.8, where $K_0^{'}$ is the global equivalent system stiffness when the piezoelectric layers are in open-circuit, defined in equation 2.9. In order to simplify the theoretical expressions of the calculations in the following chapters, a modified

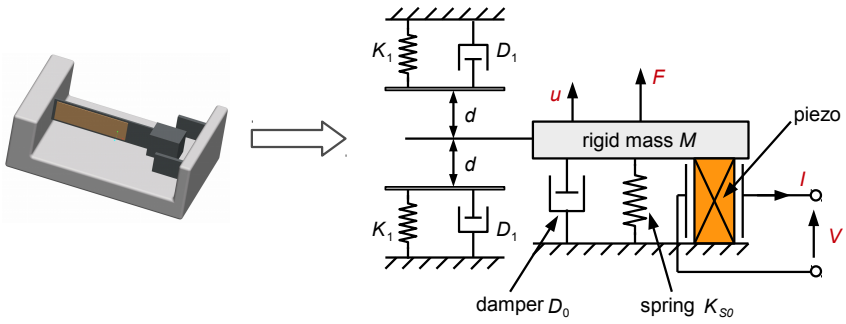

Figure 2.3: Piecewise-liner PEG and its theoretical model

coupling coefficient k_m is defined as equation 2.10. Arroyo and Badel showed that it also gives information about the ability of a PEG to convert the energy, insofar as it represents the quotient between the electrostatic energy and the elastic energy. Note that while k^2 remains inferior to 1 ($k^2 = 1$ means that all the input mechanical energy is converted into electrostatic energy), k_m^2 is not limited. For weakly coupled electromechanical structure, the values of k^2 and k_m^2 are close to each other [42]. Another important dimensionless parameter of this system is the mechanical quality factor Q_m expressed in equation 2.11, it is inversely proportional to the mechanical losses. Finally, the value of $k_m^2 Q_m$ exhibits the figure of merit of the given electromechanical structure, where ω_0 is the resonance angular frequency of the system when the piezoelectric layers are short-circuited [112].

$$k^2 = \frac{\frac{1}{2}C_0V^2}{\frac{1}{2}K_0'u^2} = \frac{\alpha^2}{K_0'C_0} = \frac{\alpha^2}{K_0C_0 + \alpha^2} \tag{2.8}$$

$$K_0^{'} = K_0 + \frac{\alpha^2}{C_0} \tag{2.9}$$

$$k_m^2 = \frac{k^2}{1-k^2} = \frac{\alpha^2}{K_0C_0} \tag{2.10}$$

$$Q_m = \frac{\sqrt{K_0M}}{D_0} \tag{2.11}$$

$$k_m^2 Q_m = \frac{\alpha^2}{C_0D_0}\sqrt{\frac{M}{K_0}} = \frac{\alpha^2}{C_0D_0\omega_0} \tag{2.12}$$

2.2.2 Piecewise-linear PEG

Piecewise-linear PEG can be made with a simple cantilever beam with one or two mechanical stoppers laid on its sides. During the oscillation, such structures exhibit the piecewise-linear stiffness [46]. This thesis investigates a piecewise-linear PEG composed of a piezoelectric cantilever beam and two symmetrical stoppers. Figure 2.3 shows this PEG as well as its theoretical model. It is worthy of note that such additional stoppers can also prevent damage of the piezoelectric layers when the PEG is subjected to shock forces.

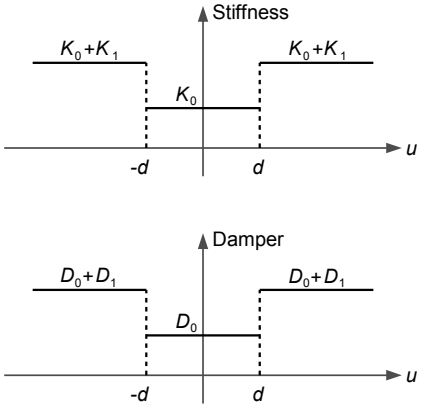

Figure 2.4: Piecewise-liner stiffness and damping of the structure

As presented in the previous section, the cantilever beam in the piecewise-linear PEG can be descripted by a {mass M + spring K_{S0} + damper D_0 + piezoelectric} system with a single degree of freedom. The global equivalent stiffness of the piezoelectric beam is assumed as K_0 when the piezoelectric layers are in short-circuit condition. Acoustic, thermal, frictional and structural dissipation mechanisms are actives during impact and subsequently while the beam and the stopper are engaged. To account for these bilinear behaviors, the two stoppers are modeled as {spring K_1 + damper D_1} systems which are also shown in the theoretical model of Figure 2.3 [86], where d is the limited distance between the rigid mass and the stoppers.

In this piecewise-linear system, the relative motion of the rigid mass can be divided into two stages. In the first stage, assuming that the vibration displacement u is lower than the limited distance d, the system retains an overall stiffness K_0 and damping D_0, respectively. When the rigid mass deflection reaches its limited distance d, the tip of the beam and one of the stoppers are engaged each other. In this stage, the overall stiffness and damping of the system are then increased to $K_0 + K_1$ and $D_0 + D_1$, respectively [88]. It means that the global restoring force F_r and the damping force F_d applied on the rigid mass should be modified as in equations 2.13 and 2.14. The dynamic equation of this piecewise-linear PEG is then given by equation 2.15.

$$\begin{cases} F_r = (K_0 + K_1)\, u - K_1 d & u \geqslant d \\ F_r = (K_0 + K_1)\, u + K_1 d & u \leqslant -d \end{cases} \tag{2.13}$$

$$F_d = (D_0 + D_1)\, \dot{u} \tag{2.14}$$

$$\begin{cases} M\ddot{u} = F - (K_0 + K_1)\, u + K_1 d - (D_0 + D_1)\, \dot{u} - \alpha V & u \geqslant d \\ M\ddot{u} = F - K_0 u - D_0 \dot{u} - \alpha V & -d < u < d \\ M\ddot{u} = F - (K_0 + K_1)\, u - K_1 d - (D_0 + D_1)\, \dot{u} - \alpha V & u \leqslant -d \end{cases} \tag{2.15}$$

2.3 Performances comparsion between the two PEGs

2.3.1 Frequency response

The frequency responses of the two PEGs will be theoretically analyzed in this subsection. In order to make the comparison as generic as possible, some parameters mentioned in the previous section are normalized as in equation 2.16, the damping characteristics ξ_0, ξ_1 and the resonance angular frequencies ω_0, ω_1 of the cantilever beam and the mechanical stopper are defined in equations 2.17 and 2.18, respectively.

$$\bar{u} = \frac{u}{d}\,, \quad \bar{V} = \frac{C_0}{\alpha d}V\,, \quad \bar{\gamma} = \frac{\gamma}{d} \tag{2.16}$$

$$\xi_0 = \frac{D_0}{2M\omega_0}\,, \quad \omega_0 = \sqrt{\frac{K_0}{M}} \tag{2.17}$$

$$\xi_1 = \frac{D_1}{2M\omega_1}\,, \quad \omega_1 = \sqrt{\frac{K_1}{M}} \tag{2.18}$$

Therefore, the normalized dynamic equations of the linear and piecewise-linear PEGs can be written as in 2.19 and 2.20, respectively.

$$\ddot{\bar{u}} + 2\xi_0\omega_0\dot{\bar{u}} + \omega_0^2\bar{u} + k_m^2\omega_0^2\bar{V} = \bar{\gamma} \tag{2.19}$$

$$\begin{cases} \ddot{\bar{u}} + 2\xi_0\omega_0\dot{\bar{u}} + \omega_0^2\bar{u} + k_m^2\omega_0^2\bar{V} = \bar{\gamma} - \left(2\xi_1\omega_1\dot{\bar{u}} + \omega_1^2\bar{u} - \omega_1 2\right) & \bar{u} \geqslant 1 \\ \ddot{\bar{u}} + 2\xi_0\omega_0\dot{\bar{u}} + \omega_0^2\bar{u} + k_m^2\omega_0^2\bar{V} = \bar{\gamma} & -1 < \bar{u} < 1 \\ \ddot{\bar{u}} + 2\xi_0\omega_0\dot{\bar{u}} + \omega_0^2\bar{u} + k_m^2\omega_0^2\bar{V} = \bar{\gamma} - \left(2\xi_1\omega_1\dot{\bar{u}} + \omega_1^2\bar{u} + \omega_1 2\right) & \bar{u} \leqslant -1 \end{cases} \tag{2.20}$$

To obtain the frequency response curves of the two PEGs, MATLAB and SIMULINK (The MathWorks©) softwares can be selected to integrate the above dynamic equations numerically. Some simulation parameters are assumed as followed:

- The acceleration γ is a 1g amplitude sinusoidal forward sweep signal.
- The piezoelectric layers in the PEG are in open-circuit condition.
- $k_m = 0.1\,,\ \ \xi_0 = 0.01\,,\ \ \xi_1 = 0.02.$
- The first resonance frequencies of the beam and the stoppers are 87 Hz and 200 Hz, respectively.

The frequency response curves are then shown in Figure 2.5, where the frequency is normalized by the first resonance frequency ω_0 of the cantilever beam. It is clearly seen that in the linear case, the high vibration displacement amplitude is limited to a very narrow bandwidth, slightly wider than points B to C. While in the piecewise-linear case, the vibration first follows the linear PEG behavior and increases monotonically from A

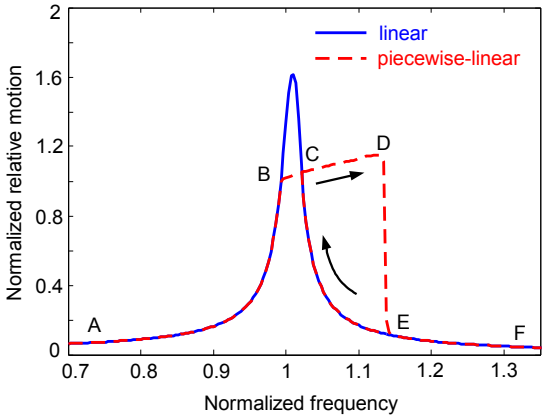

Figure 2.5: The frequency responses of the PEGs

to B. Then the vibration amplitude reaches the limited distance d and starts to deform the stoppers. The operating bandwidth is significantly extended beyond the linear case. The excitation frequency finally reaches point D and the motion drops down to point E. Subsequently, the free end of the beam cannot reach the stoppers anymore and the frequency response of the linear PEG is recovered.

2.3.2 Parameter effects on the frequency response

In the piecewise-linear PEG, for a specific cantilever beam, four certain parameters (damping characteristic of the stoppers ξ_1, stiffness of the stoppers K_1, external excited acceleration γ and limited distance d) show strong influences on its frequency response [88]. As shown in Figure 2.6, each of these four parameters has been studied separately with three other parameters fixed. The parameters of the cantilever beams (both in the linear PEG and in the piecewise-linear PEG) remain the same as in the case of Figure 2.5.

In Figure 2.6(a), only the damping characteristics of the stoppers ξ_1 are changed from 0.005 to 0.02. It is clearly shown that the frequency bandwidth is strongly affected by the damping characteristic: lower damping leads to the wider bandwidth. As the damping characteristic also contains the relationship to the energy losses of the piecewise-linear PEG during the impact phase, it is necessary to design a mechanical stoppers with the low damping characteristic.

Because the characteristic of the first resonance frequency of the mechanical stopper is related to its stiffness K_1 according to equation 2.18, Figure 2.6(b) shows the different frequency responses with various stiffness of the stoppers. The curves show that to obtain the widest frequency bandwidth, there exist an optimal value of the stiffness. When the stiffness is softer than this optimal value, the bandwidth is increased with the stiffness. However, if the stiffness is harder than the optimal value, the bandwidth will decrease. This is a different conclusion from the previous literature said that the frequency bandwidth would keep constant when the stiffness of the stoppers were about 16 times harder than

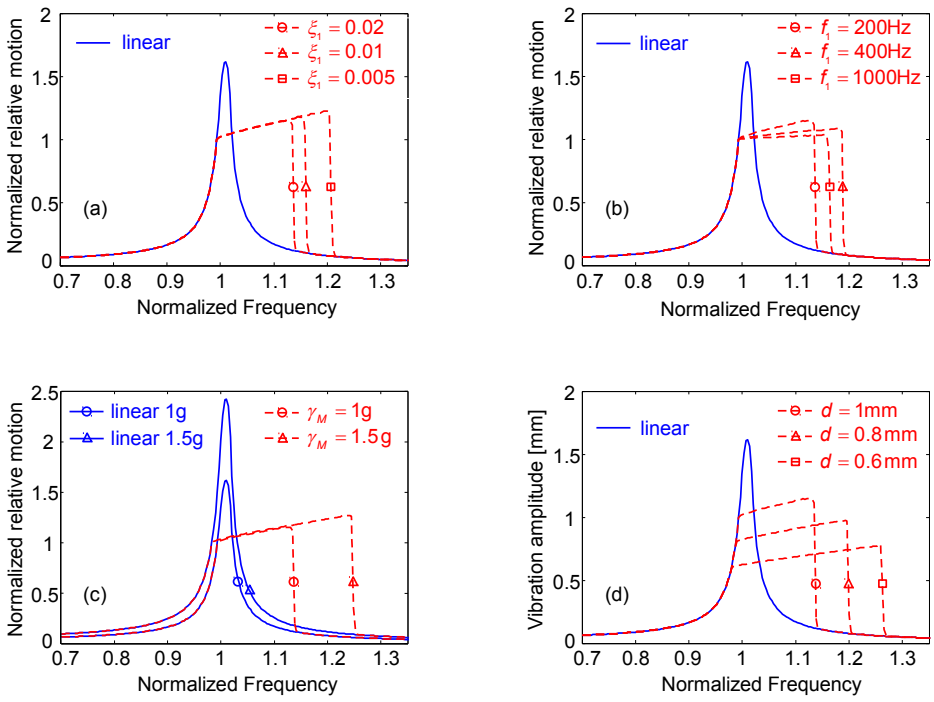

Figure 2.6: The frequency responses of the PEGs in the case of 4 different parameters (solid line: linear PEG; dashed line: piecewise-linear PEG)

the cantilever beam [86]. The reason is that the authors obtained the conclusion based on an assumption that the velocity of the rigid mass is approximate to a sinusoidal signal. However, according to our research, when the stoppers stiffness is very high, the sign of the tip mass velocity will suddenly change as soon as the tip of the beam impact the stoppers. The approximation of a sinusoidal signal is no longer accurate. From another point of view, due to the harder stiffness, the average restoring force F_r applied on the cantilever beam becomes larger and shorter at the same time. Since these two influences are repulsive, there should exist an optimized value of the stopper's stiffness, if the stiffness is harder than this point value, the frequency bandwidth will decrease.

In Figure 2.6(c), the external acceleration amplitude γ_M exciting on the two PEGs is changed from 1g to 1.5g. The frequency bandwidth of the piecewise-linear PEG is especially increased. In this case, the larger external acceleration would also lead the higher vibration amplitude of the linear PEG around its resonance frequency, while the vibration of the piecewise-linear PEG is still limited due to the two side stoppers.

Figure 2.6(d) gives the different frequency responses of the piecewise-linear PEG with several limited distances d. As can be seen, a nearer stopper distance results in a wider frequency bandwidth at the detriment of a reduction in the vibration amplitude. To obtain the best performance of the PEG, this distance value needs to be thoroughly optimized in the specific applications.

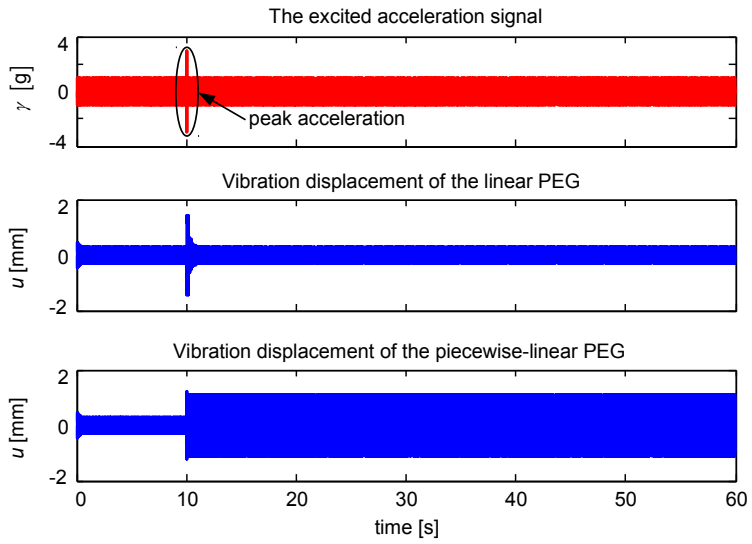

Figure 2.7: The time history of the sinusoidal excitation, the vibration displacements of the linear PEG and piecewise-linear PEG

2.3.3 Performances under various excitations

As a mater of fact, due to the hardening effect [72], the piecewise-linear PEG significantly increase the bandwidth during the external acceleration forward sweep (following the A-B-C-D-E-F path), while maintain the same bandwidth as the linear PEG during the reverse sweep (following the F-E-C-B-A path). Which means in various excitations, if the excitation frequency lies between the points C and D, it is possible that the beam can not hit the mechanical stoppers (the same as the linear PEG in Figure 2.5). In this subsection, several simulation results based on MATLAB and SIMULINK softwares will be presented to discuss the performances of the above two PEGs when the excitation frequencies are between the points B to D.

Firstly, assuming the external excited acceleration is a sinusoidal signal with a constant frequency between the points C and D, and the cantilever beam operates in the linear condition, in this case, an applied peak acceleration on the PEG would change the operating condition and make the collisions occur again. This useful perturbation can either be produced by an external shock force or by adding a snap voltage on the piezoelectric elements (a few periods of a sinusoidal voltage whose frequency is ω_0 for instance).

Figure 2.7 gives an illustration of such a way to artificially reach the periodic collisions pattern to occur. In this example, the excitation consists in a sinusoidal signal whose amplitude is 1g and the frequency is 92 Hz, which is sensitively larger than the resonance frequency (87 Hz) of the cantilever beam. Between times 10 s and 10.1 s, a 2g peak acceleration is added. The limited distance d of the simulated PEG is 1 mm. Before the peak, the beam vibration is small and it does not hit the stoppers. At time 10 s, because of the additional acceleration, the beam starts colliding with the stoppers. The vibration

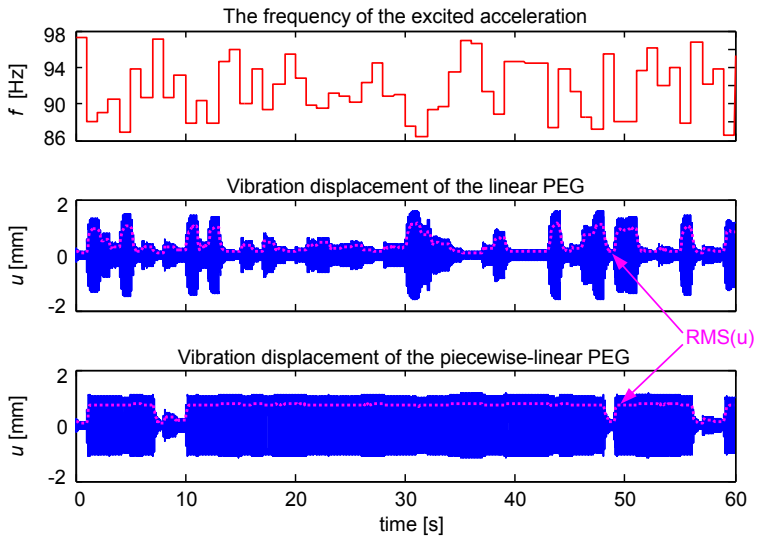

Figure 2.8: The time history of the excitation frequency, the vibration displacements of the linear PEG and piecewise-linear PEG

amplitude is then greatly enlarged, and it keeps on hitting the stoppers even after the end of the perturbation (time 10.1 s).

Secondly, assuming the external excited acceleration is a sinusoidal signal, but its frequency is uniformly distributed over a wide range from the points B to D, as expressed in equation 2.21. In this case, the performance of the piecewise-linear PEG is still much better than that of the linear PEG [86]. It is worthy of note that, the excited acceleration signal given in equation 2.21 should be a continuous function of time. To implement a discontinuous random angular frequency $\omega(t)$ of the excited acceleration, a periodic phase $\phi_\gamma(t)$ given in equation 2.22 is used in the simulation, where Δt is the simulation time step.

$$\gamma(t) = \sin[\omega(t) \times t] \tag{2.21}$$

$$\begin{cases} \phi_\gamma(t) = \mathrm{mod}\left(\sum \omega(t) \times \Delta t\,,\ \ 2\pi\right) \\ \gamma(t) = \sin[\phi_\gamma(t)] \end{cases} \tag{2.22}$$

Figure 2.8 compares the performances of these two PEGs, the excitation frequency is uniformly distributed over a 11.2 Hz range from 86.15 Hz to 97.35 Hz, and the acceleration amplitude is 1g. Using the linear PEG, the displacement amplitude is large only when the excited frequency is closed to its resonance frequency (87 Hz). Most of the time, the vibration displacement amplitude is lower than the limited distance d (1 mm). While using the piecewise-linear PEG, it is clearly shown that most of the time, vibration amplitude is around 1 mm. Finally, comparing the average root mean square (RMS) value of the vibration amplitude, the value of the piecewise-linear PEG is 1.73 times larger than that

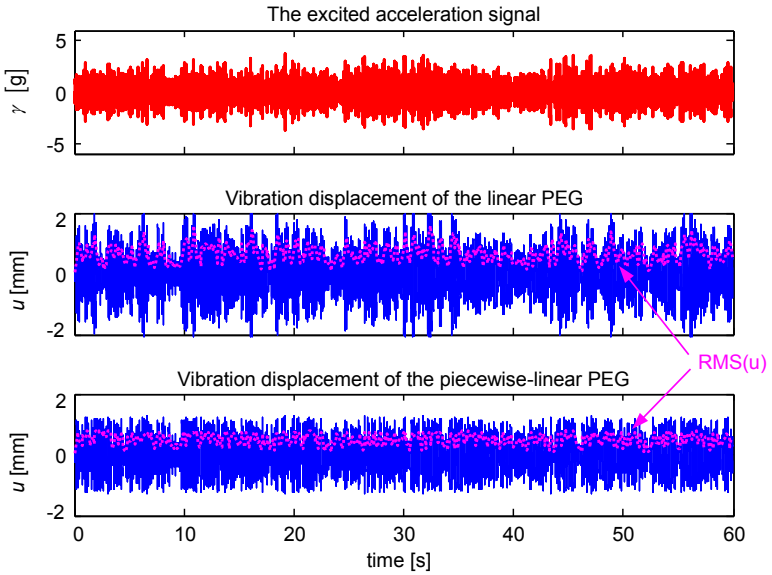

Figure 2.9: The time history of the random excitation, the vibration displacements of the linear PEG and piecewise-linear PEG

of the linear PEG.

Finally, assuming the external excited acceleration is a band-limited white noise signal, and the bandwidth is from the points B to D, which means the noise bandwidth includes the resonance frequency of the cantilever beam. In this case, if the RMS value of the excited acceleration is large enough (the vibration amplitude of the beam can reach the limited distance during the most of the time), due to the stroke limited stoppers in the piecewise-linear PEG, the performance of the linear PEG is better. Comparing the RMS values of the displacements shown in Figure 2.9, the piecewise-linear RMS displacement value is only 76% of that of the linear PEG.

If the white noise bandwidth is from the points C to D, which means the bandwidth does not contain the resonance frequency of the cantilever beam, this situation can be divided into two cases: if the RMS excitation value is small (the vibration amplitude of the beam can not hit the limited stoppers), the performances of both of them are exactly the same; however, if the excitation is large enough, the performance of the piecewise-linear PEG will be a little bit better. See the results shown in Figure 2.10, the RMS displacement of the piecewise-linear PEG is 1.11 times larger that that of the linear PEG*.

*The result of the RMS comparison is actually randomly distributed between 1 to 1.11, based on our repeated simulations.

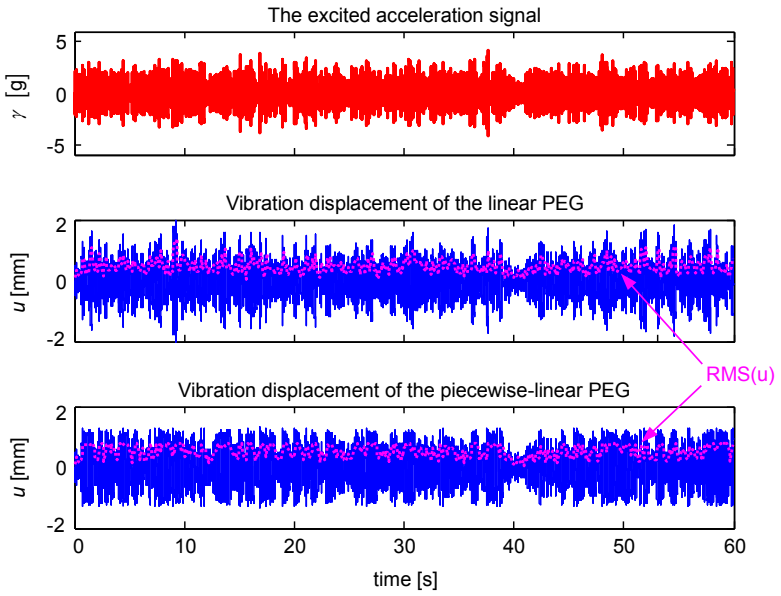

Figure 2.10: The time history of the random excitation, the vibration displacements of the linear PEG and piecewise-linear PEG

2.4 Additional benefits of mechanical stoppers

2.4.1 Frequency up-conversion

The frequency range of the environment vibrations is usually low, typically $10 \sim 100$ Hz. In order to obtain a high power generated from PEGs, a traditional solution is to reduce their resonance frequencies to match the ambient vibration spectrum, so that the oscillator can amplify the vibration displacement and enhance the generated energy per cycle. On the other hand, for a high fundamental frequency intrinsic PEG, even a small amount of mechanical energy can be converted into electrical energy in each strain cycle, higher frequency increases the potential of power generation. Obviously, the frequency match strategy is not always suitable especially when the vibration spectrum is very low. For human-based energy harvesting for instance, the human motions are intrinsically slow, never exceeding a few hertz. In this context, the application of the traditional approach, that is to reduce the resonance frequency of the PEG, would unacceptably lead to increased the encumbrance (e.g. vibration stroke and rigid mass would exceed the allowed range) [128].

Therefore, the need for a technique capable of bridging between the high-frequency response of PEGs and the low-frequency input that is most often available on specific environment and on the human body is clearly needed [128]. Fortunately, due to the plucking or impact excitation techniques, a mechanical stopper composed of a cantilever beam with piezoelectric elements can address the above issue.

Figure 2.11 shows one of the operating principles of the mechanical plucking, where

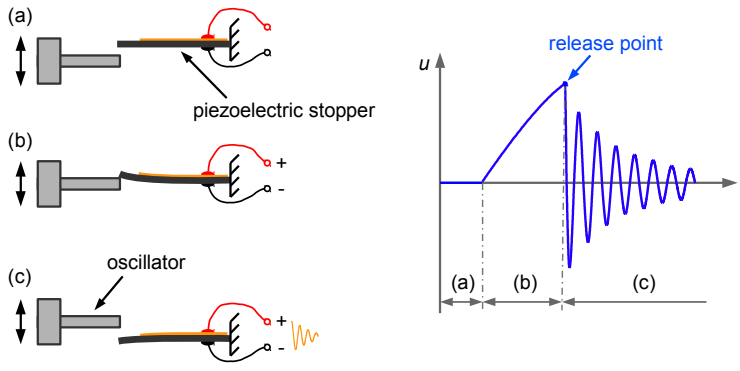

Figure 2.11: The operating principle of a plucked stopper and its vibration displacement waveform [128]

the oscillator vibrating at a very low frequency is used as a plectrum. In stage 'a', the distance between piezoelectric stopper and the plectrum is reduced until they come into contact. Immediately follows the stage 'b', during which both elastic elements are deflected, according to their mechanical compliance: mechanical energy is input in the system in the form of strain energy. As the deflection progresses, the overlap between the two elements is reduced so that their contact area becomes gradually smaller, until contact is lost (release point). From this instant, the piezoelectric stopper vibrates at its resonance frequency around its stable position, see the stage 'c'. As the stopper vibrates, the stored strain energy is mainly converted into electrical energy by the direct piezoelectric effect, part of the energy is however dissipated through various forms of damping. This outcome of plucking is frequency up-conversion, as by one single slow movement of the plectrum, a large number of vibrations are produced at high frequency [128].

Another frequency up-conversion technique is shown in Figure 2.12, where the small cantilever beam noted as PEH-T and the metal package are the mechanical stoppers. The PEG is very similar to the previous presented piecewise-linear PEG except the stoppers are not exactly the same and symmetrically arranged. In the PEG, the resonance frequency of the cantilever beam noted as PEH-B is as low as 36 Hz, while PEH-T exhibits a much high resonance frequency of 618 Hz. When an external excitation with 38 Hz frequency is applied to the PEG, PEH-B vibrates according to the base excitation at 38 Hz. During each vibration cycle, PEH-B impacts the top stopper PEH-T, resulting in a self-oscillation of PEH-T at its high resonance frequency. Due to the much smaller displacement of PEH-T, its generated power is lower. However, comparing the power efficiency defined by the authors (the mean value of output power divided by the tip displacement of the cantilever), the power efficiency of PEH-T is 3.6 times higher than that of PEH-B [129]. Hence, if the top stopper PEH-T is well optimized, it can generate a considerably higher power output which is more suitable for frequency up-conversion technique.

It is worthwhile to highlight the differences between the plucking and impact exci-

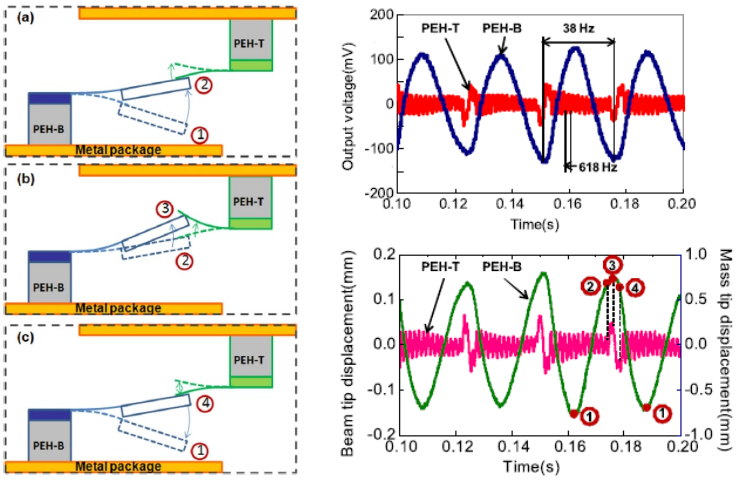

Figure 2.12: A piecewise-linear PEG and its waveforms of the output voltages and vibration displacements [129]

tations. From the physical point of view, impact involves the transfer of momentum; mathematically, the system's initial conditions have none-zero velocity. In plucking excitation, the piezoelectric stopper is slowly deformed and then released; mathematically, the system's initial conditions feature a non-zero displacement [128]. Anyway, both of them can be used in situations where the vibrational energy available is at much lower frequency.

2.4.2 Mechanical switch

Nonlinear EECs which are used to extract the energy generated from PEGs can improve the energy density and the extraction efficiency of VEHDs [34]. At the same time, they introduce synchronous switches which should be precisely controlled in the circuits. Traditionally, these switches in the electronic EEC circuits are composed of electronic elements. They require the electrical energy and voltage or current signals to be correctly driven. Nevertheless, when the external excitation is a random signal, the switching control strategies based on the electronic switches in various nonlinear EECs may become very complicated.

Mechanical switches composed by stoppers and the moving part of the oscillators are passively driven by the vibrations whose energy is being harvested, so they can avoid the issue of complex switching control strategies. In addition, comparing to the electronic switches, the voltage drops or on-resistances of the closed switches can be neglected if the switching contacts are good. According to our knowledge, the first application of the mechanical switch was presented by Giusa et al. in 2013. It is shown in Figure 2.13 [121].

Figure 2.13 shows the prototype, the schematic structure as well as the operating principle of the mechanical switches applied in the SSHI tchnique. Because this approach is particularly suitable for the random excitations, the whole vibration harvesting system is called "random mechanical switching harvester on inductor" (RMSHI) in the reference.

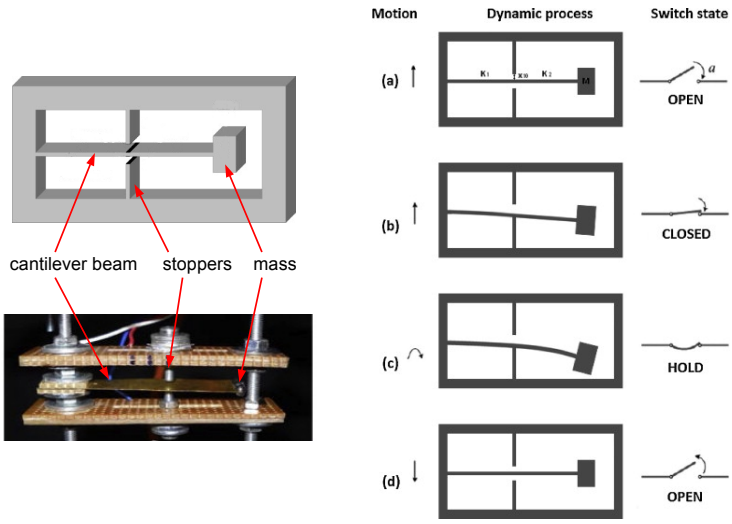

Figure 2.13: Mechanical switch and its operating principle in a piecewise-linear PEG [121]

The mechanical switches, driven by the external vibrations, continually switch between open and close states. Due to the movement of the oscillating beam, the two mechanical stoppers close the electrical circuit, a conductive path is realized between the stoppers and the beam in order to have a short-circuit as soon as the oscillating beam impacts the stopper, and this conductive state will be kept for a short time because of the inertial mass at the free end of the beam. Moreover, according to the authors research, this duration can be regulated by tuning both the horizontal positions and the separation of the stoppers [121].

Benefiting from the advantages of the mechanical switches, they can also be used as diodes in electronic circuits. Maiorca et al. proposed a mechanical H-bridge rectifier composed of four identical mechanical switches. This diode-less technique is particularly suitable for low voltage outputs of PEGs [130].

2.4.3 Enlarge bandwidth of nonlinear PEGs

As talked in the previous section, the mechanical stoppers cause the piecewise-linear stiffness behavior of an originally linear oscillator. This behavior introduce the hardening effect that is capable of increasing the operating bandwidth. Does this behavior also benefit to originally nonlinear PEGs?

Figure 2.14 shows a prototype, a schematic structure, as well as an equivalent electromechanical model of a nonlinear BSM PEG with stoppers. The PEG is based on a lumped spring-mass structure in a buckled configuration, composed of four flexible hinges, two piezoelectric components, two stoppers, a central inertial mass and a frame. Flexible hinges are used to connect the piezoelectric components and inertial mass together with the frame, they are also used to avoid dry friction and lash when the mass vibrates. Two identical elastic stoppers are symmetrically arranged at the both sides of the mass. When

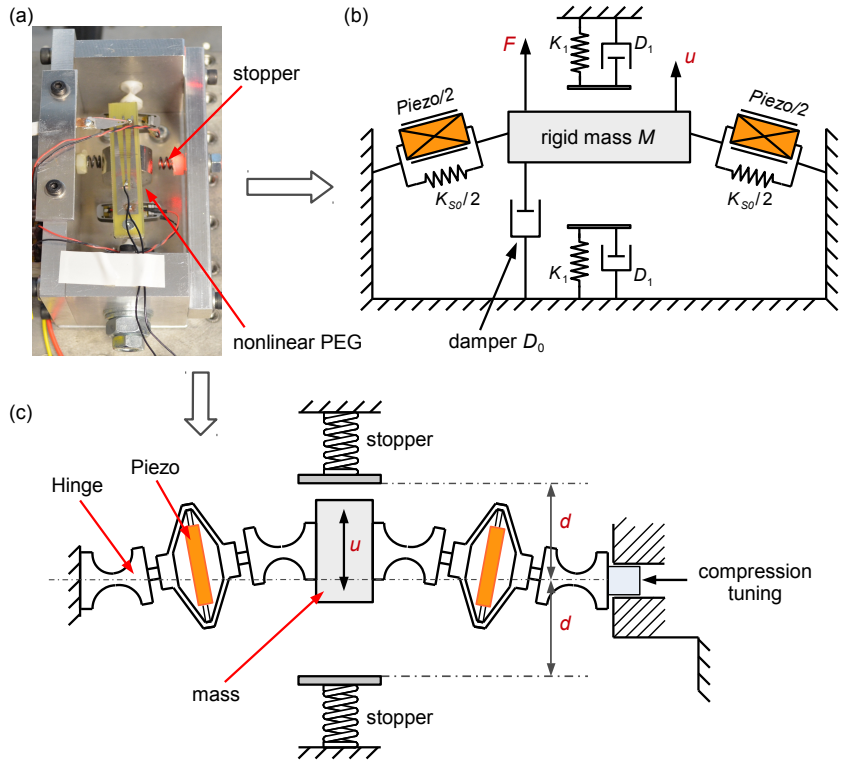

Figure 2.14: Nonlinear PEG: (a) prototype; (b) equivalent electromechanical model; (c) schematic structure [89]

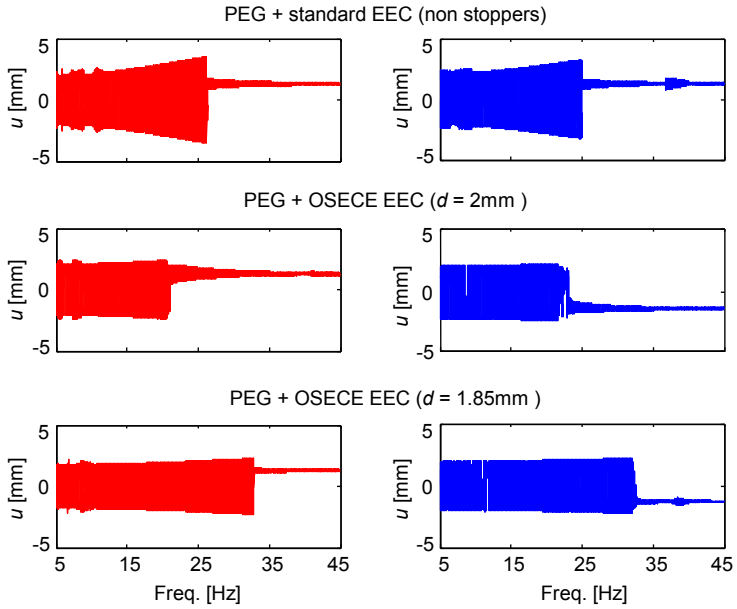

Figure 2.15: Displacement response for the BSM PEG in different cases (left side: experimental; right side: theoretical) [89]

the displacement is large enough to let the mass contact a stopper, the additional stiffness from the stopper presents a more obvious hardening effect than the single bistable oscillator, the bandwidth is then increased in the forward sweep excitation. Besides, the stoppers provide the limitation of the oscillator displacement when over-high excited, and can therefore prevent potential damages.

Figure 2.15 shows the vibration displacement responses of the BSM PEG using the standard EEC and the BSM PEG with stoppers plus the OSECE EEC. For the stoppers position set as $d = 2$ mm, the useful band of the inter-well motions of the oscillator is not increased comparing to the BSM PEG using the standard EEC. This is because the nonlinear OSECE EEC induces a stronger damping effect than that of the standard EEC, the polymer tape of the stopper and the impact also bring the additional damping of the whole device. However, as the limited distance is shorter ($d = 1.85$ mm), the bandwidth is greatly enlarged, this performance is similar as the conclusion that was proposed in the piecewise-linear structure. Comparing to the BSM PEG using the standard EEC, although the damping in the device is higher, the bandwidth is significantly larger. In addition, due to the higher extraction efficiency of the OSECE EEC, the harvested power is always larger than that of the BSM PEG using the standard circuit, though the displacement amplitude is limited in the PEG [89].

According to the above results, the bandwidth increasing effect of the stoppers is clearly demonstrated for nonlinear PEGs.

2.5 Conclusion

This chapter proposes two typical electromechanical generator: linear PEG and piecewise-linear PEG. Their performances under different excitations are discussed. Comparing with the linear PEG, if the excitation is a forward sweep signal, the piecewise-linear PEG can significantly enlarge its operating bandwidth at the detriment of the maximal vibration displacement; if the excitation is a sinusoidal signal but its frequency changes in a large range, the piecewise-linear PEG still has a better performance; if the excitation is a random signal, the performances of the two PEGs are close to each other. Anyway, the stopper in the piecewise-linear PEG can be integrated as the frequency up-converter or the mechanical switch, introducing additional benefits of the VEHD.

The next chapter will present three different EECs (Standard, SECE, OSECE). For the sake of simplicity, their harvested powers will compared for the classical linear PEG proposed in this chapter. However, the combination of the OSECE approach with the piecewise-linear PEG will be discussed in chapter 4.

3

Energy extraction circuits: presentation and comparative study

Contents

3.1 Introduction

EECs are the circuits that interface between PEGs and self-powered electronic devices, they are used to extract and store the electrical energy generated by the PEGs. The standard EEC is a classical interface that is generally studied, however, the energy extraction effectiveness of this interface is not advanced. So many nonlinear EECs have been developed to increase the effectiveness of this energy conversion, the first published approach, called SSHI, consists in connecting a switch and an inductor to the piezoelectric element in parallel or in series [95], the switch is triggered at the displacement extremes of the PEGs, the nonlinear effect generated on the piezoelectric voltage drastically enhances the extracted energy density under the same strain of the piezoelectric element. But on the other side, most of these nonlinear EECs still have the load-dependent issue, and a matching impedance strategy to obtain the maximal power is needed. This matching impedance strategy consists in matching the input impedance value of the EEC to the output impedance of the PEG. Since the piezoelectric impedance is related to the vibration frequency due to its capacitive behavior, and the input impedance value of the EEC is also variable and may depend, for instance, on the storage voltage, this strategy is difficult to implement in practical applications.

An advanced nonlinear EEC known as SECE successfully addresses this load impedance matching issue [107], but the switching closing time in the approach need to be accurately controlled, which is complicated to be achieved in practical stand-alone systems. For this reason, the OSECE EEC aiming at simplifying the switching strategy is presented as an improvement of the former SECE technique [112]. OSECE is a load-weakly-dependent circuit, which is also a favorable characteristic for practical ambient vibration energy harvesting.

In this chapter, applied on a linear PEG presented in the previous chapter, three typical EECs (standard, SECE, OSECE) and their energy extraction principles will be theoretically analyzed and developed. The harvested powers will also be calculated and compared under two sinusoidal excitation cases:

Case u_M: constant vibration amplitude of the inertial mass. The harvesting power is obtained assuming a constant vibration amplitude (u_M) of the inertial mass. It corresponds to either weakly coupled structures or structures when excited far from their natural resonance frequencies.

Case F_M: constant ambient acceleration amplitude. The VEHD is excited at its resonance frequency undergoing a constant amplitude sinusoidal force (F_M). Due to the damping effect induced by the harvesting process [131–133], the vibration amplitude is modified according to the electromechanical coupling factor. It corresponds to inertial VEHD driven at constant external acceleration amplitude γ_M, such as $F_M = M\gamma_M$.

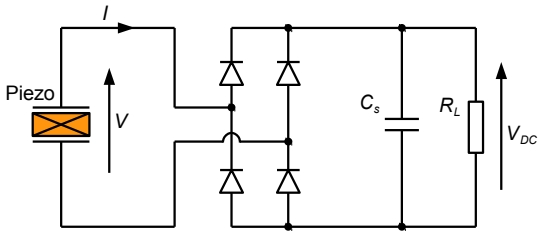

Figure 3.1: Standard circuit

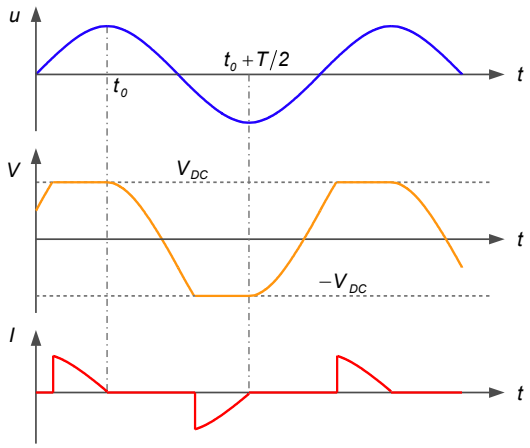

Figure 3.2: Standard waveforms of displacement (u), piezoelectric output voltage (V) and current (I)

3.2 Presentation of EECs

3.2.1 Standard circuit

The standard EEC is shown in Figure 3.1. It includes a full-bridge rectifier and a smoothing/storing capacitor C_s. This is practically the simplest circuit for rectifying and storing an alternating voltage generated from a PEG. The load resistance R_L represents the input impedance of the following electronic module as far as it exhibits a linear behavior.

As the mechanical vibration displacement u is assumed to be purely sinusoidal in steady-state operation, the open-circuit piezoelectric voltage delivered by the linear PEG is sinusoidal too. However, the standard EEC connected to the piezoelectric element changes the waveform of the voltage V. Indeed, the piezoelectric element is open-circuited only when the rectifier bridge is blocking. Once the absolute value of V reaches the load voltage V_{DC}, the rectifier bridge conducts and the piezoelectric element charges the load $\{C_s\ R_L\}$ circuit. The corresponding waveforms of the vibration displacement u, the piezoelectric output voltage V and the outgoing current I are shown in Figure 3.2. The full-bridge rectifier is assumed to be ideal and the rectified voltage V_{DC} is ripple-free.

Standard circuit in case u_M:

In steady-state operation, the average current through the capacitor C_s is null, so the absolute value of the electric charge outgoing from the piezoelectric element during a vibration period T is equal to the average current flowing through the equivalent load resistance R_L. According to the equation 2.3 in chapter 2, the integration expression can be written as equation 3.1. So the load voltage V_{DC} as a function of the vibration amplitude u_M is given in equation 3.2. Then the harvested power is finally calculated in equation 3.3, where ω is the angular frequency of the excitation force.

$$-\frac{V_{DC}}{R_L}\int_{t_0}^{t_0+T/2} \mathrm{d}t = \alpha\int_{t_0}^{t_0+T/2} \dot{u}\,\mathrm{d}t - C_0\int_{t_0}^{t_0+T/2} \dot{V}\,\mathrm{d}t \tag{3.1}$$

$$V_{DC} = \frac{R_L\alpha\omega}{R_L C_0\omega + \frac{\pi}{2}}u_M \tag{3.2}$$

$$P_u^{st} = \frac{V_{DC}^2}{R_L} = \frac{R_L\alpha^2\omega^2}{\left(R_L C_0\omega + \frac{\pi}{2}\right)^2}u_M^2 \tag{3.3}$$

Since the vibration displacement amplitude u_M is constant in this case, according to equation 3.3, the harvested power using the standard EEC reaches a maximum value $P_u^{st\_max}$ for an optimal load resistance R_L^{opt}, given in equations 3.4 and 3.5, respectively. From equation 3.5, it is clearly seen that the optimal load resistance is proportional to the output impedance of the piezoelectric element $(1/C_0\omega)$, whose value is dependent on the excitation frequency. So the matching impedance strategy of the standard approach is complicated to be achieved under wideband excitations.

$$P_u^{st\_max} = \frac{\alpha^2\omega}{2\pi C_0}u_M^2 \tag{3.4}$$

$$R_L^{opt} = \frac{\pi}{2C_0\omega} \tag{3.5}$$

Standard circuit in case F_M:

In this case, the harvesting process induces a damping effect on the mechanical PEG, which leads to a reduction of the vibration amplitude u_M. During a particular half vibration period defined by instants t_0 to $t_0 + T/2$ (Figure 3.2), the electromechanical system's energy balance expressed in equation 2.6 is considered. Because the kinetic energy is null and the elastic energy is the same at those two instants, the external mechanical energy provided to the system is equal to the sum of the mechanical losses and the electrical energy extracted from the PEG, as shown in equation 3.6.

$$\int_{t_0}^{t_0+T/2} F\dot{u}\,\mathrm{d}t = D_0\int_{t_0}^{t_0+T/2} \dot{u}^2\,\mathrm{d}t + \frac{V_{DC}^2}{R_L}\frac{\pi}{\omega} \tag{3.6}$$

As the system operates at the resonance frequency, it can be assumed that the structure displacement remains sinusoidal, for low mechanical damping, the external force and

the velocity are in phase. Under these assumptions, the energy balance equation can be simplified, leading to the expression 3.7 of the displacement amplitude u_M as a function of the external force amplitude F_M. Then, considering equations 3.4 and 3.7, it is possible to get the harvested power P_F^{st} as a function of the external force amplitude.

$$u_M = \frac{F_M}{D_0\omega + \frac{2R_L\omega\alpha^2}{(R_LC_0\omega+\pi/2)^2}} \tag{3.7}$$

$$P_F^{st} = \frac{R_L\alpha^2}{\left(R_LC_0\omega + \frac{\pi}{2}\right)^2} \frac{F_M^2}{\left[D_0 + \frac{2R_L\alpha^2}{(R_LC_0\omega+\pi/2)^2}\right]^2} \tag{3.8}$$

To calculate the maximal harvested power $P_F^{st\_max}$ and the optimal load resistance in case F_M, the four roots R_a, R_b, R_c and R_d of $\left(\partial P_F^{st}/\partial R_L\right)$ are given in equation 3.9 respectively [107]. Of course, R_a is not a physical solution. If the figure of merit $(k_m^2Q_m)$ of the PEG is lower than π, then R_c and R_d are complex solutions, R_b is the only optimal load resistance for which the harvested power reaches a maximum value given in equation 3.10. If the figure of merit of the PEG is larger than π, then the system behavior changes: R_b corresponds to a local minimum of the harvested power and there are two optimal load resistance R_c and R_d, for which the harvested power reaches the maximum value expressed in equation 3.11. It remains constant for a given excited force amplitude.

$$\begin{cases} R_a = -\frac{\pi}{2C_0\omega} \\ R_b = \frac{\pi}{2C_0\omega} \\ R_c = \frac{2\alpha^2 - \pi C_0 D_0\omega - 2\alpha\sqrt{\alpha^2 - \pi C_0 D_0\omega}}{2C_0^2 D_0\omega^2} \\ R_d = \frac{2\alpha^2 - \pi C_0 D_0\omega + 2\alpha\sqrt{\alpha^2 - \pi C_0 D_0\omega}}{2C_0^2 D_0\omega^2} \end{cases} \tag{3.9}$$

$$\begin{cases} P_F^{st\_max} = \frac{\alpha^2\omega}{2\pi C_0} \frac{F_M^2}{(D_0\omega + \alpha^2/\pi C_0)^2} \\ k_m^2Q_m = \frac{\alpha^2}{C_0D_0\omega} < \pi \end{cases} \tag{3.10}$$

$$\begin{cases} P_F^{st\_max} = \frac{F_M^2}{8D_0} \\ k_m^2Q_m = \frac{\alpha^2}{C_0D_0\omega} \geqslant \pi \end{cases} \tag{3.11}$$

A physical interpretation of the changing system behavior can be made considering the influence of the load resistance on the damping. According to equation 3.7, R_b is the load resistance value leading to the strongest damping effect for any figure of merit of the electromechanical structure. When the figure of merit is low, under the condition of the constant mechanical quality factor, the electromechanical coupling coefficient of the structure is weak, so the damping effect due to the load R_b is also weak. Its displacement amplitude allows the structure to receive power from the external excited force. Hence, in this domain it is intuitively understandable that the harvested power increases if the electromechanical coupling is improved. But in the strong coupling domain, the load R_b

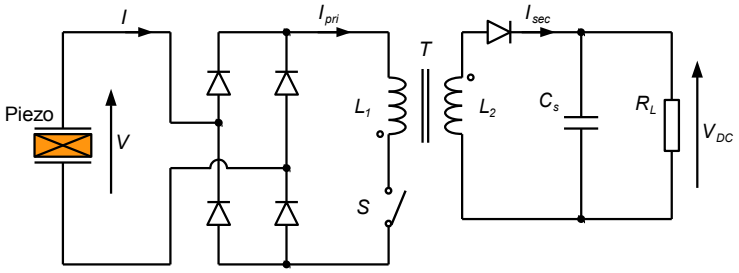

Figure 3.3: SECE circuit

induces a significant damping effect. Since the external driving force has a constant amplitude, the power received by the structure is shift lower because of the strong displacement amplitude reduction. Thus, a reduction in the load resistance to R_c or an increase in the load resistance to R_d allows a larger vibration displacement amplitude, which makes the harvested power return at maximum [107]. In addition, Figure 3.11(a) clearly shows this interpretation.

3.2.2 SECE circuit

The SECE technique consists in extracting all the electric charges accumulated on the piezoelectric element periodically and transferring the corresponding amount of electrical energy to the load circuit. Although this technique has already been presented in the study of Lefeuvre et al. [107], the theoretical development proposed in this thesis includes some electrical losses that were not taken into account in the previous study.

One of the possible implementation of the SECE strategy is shown in Figure 3.3: On the transformer's primary side, the piezoelectric element is connected to a full-bridge rectifier, followed by the primary inductance L_1 in series with an electronic switch S. The secondary inductor L_2 is connected to a rectifying diode D, followed by a smoothing capacitance C_s and an equivalent load resistance R_L. Some assumptions are made in order to simplify analytical calculations: the magnetic circuit is linear and the coupling between the primary and the secondary windings is ideal; on state voltage drops of switches and diodes are neglected; the output voltage V_{DC} is ripple-free.

Figure 3.4 shows the theoretical waveforms of the displacement, the piezoelectric voltage and the current, as well as the switch control signal. Most of the time, the piezoelectric element is in open-circuit configuration (S is open). As soon as the displacement reaches an extremum (maximum or minimum), so do the voltage on the piezoelectric element ($\pm V_M$), as it is proportional to the structure displacement. The switch S is then closed for a short time t_{SECE}. Considering the capacitive behavior of the piezoelectric element, the left part of the circuit is an oscillating $r_I L_1 C_0$ circuit*. The differential equation governing the

*r_I is some equivalent resistance encompassing the resistive and magnetic losses.

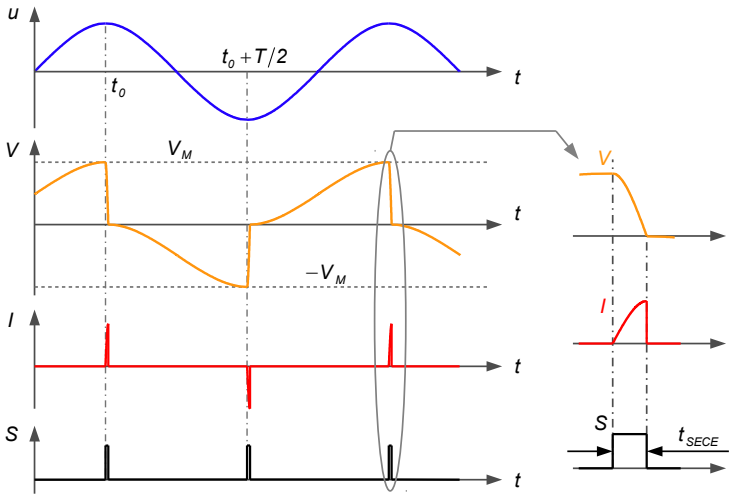

Figure 3.4: SECE waveforms of displacement (u), voltage (V), current (I), and switch control signal (S)

electrical charge q_0 on the piezoelectric element is given by equation 3.12. Considering the initial conditions $q_0(0) = C_0 V_M$ and $\dot{q_0}(0) = 0$, the current I_{pri} can be expressed as 3.13, where ω_I and Q_I are the natural angular frequency and the quality factor of this oscillating circuit, respectively.

$$L_1 \ddot{q_0} + r_I \dot{q_0} + \frac{q_0}{C_0} = 0 \tag{3.12}$$

$$I_{pri} = \dot{q_0} = C_0 V_M \frac{\omega_I}{\sqrt{1-(1/2Q_I)^2}} \sin\left(\sqrt{1-(1/2Q_I)^2}\,\omega_I t\right) \mathrm{e}^{-\frac{\omega_I t}{2Q_I}} \tag{3.13}$$

$$\omega_I = \frac{1}{\sqrt{L_1 C_0}}, \quad Q_I = \frac{1}{r_I}\sqrt{\frac{L_1}{C_0}} \tag{3.14}$$

Because the switch S is closed and the diodes are assumed ideal, the voltage across the piezoelectric element equals the voltage across the primary inductor. Thus, it can be expressed as:

$$V = L_1 \ddot{q_0} = \frac{V_M}{\sqrt{1-(1/2Q_I)^2}} \cos\left(\sqrt{1-(1/2Q_I)^2}\,\omega_I t + \arcsin(1/2Q_I)\right) \mathrm{e}^{-\frac{\omega_I t}{2Q_I}} \tag{3.15}$$

To limit electromagnetic losses, the quality factor Q_I should be as high as possible. If it is larger than 5, $(1/2Q_I)$ is a small value compared to 1, the second order term $(1/2Q_I)^2$ can be ignored, and the phase difference between the voltage and the current can be considered as $\pi/2$. Equations 3.13 and 3.15 can then be simplified into equations 3.16 and 3.17, respectively.

$$I_{pri} = \sqrt{\frac{C_0}{L_1}} V_M \sin(\omega_I t)\, \mathrm{e}^{-\frac{\omega_I t}{2Q_I}} \tag{3.16}$$

$$V = V_M \sin\left(\omega_I t - \frac{\pi}{2}\right) \mathrm{e}^{-\frac{\omega_I t}{2Q_I}} \tag{3.17}$$

The switch is open again as soon as the voltage across the piezoelectric element reaches 0. From equation 3.17, the duration time t_{SECE} can be obtained as shown in equation 3.18, which also corresponds to a quarter of the oscillating period of the primary $r_I L_1 C_0$ circuit. Hence, the value of the current flowing through L_1 at this moment can be expressed as equation 3.19 and corresponds to a maximum.

$$t_{SECE} = \frac{\pi}{2\omega_I} = \frac{\pi}{2}\sqrt{L_1 C_0} \tag{3.18}$$

$$I_{pri} = I_M = \sqrt{\frac{C_0}{L_1}} V_M \mathrm{e}^{-\frac{\pi}{4Q_I}} \tag{3.19}$$

During the switch closing time, all the accumulated electric charges are extracted and most part are transferred to the transformer primary inductor L_1, except the losses in the equivalent resistance r_I. It is called electric charges extraction phase, the energy stored on the inductor L_1 after this process can be expressed as equation 3.20, this energy is assumed to be totally discharged through L_2 to the load circuit $\{C_s\ R_L\}$ at last.

$$E_L = \frac{1}{2} L_1 I_M^2 = \frac{1}{2} C_0 V_M^2 \mathrm{e}^{-\frac{\pi}{2Q_I}} \tag{3.20}$$

SECE circuit in case u_M:

In steady-state operation of the SECE approach, the piezoelectric current I is null except during the energy extraction phases, which means the piezoelectric element is almost always in open-circuit condition. So integrating equation 2.3 over the time between instant t_0 and $t_0 + T/2$ leads to equation 3.22 that gives the relationship between the maximum voltage V_M and the displacement amplitude u_M. As the electric charges are extracted twice a vibration period, the harvested power in this case is finally expressed in equation 3.23.

$$\alpha \int_{t_0}^{t_0+T/2} \dot{u}\, \mathrm{d}t - C_0 \int_{t_0}^{t_0+T/2} \dot{V}\, \mathrm{d}t = 0 \tag{3.21}$$

$$V_M = 2\frac{\alpha}{C_0} u_M \tag{3.22}$$

$$P_u^{SECE} = E_L \frac{\omega}{\pi} = \frac{2\alpha^2 \omega}{\pi C_0} \mathrm{e}^{-\frac{\pi}{2Q_I}} u_M^2 \tag{3.23}$$

From the expression of the harvested power, it can be clearly seen that the SECE circuit is a totally load-independent EEC, and we do not need to care about the impedance matching issue. If the quality factor Q_I is large enough, then the harvested power is almost 4 times higher than the maximal power $P_u^{st\_max}$ obtained in the standard EEC.

SECE circuit in case F_M:

In this case, the electromechanical system's energy balance during half a vibration period between the instants t_0 to $t_0 + T/2$ is still considered. Since the kinetic energy is null and the elastic energy is the same at those two instants, the external mechanical energy provided to the system is distributed into the mechanical losses and the electrical energy extracted from the piezoelectric element, as shown in equation 3.24.

$$\int_{t_0}^{t_0+T/2} F\dot{u}\,\mathrm{d}t = D_0 \int_{t_0}^{t_0+T/2} \dot{u}^2\,\mathrm{d}t + \frac{1}{2}C_0 V_M^2 \tag{3.24}$$

As the system works at the resonance frequency, it can be assumed that the structure displacement remains sinusoidal, for low mechanical damping, the external force and the velocity are in phase. Under these assumption, the energy balance can be simplified, leading to the expression 3.25 of the displacement amplitude u_M as a function of the external force amplitude F_M. Then the harvested power can be easily expressed in equation 3.26.

$$u_M = \frac{F_M}{D_0\omega + \frac{4\alpha^2}{\pi C_0}} \tag{3.25}$$

$$P_F^{SECE} = \frac{2\alpha^2}{\pi C_0 \omega} \frac{F_M^2}{\left(D_0 + \frac{4\alpha^2}{\pi C_0 \omega}\right)^2} \mathrm{e}^{-\frac{\pi}{2Q_I}} \tag{3.26}$$

This expression also shows that the power does not depend on the load resistance, which is notably favorable for wideband vibration energy harvesting. In addition, these results in two cases are both consistent with reference [107], but losses in the left part of the circuit are now taken into account during the electric charge extraction phases.

Discussion about the switch closing time:

Equation 3.18 gives the accurate value of the theoretical switch closing time t_{SECE} in the original SECE technique. It equals a quarter of the $r_I L_1 C_0$ oscillating period which is constant in a given SECE EEC. In order to optimize the performances of the SECE approach, the real switch closing time need to be precisely controlled eventually. However, since the circuit oscillating frequency is very high, t_{SECE} is brief ($10^0 \sim 10^2$ µs) and difficult to be achieved in a simple stand-alone system. If the real closing time is too short, the electric charge accumulated on the piezoelectric element will only be partly extracted in this original technique; if it is too long, the electrical energy stored in the inductor will be gradually dissipated on r_I. Figure 3.5 shows one of the practical examples of the presented issues, in which the switching closing time is much longer than the precise t_{SECE}.

The precise t_{SECE} ends as soon as the primary current reaches maximum, the voltage difference between the two piezoelectric electrodes is 0. However, due to the threshold voltage of the diodes in the practical circuit, the absolute electrode voltage is not exactly zero compared to the ground level signal (typically −0.6 V), so do the voltage across the

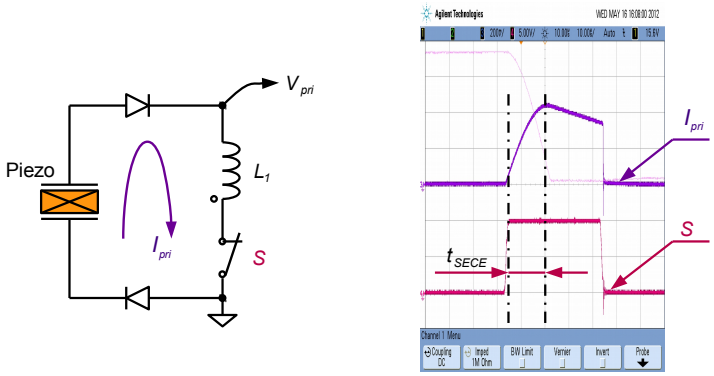

Figure 3.5: Energy extraction phase in the long switch closing time

primary inductor V_{pri} (typically -1.2 V). If the switch is still closed after this instant, the primary current value will decrease according to the law of electromagnetic induction expressed in equation 3.27. So the energy stored in the flyback transformer will also decrease proportionally to the square value of I_{pri}. In addition, the decreased energy is dissipated on the primary equivalent resistance r_I.

$$V_{pri} = -L_1 \frac{\mathrm{d}}{\mathrm{d}t} I_{pri} \tag{3.27}$$

3.2.3 OSECE circuit

For the aforementioned reasons discussed in the previous section, a new EEC based on the SECE technique but with a simplified switch control strategy is proposed. Figure 3.6 shows the schematic of this EEC. A transformer with two primary windings and one secondary winding divides this interface circuit into two parts. The left part of this circuit is very similar to the SSDI circuit, including the switch control signal [96, 134]. The right part is a load circuit, which consists of a smoothing/storing capacitor C_s and an equivalent load R_L. Comparing with the original SECE approach, some main features of the OSECE approach are presented in the following:

- Only one diode threshold voltage drop is faced in the primary side.
- The negative pole of the piezoelectric element and the circuit share a common ground, which greatly simplifies the implementation of the VEHD (e.g. piezoelectric sensor can share a common ground signal in this system).
- During the energy extraction phase, a fraction of the electric charge stored in the inductor directly flows back to the piezoelectric material through the closing switch. It set an initial voltage up on the piezoelectric element which enhances the electrical energy density of the PEGs [110].

Using the same assumptions as for the SECE EEC, Figure 3.7 mainly shows the three stages (1, 2, -) of the operation principle of this approach during one semi-period, and Figure 3.8 shows the detailed waveforms of voltages and currents in the circuit.

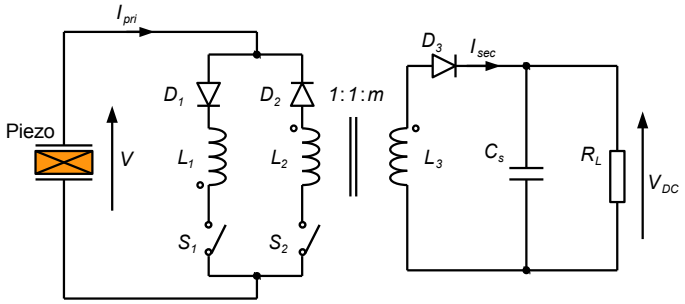

Figure 3.6: OSECE circuit

Before stage '1' (stage '+' shown in the figures), the displacement u is supposed to be increasing; the switches and diodes conditions are the following: S_1 is open, S_2 is closed, D_1 is on and D_2 is off. The piezoelectric element is open-circuited, the piezoelectric voltage V is positive and in phase with the displacement u.

Stage '1' starts as soon as the displacement reaches a maximum (the voltage on the piezoelectric element is also maximal as they are in phase), the switch S_2 is opened and the switch S_1 is closed. At this moment, diode D_1 is conducting, so the primary inductor L_1 is connected to the piezoelectric element. Due to the capacitive behavior of the piezoelectric element, this part of the circuit will works as an oscillating circuit for the short time t_m shown in Figure 3.8. As previously shown for the SECE approach, the current in this circuit and the voltage across the primary inductor can be expressed by 3.28 and 3.29 respectively. The voltage across the secondary winding can be expressed by 3.30, where m is the secondary-primary turns ratio of the transformer. The two voltages V_{pri} and V_{sec} are shown in Figure 3.8 respectively (for stage '+', V_{pri} is actually the voltage across the second primary inductor L_2 and equals 0).

The stage '1' ends when V_{sec} reaches V_{DC} at $t = t_m$. The energy stored in the transformer is then expressed by 3.31, where I_m is the value of the current in the primary at this specific time. The range value of t_m is given in equation 3.32.

$$I_{pri} = \sqrt{\frac{C_0}{L_1}} V_M \sin(\omega_I t)\, \mathrm{e}^{-\frac{\omega_I t}{2Q_I}} \tag{3.28}$$

$$V_{pri} = V = V_M \cos(\omega_I t)\, \mathrm{e}^{-\frac{\omega_I t}{2Q_I}} \tag{3.29}$$

$$V_{sec} = -mV_{pri} \tag{3.30}$$

$$E_L = \frac{1}{2} L_1 I_m^2 = \frac{1}{2} C_0 V_M^2 \sin^2(\omega_t t_m)\, \mathrm{e}^{-\frac{\omega_I t}{Q_I}} \tag{3.31}$$

$$\frac{\pi}{2} < \omega_I t_m < \pi \tag{3.32}$$

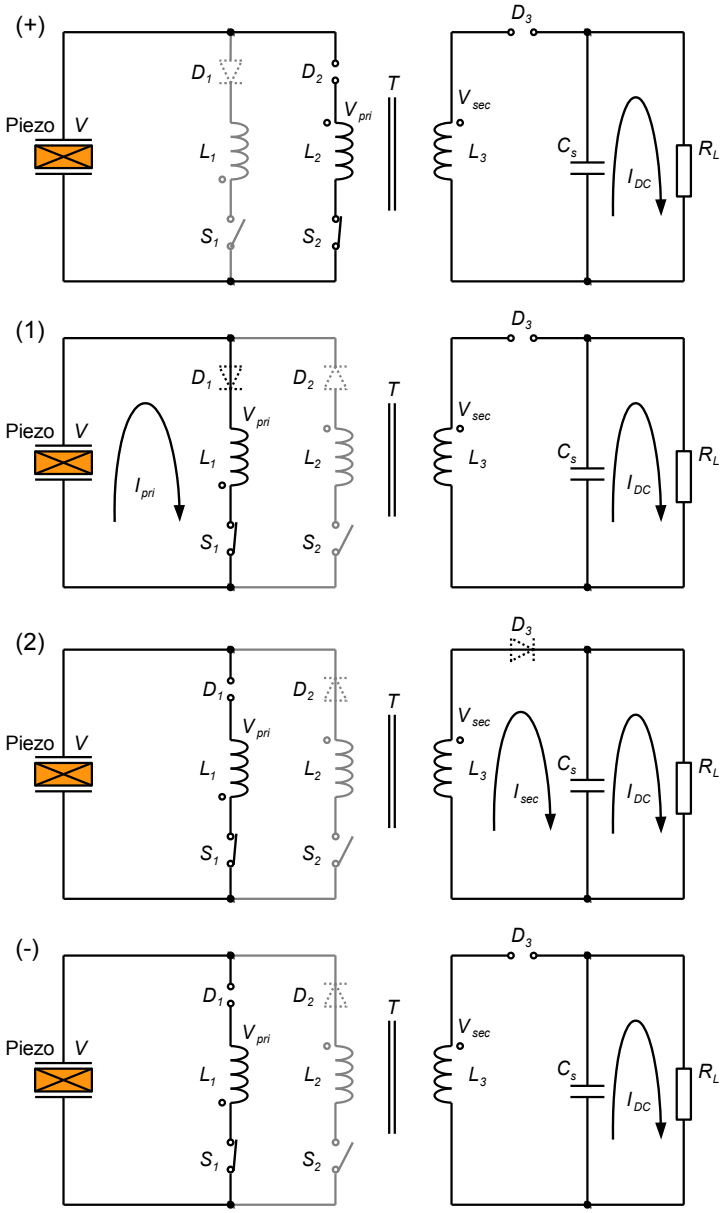

Figure 3.7: Energy extraction principle of the OSECE circuit, stage (+): piezoelectric element is in open-circuit condition and its voltage is positive; stage (1): energy extraction phase; stage (2): charging phase; stage (-): piezoelectric element is in open-circuit condition and its voltage is negative

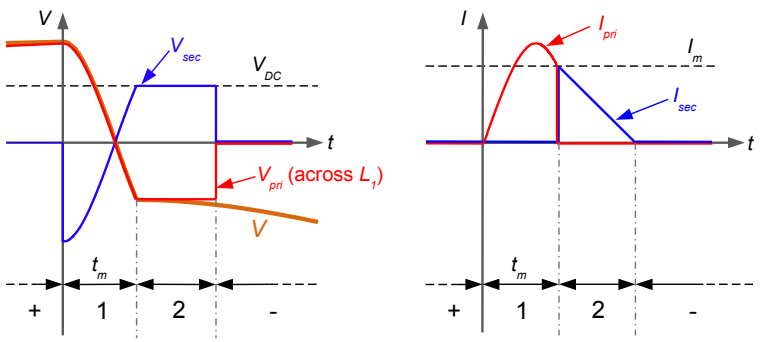

Figure 3.8: OSECE waveforms of the voltages and currents around the energy extraction and charging phases ($m = 1$)

During the stage '2', V_{sec} equals V_{DC}, and the extracted electrical energy expressed by 3.31 is transferred from the transformer to the $\{C_s\ R_L\}$ circuit. The voltage across the diode D is no longer reverse biased, so the secondary winding is connected to the load and V_{sec} is kept constant till the current I_{sec} becomes 0. According to the transformer principle, V_{pri} is also kept constant. Since the displacement of the mechanical structure is still decreasing, so do the voltage V on the piezoelectric element. During this phase, the diode D_1 is reverse biased since V is lower than V_{pri}, and then the piezoelectric element is in open-circuit condition.

The stage '-' occurs when the energy stored in the transformer is completely transferred to $\{C_s\ R_L\}$ circuit (i.e. the current I_{sec} reaches 0). During this stage, the capacitor C_s continues to supply uninterrupted voltage to the load R_L. The vibration displacement is still decreasing, the switches and diodes conditions are the following: S_1 is closed, S_2 is open, D_1 is off and D_2 is on. The piezoelectric element is open-circuited again, the piezoelectric voltage V is then in phase with the displacement u, but the value becomes negative. This stage will end when the displacement reaches a minimum.

The next stages will be similar to stage '1', '2' and '-' but with reverse piezoelectric voltage and through the second primary inductor.

Finally, Figure 3.9 shows the OSECE typical waveforms of the displacement, the piezoelectric voltage and current, as well as the switch control signal for one full period. When the displacement reaches a maximum (or a minimum), the switches states are reversed, the electric charges accumulated on the piezoelectric element are then transferred to the primary inductor L_1 (or L_2). When the value of the current I_{pri} reaches its maximum, all the electric charges have been extracted and the voltage difference between the piezoelectric electrodes is 0. At this moment, as the switch is still closed and the diode is in conduction state, the energy stored in the primary inductor L_1 (or L_2) will flow back to the piezoelectric material. This gives an initial voltage on the piezoelectric element similarly to the initial energy injection technique [110].

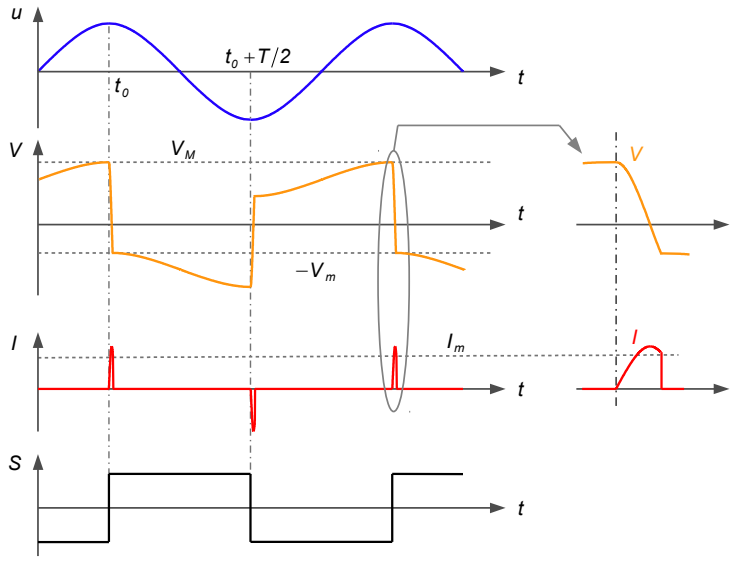

Figure 3.9: OSECE waveforms of displacement (u), voltage (V), current (I), and switch control signal (S)

When V_{sec} reaches V_{DC}, the piezoelectric element is open-circuited again because the diode in series with the closed switch will be reversed biased. The voltage V_m on the piezoelectric element is then equal to the voltage across the primary inductor, and is given by 3.33. The extracted energy stored in the magnetic field of the transformer is then transformed to the $\{C_s\ R_L\}$ circuit, which leads to equation 3.34.

$$V_m = V_{pri} = \frac{V_{DC}}{m} = -V_M \cos(\omega_I t_m)\, \mathrm{e}^{-\frac{\omega_I t_m}{2Q_I}} \tag{3.33}$$

$$E_L = \frac{V_{DC}^2}{R_L}\frac{\pi}{\omega} \tag{3.34}$$

OSECE circuit in case u_M:

As the piezoelectric element is open-circuited in stage '-', the outgoing current I is null. Integrating equation 2.3 over the time between instant t_0 and $t_0 + T/2$ (shown in equation 3.35) leads to equation 3.36 which gives the relationship between the maximum piezoelectric voltage V_M and the displacement amplitude u_M.

$$\alpha \int_{t_0}^{t_0+T/2} \dot{u}\, \mathrm{d}t - C_0 \int_{t_0}^{t_0+T/2} \dot{V}\, \mathrm{d}t = 0 \tag{3.35}$$

$$V_M = V_m + \frac{2\alpha}{C_0} u_M \tag{3.36}$$

The harvested energy during a semi-vibration-period is given by 3.31 and 3.34, from the above equations, the load voltage V_{DC} can be expressed as a function of the displacement amplitude u_M, the load resistance R_L, the turns ratio m and the quality factor Q_I of the

oscillating circuit, as shown in equation 3.37. Then the harvested power using OSECE EEC in case u_M is finally given by equation 3.38.

$$\begin{cases} V_{DC} = -\frac{2m\alpha}{C_0} \frac{\cos(\omega_I t_m) \mathrm{e}^{-\frac{\omega_I t_m}{2Q_I}}}{1+\cos(\omega_I t_m) \mathrm{e}^{-\frac{\omega_I t_m}{2Q_I}}} u_M \\ \omega_I t_m = \arctan\left(-m\sqrt{\frac{2\pi}{R_L C_0 \omega}}\right) + \pi \end{cases} \tag{3.37}$$

$$\begin{cases} P_u^{OSECE} = \frac{2\alpha^2\omega}{\pi C_0} \frac{\sin^2(\omega_I t_m) \mathrm{e}^{-\frac{\omega_I t_m}{Q_I}}}{\left[1+\cos(\omega_I t_m) \mathrm{e}^{-\frac{\omega_I t_m}{2Q_I}}\right]^2} u_M^2 \\ \omega_I t_m = \arctan\left(-m\sqrt{\frac{2\pi}{R_L C_0 \omega}}\right) + \pi \end{cases} \tag{3.38}$$

OSECE circuit in case F_M:

Considering the electromechanical system's energy balance during half a vibration period between the instants t_0 to $t_0 + T/2$, leads to equation 3.39. The external mechanical energy provided to the system is distributed into the mechanical losses and the electrical energy extracted from the piezoelectric element. At the resonance, assuming that the displacement is sinusoidal, and for low mechanical damping, the force and velocity are in phase, equation 3.39 can be simplified and leads to the expression of the displacement amplitude u_M as a function of the external force amplitude F_M (equation 3.40). Substituting equation 3.40 into equation 3.38 can easily lead to the expression 3.41 of the harvested power.

$$\int_{t_0}^{t_0+T/2} F\dot{u}\,\mathrm{d}t = D_0 \int_{t_0}^{t_0+T/2} \dot{u}^2\,\mathrm{d}t + \frac{1}{2}C_0\left(V_M^2 - V_m^2\right) \tag{3.39}$$

$$u_M = \frac{F_M}{D_0\omega + \frac{4\alpha^2}{\pi C_0} \frac{1-\cos(\omega_I t_m) \mathrm{e}^{-\frac{\omega_I t_m}{2Q_I}}}{1+\cos(\omega_I t_m) \mathrm{e}^{-\frac{\omega_I t_m}{2Q_I}}}} \tag{3.40}$$

$$\begin{cases} P_F^{OSECE} = \frac{2\alpha^2}{\pi C_0 \omega} \frac{\sin^2(\omega_I t_m) \mathrm{e}^{-\frac{\omega_I t_m}{Q_I}}}{\left[1+\cos(\omega_I t_m) \mathrm{e}^{-\frac{\omega_I t_m}{2Q_I}}\right]^2} \frac{F_M^2}{\left[D_0 + \frac{4\alpha^2}{\pi C_0 \omega} \frac{1-\cos(\omega_I t_m) \mathrm{e}^{-\frac{\omega_I t_m}{2Q_I}}}{1+\cos(\omega_I t_m) \mathrm{e}^{-\frac{\omega_I t_m}{2Q_I}}}\right]^2} \\ \omega_I t_m = \arctan\left(-m\sqrt{\frac{2\pi}{R_L C_0 \omega}}\right) + \pi \end{cases} \tag{3.41}$$

3.3 Theoretical performance comparisons

The aim of this section is to compare the theoretical harvested power for the above-mentioned EECs in the two excitation cases. In order to make the comparison as generic as possible, several dimensionless parameters are listed in Table 3.1.

Table 3.1: Dimensionless parameters

Parameter	Expression	Definition
ξ_R	$\frac{2R_L C_0 \omega}{\pi}$	Load resistance coefficient
$k_m^2 Q_m$	$\frac{\alpha^2}{C_0 D_0 \omega}$	Figure of merit of the electromechanical structure
Q_I	$\frac{1}{r_I}\sqrt{\frac{L_1}{C_0}}$	Quality factor of the $r_I L_1 C_0$ oscillating circuit

Table 3.2: Normalized harvested powers in case u_M

EECs	Case u_M
standard	$\bar{P}_u^{st} = 4\frac{\xi_R}{(1+\xi_R)^2}$
SECE	$\bar{P}_u^{SECE} = 4\mathrm{e}^{-\frac{\pi}{2Q_I}}$
OSECE	$\begin{cases} \bar{P}_u^{OSECE} = 4\dfrac{\sin^2(\omega_I t_m)\mathrm{e}^{-\frac{\omega_I t_m}{Q_I}}}{\left[1+\cos(\omega_I t_m)\mathrm{e}^{-\frac{\omega_I t_m}{2Q_I}}\right]^2} \\ \omega_I t_m = \arctan\left(-\frac{2m}{\sqrt{\xi_R}}\right) + \pi \end{cases}$

3.3.1 Harvested powers in case u_M

The definition of the load resistance coefficient ξ_R is established by following the procedure described in Arroyo et al. [42]. Equation 3.5 shows that when ξ_R equals to 1, the load impedance would maximize the harvested power using the standard EEC. The new maximal power expression derived from equation 3.4 is then given in 3.42. It can be clearly seen that using the standard EEC, the maximal harvested power is proportional to the inertial mass M of a PEG; the vibration pulsation frequency ω; the squared of the coupling coefficient k_m; the squared of the vibration velocity amplitude (ωu_M). All the following harvested powers in case u_M will be normalized with respect to this maximal power, see Table 3.2.

$$P_u^{max} = \frac{\alpha^2 \omega}{2\pi C_0} u_M^2 = \frac{k_m^2}{2\pi} M\omega \left(\omega u_M\right)^2 \tag{3.42}$$

Figure 3.10 shows the curves of the normalized harvested powers as a function of load resistance coefficient ξ_R. Equations and plots clearly show that performances of both standard and OSECE techniques depend on the load. Moreover, in the case of the OSECE circuit, the turns ratio m also plays an important role: As shown in Figure 3.10, larger values of m lead to larger band of load resistances for which the harvested power is increased compared to the SECE case. If m is infinite, the results will be the same as that in the SECE case. This conclusion can be also construed from the normalized equations. However, it is worth noting that large value of m will usually induce larger losses in the

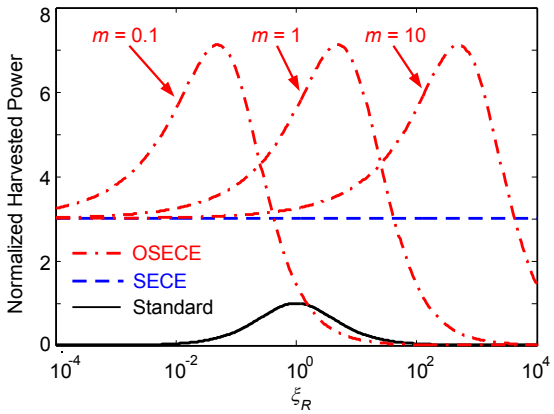

Figure 3.10: Normalized harvested powers in case u_M ($Q_I = 5.5$)

flyback transformer that are not taken into account in the theoretical calculation. Finally, turns ratios between 1 and 5 are considered to be suitable values.

The quality factor Q_I is also important to maximize the harvested power: it should be as high as possible. In Figure 3.10, it has been set to 5.5, which corresponds to the experimental value of the setup proposed in this thesis.

3.3.2 Harvested powers in case F_M

Previous results established for the standard EEC have show that the maximal power that can be harvested is given by equation 3.11. Normalizing the harvested powers with respect to this limit power gives the equations shown in 3.3. It is clearly shown that the harvested powers using both standard and OSECE EECs depend on the figure of merit $k_m^2 Q_m$ of a PEG and the load resistance coefficient ξ_R. Figure 3.11 shows the variations of the normalized harvested power as a function of $k_m^2 Q_m$ and ξ_R. The plots exhibit that when the value of $k_m^2 Q_m$ is low, the SECE and OSECE EECs can harvest higher power, and the powers are load-independent in the SECE approach, load-weakly-dependent in the OSECE approach (the larger the m, the lower the dependency).

Figure 3.12 shows the maximal normalized powers as a function of $k_m^2 Q_m$, which means that the value of ξ_R is optimized for both the standard and OSECE approaches. The curves are always lower or equal to 1, which confirm that the harvested powers in this case are always lower than the limit power given in equation 3.11. The limit power is only obtained using the standard approach, for $k_m^2 Q_m \geqslant \pi$. It is worthy of note that practical application of the standard technique would call for a load adaptation interface. This would induce additional losses that are not taken into account in this theoretical analysis.

This limit power cannot be obtained using the SECE and OSECE EECs because of energy losses due to the quality factor Q_I of the oscillating circuit (it would be reached for $Q_I = +\infty$). However, most of VEHDs exhibit the figure of merits $k_m^2 Q_m$ lower than 1 [47]; in this case, the interest of the OSECE and SECE circuit is clearly shown: the same power

Table 3.3: Normalized harvested powers in case F_M

EECs	Case F_M
standard	$\bar{P}_F^{st} = \frac{\pi k_m^2 Q_m}{\left[\frac{\pi}{4}+\frac{\xi_R}{(1+\xi_R)^2}k_m^2 Q_m\right]^2}\frac{\xi_R}{(1+\xi_R)^2}$
SECE	$\bar{P}_F^{SECE} = \frac{\pi k_m^2 Q_m}{\left[\frac{\pi}{4}+k_m^2 Q_m\right]^2}\mathrm{e}^{-\frac{\pi}{2Q_I}}$
OSECE	$\begin{cases} \bar{P}_F^{OSECE} = \frac{\pi k_m^2 Q_m}{\left[\frac{\pi}{4}+\frac{1-\cos(\omega_I t_m)e^{-\frac{\omega_I t_m}{2Q_I}}}{1+\cos(\omega_I t_m)e^{-\frac{\omega_I t_m}{2Q_I}}}k_m^2 Q_m\right]^2}\frac{\sin^2(\omega_I t_m)e^{-\frac{\omega_I t_m}{Q_I}}}{\left[1+\cos(\omega_I t_m)e^{-\frac{\omega_I t_m}{2Q_I}}\right]^2} \\ \omega_I t_m = \arctan\left(-\frac{2m}{\sqrt{\xi_R}}\right)+\pi \end{cases}$

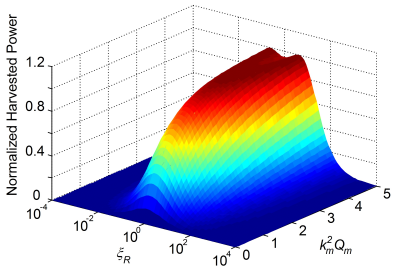

(a) Harvested power using the standard EEC

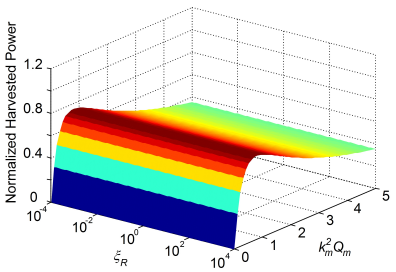

(b) Harvested power using the SECE EEC

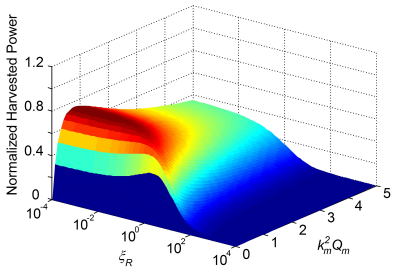

(c) Harvested power using the OSECE EEC ($m = 1$)

Figure 3.11: Normalized harvested power as a function of figure of merit and load rsistance coefficient in case F_M ($Q_I = 5.5$)

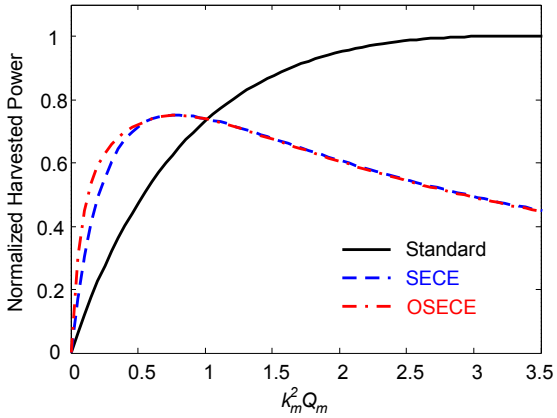

Figure 3.12: Maximal normalized powers in case F_M ($Q_I = 5.5$)

Table 3.4: The dimensions of the PEG

	Steel beam	PZT insert
Length	105 mm	60 mm
Width	32 mm	25 mm
Thickness	1 mm	0.2 mm

as harvested with the standard approach can be obtained, but for a much lower value of $k_m^2 Q_m$. This means that either the amount of piezoelectric material can be reduced (which decreases k_m), or the bandwidth can be enlarged (decreasing Q_m) for the same harvested power.

3.4 Experimental validation and discussion

3.4.1 Experimental setup

The experimental VEHD, as shown in Figure 3.13, is composed of a PEG, an EEC and a programmable load resistance box. The PEG is a classical cantilever beam clamped at one end. A piezoelectric layer is bonded on the surface of this beam, close to the clamped edge, see Figure 3.13(b). The dimensions of this electromechanical structure are shown in Table 3.4. The beam is excited by an external force generated by an electromagnet. The free-end displacement of the cantilever beam is measured by a laser displacement sensor (LD1607-10, MicroEpsilon©). In addition, the electromechanical coupling coefficient of the global structure can be tuned (decreased) by connecting capacitors in parallel with the piezoelectric layer.

In this experiment, the synchronous switch control signals of the SECE and OSECE approaches are generated by a real-time rapid prototyping solution (dSPACE©). To evaluate the performances of the EECs, a resistance box has been specially developed for this

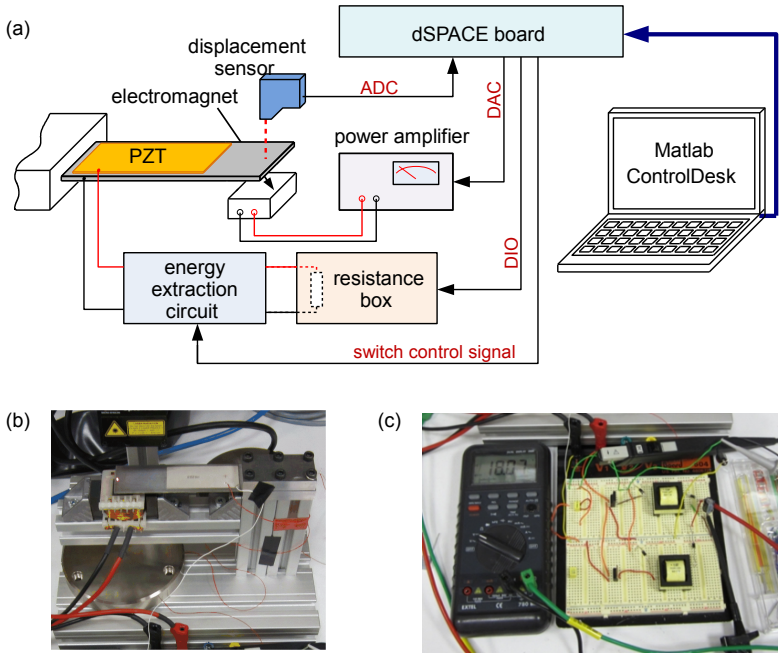

Figure 3.13: Experimental setup: (a) schematic of the experimental setup, (b) PEG, (c) OSECE EEC

experiment. Using this box, the value of the load resistance can be selected conveniently by the digital input/output (DIO) of the dSPACE solution. The detail introduction of this programmable load resistance box can be seen in appendix B of the thesis.

In the SECE EEC, the flyback transformer has only one primary winding (400 µH) and one secondary winding (400 µH). The switch S is a N-channel MOSFET. A high level voltage (10 V) from a digital-to-analog converter (DAC) output of the dSPACE solution can directly drive the switch to close.

The transformer used for the OSECE EEC should have two primary windings (400 µH) and one secondary winding (400 µH). However, for practical reason, in this experiment, we use two same transformers to implement the OSECE EEC, as shown in Figure 3.13(c). Each of them having one primary and one secondary windings. The behavior is exactly same as the implementation illustrated in the schematic of the OSECE circuit, provided that both secondary winding are followed by a rectifying diode and connected in parallel. The switch S_1 in the circuit is a N-channel MOSFET, but the switch S_2 is a P-channel MOSFET which is driven by a negative high level voltage (-10 V).

In both circuit, ultrafast silicon rectifier diodes (UF4003) are used and the circuit load R_L is the programmable resistance box. In order to generate ripple free DC voltage, a 47 µF smoothing capacitor is connected to the resistance box in parallel, so that the time constant $R_L C_s$ is much larger than half of the vibration period. The DC voltage is acquired by the dSPACE solution to calculate the harvested power.

Table 3.5: Definitions of the experimental measurements

Parameter	Symb	Value
Short-circuit resonance frequency	f_0	77.148 Hz
Open-circuit resonance frequency	f_1	78.223 Hz
Open-circuit mechanical quality factor	Q_m	40.32
Open circuit piezoelectric voltage to the beam free-end displacement ratio	β	1.71×10^4 V/m
Clamped capacitance of the piezoelectric element	C_0	140 nF

Table 3.6: Derived experimental parameters

α	2.4×10^{-3} N/V
K_0	1.45×10^3 N/m
M	6.2×10^{-3} kg
D_0	7.5×10^{-4} V/m/s
$k_m^2 Q_m$	1.11

3.4.2 PEG parameters identification and OSECE waveforms

The piezoelectric cantilever structure presents all the features of the linear model defined in chapter 2. The model parameters can be identified using equations 3.43 and the experimental measurements defined in Table 3.5. The obtained parameters are given in Table 3.6.

$$\alpha = \beta C_0 \,, \quad K_0 = \alpha\beta \frac{f_0^2}{f_1^2 - f_0^2} \,, \quad M = \frac{K_0}{4\pi^2 f_0^2} \,, \quad D_0 = \frac{2\pi M f_1}{Q_m} \tag{3.43}$$

Figure 3.14 shows the experimental waveforms in the OSECE circuit as well as the vibration displacement of the PEG. When the displacement reaches a maximum, the switch control signal rises to 10 V, thus the switch S_1 is closed and the switch S_2 is opened instantaneously and electrical charges are extracted (detail waveforms in the figure). The next extraction phase occurs when the displacement reaches a minimum, then the switch control signal drops to -10 V, the switch S_2 is closed while the switch S_1 is opened.

3.4.3 Comparison of the experimental harvested powers

Harvested powers in case u_M:

In the first experiment, the cantilever beam is driven to get a constant 1.2 mm displacement amplitude of its free-end. A 162 nF capacitor is connected in parallel with the piezoelectric element, in this case, the value of $k_m^2 Q_m$ is 0.52. The experimental measure-

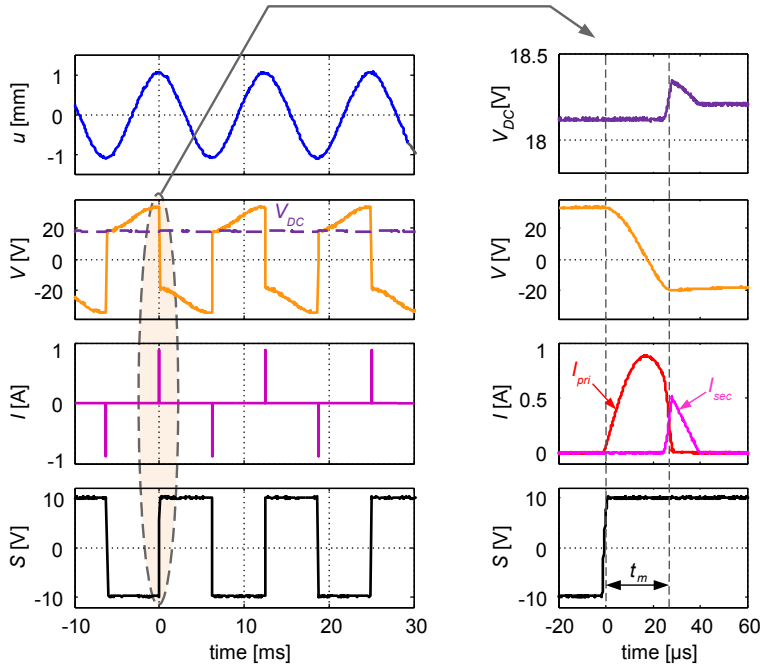

Figure 3.14: OSECE experimental waveforms: vibration displacement (u), piezoelectric voltage (V), DC voltage across the load circuit (V_{DC}), currents in the transformer (I) and switch control signal (S)

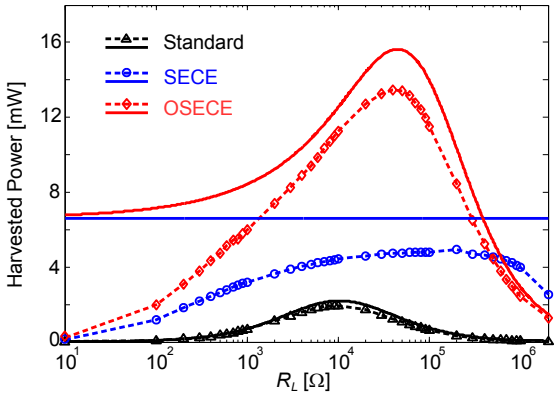

Figure 3.15: Harvested powers as a function of the load resistance

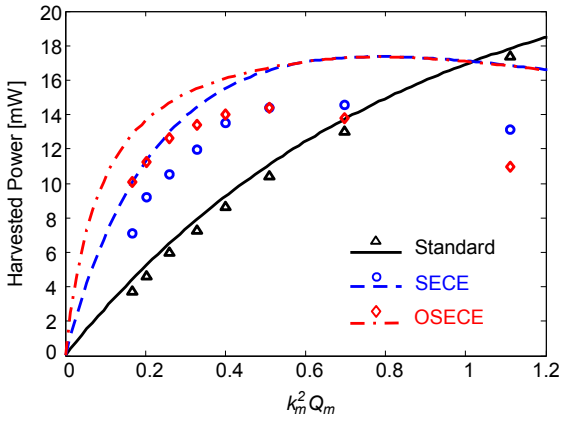

Figure 3.16: Harvested powers as a function of electromechanical structure's figure of merit

ments of the electrical quality factor Q_I and turns ratio m are 5.5 and 0.94 respectively. Finally, experimental harvested powers and theoretical predictions are plotted in Figure 3.15 as a function of the load resistance R_L.

For the standard circuit, the impedance matching issue is clearly shown, and the maximal harvested power is 2 mW. Using the SECE circuit allows to increase the harvested power (5 mW) and to make it more independent from the load. The maximal power harvested by the OSECE circuit is 13.5 mW on a 40 kΩ optimal load. Even if the harvested power using OSECE is more dependent on the load than in the SECE case, it is almost always higher, except for resistance larger than 500 kΩ.

Harvested powers in case F_M:

In the second experiment, the beam is driven at its resonance frequency, and the external exciting force amplitude is kept constant at 118 mN. In order to change the electromechanical structure's figure of merit, various capacitors are chosen to be connected in parallel with the piezoelectric element.

Theoretical calculations and experimental results are depicted in Figure 3.16. As expected, OSECE technique allows harvesting more energy for low value of $k_m^2 Q_m$, thus require less piezoelectric material for the same amount of power, saving both space and cost. From another point of view, if the PEG is a weakly coupled electromechanical structure (for instance the figure of merit is lower than 0.52), using OSECE circuit leads to the highest power.

As depicted in case u_M, the harvested power using the standard EEC strongly depends on the load. Moreover, this optimal load resistance is a function of the vibration frequency and the figure of merit $k_m^2 Q_m$. The matching impedance strategy is then inappropriate to wideband vibrations. For this reason, a load adaptation interface is usually required in addition to the standard circuit, which would also induce additional losses that are not taken into account in this study.

Table 3.7: Parameters of the diodes and the secondary winding of the transformer

Name	Description	Value
V_{fwd}	Forward threshold voltage	0.5 V
V_{rev}	Reverse breakdown voltage	200 V
R_{on}	Resistance in forward conduction	0.4 Ω
R_{off}	Resistance when off	20 MΩ
R_{ser}	Equivalent series resistance	1.23 Ω

In addition, when the value of $k_m^2 Q_m$ is larger, the use of SECE or OSECE circuit induces a strong damping effect, leading to a reduction of the harvested power. In can be noticed that in this case, the OSECE power is slightly lower than for the SECE, whereas theoretical results converge. This is due to the fact that the optimal range of resistance in the OSECE approach is slightly shifted to the lower value when $k_m^2 Q_m$ raises, involving more losses increase due to nonlinear losses in the interface circuit. That will be discussed in the following section.

3.5 Electrical losses evaluation in nonlinear EECs

Comparing the experimental results with the theoretical predictions, it is worthy of note that there exists some energy losses in SECE and OSECE EECs, especially for low load resistance in case u_M (Figure 3.15), and these losses are not taken into account in the theoretical model.

The losses are mainly due to the threshold voltage of the diode and the equivalent resistance in the secondary winding of the transformer, as these nonlinear behaviors cannot be simply taken into account in the previously proposed analytic developments, SPICE (Simulation Program with Integrated Circuit Emphasis) simulations have been performed to give a detailed insight into nonlinear losses. According to the datasheets, four parameters of the diode model and the equivalent series resistance of the secondary wind are defined in the SPICE software and given in Table 3.7.

Results are obtained under the condition of case u_M, Figure 3.17(a) shows the various powers as a function of R_L in the SECE circuit. Both experimental and simulated harvested powers are in very good agreement. The extracted power is the power that is directly extracted from the piezoelectric element. Because some energy losses exist in the circuit, the final harvested power is lower. From the figure, it is clearly shown that there mainly exists the following four sources of energy losses:

- The quality factor of the primary circuit (the only one taken into account in the previously proposed analytical calculation).
- The full-bridge rectifier.

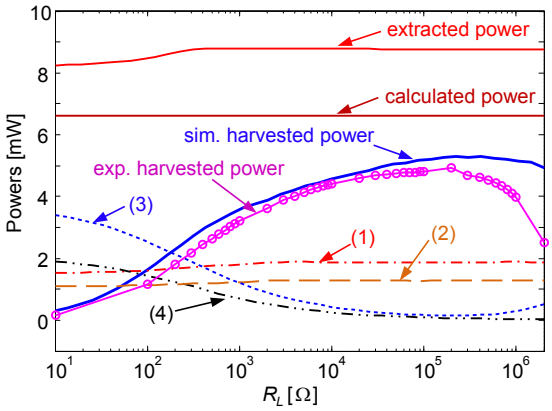

(a) SECE circuit: (1) power lost due to Q_I, (2) power lost due to the full-bridge rectifier, (3) power lost due to the series resistance in the secondary winding, (4) power due to the secondary diode

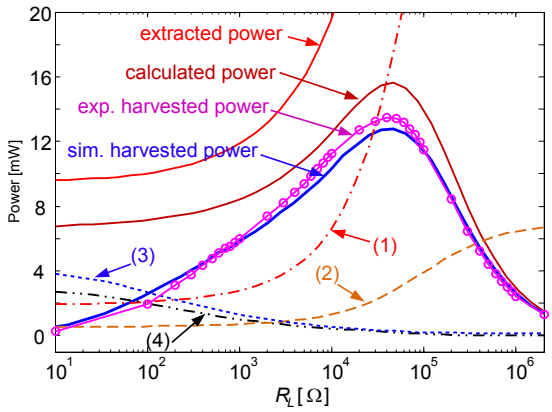

(b) OSECE circuit: (1) power lost due to Q_I, (2) power lost due to the primary diodes, (3) power lost due to the series resistance in the secondary winding, (4) power due to the secondary diode

Figure 3.17: Electrical losses for the two EECs

- The series resistance in the secondary winding.
- The secondary diode.

The first two are constant whatever the load resistance is, they can be optimized by choosing better transformer and full-bridge rectifier. The two last are very high for low load resistances, however they can be minimized when the value of the load resistance is in a specific range (roughly between 10 kΩ and 500 kΩ).

Figure 3.17(b) shows the various powers as a function of R_L in the OSECE circuit. Both experimental and simulated harvested power are also in a very good agreement. There also exists four sources of energy losses in this circuit:

- The quality factor of the primary circuit (taken into account in the previously proposed analytical calculation).

- The primary diodes.
- The series resistance in the secondary winding.
- The secondary diode.

For small resistance values, energy losses are mainly located on the secondary side of the transformer (aforesaid third and fourth sources). For large value of the load resistance, the extracted energy become very large, but a great part is lost due to the quality factor Q_I and in a lower extend in the primary diode.

3.6 Conclusion

This chapter proposes a new energy extraction technique named OSECE for PEG. It is a drastic enhancement from the previous SECE approach. In comparison with the original technique, the OSECE technique has four advantages:

- The switch control strategy is much simpler.
- The circuit is simpler (only one ground signal is necessary in this VEHD system).
- The voltage drop is lower because there is one single diode between the piezoelectric element and the primary inductor.
- The harvested power is enhanced.

Therefore, it can be inferred that the interface circuit can be easily self-powered with regard to the first two advantages. Additionally, because of the last two advantages, the harvested power is also enhanced, as shown by consistent experimental and theoretical results.

From another point of view, because its principle consists in extracting energy when it appears to be maximum in the piezoelectric element, OSECE EEC is expected to be effective whatever the vibration spectrum and especially relevant in the case of wideband vibrations.

4

Two self-powered OSECE circuits: electronic and mechanical approaches

Contents

4.1 Introduction

In the previous chapter, the SECE and OSECE nonlinear energy extraction techniques are presented and compared with the standard energy extraction technique. Both the theoretical and experimental results exhibit the better performances of the nonlinear extraction techniques: the energy density of the PEG is enhanced; the harvested power is load-independent or at least load-weakly-dependent. Nevertheless, the nonlinear energy extraction techniques require synchronized switches, which need to be correctly controlled in the circuits. These switch control signals and related energies are produced by the external dSPACE solution in the previous experimental implementations.

VEHDs are supposed to be stand-alone systems that should operate autonomously. Then, it is mandatory to achieve a totally autonomous EEC for which the synchronized switches are driven and powered by the VEHD itself. But for the SECE EEC, the switch closing time ($10^0 \sim 10^2$ µs) needs to be precisely controlled, so this technique is hard to be achieved in a simple stand-alone system. For the OSECE EEC, the switch control strategy is much simpler: the switch states only need to be reversed at the vibration extrema of the PEG. The OSECE circuit can then be more easily self-powered.

The synchronized switches in the OSECE EECs can be realized using the electronic switches. In this case, derived from the self-powered synchronized switch damping on inductor (SSDI) circuit used to suppress vibrations [115], we propose a similar PKD circuit dedicated to the OSECE circuit. The two identical PKD circuits in the EEC can detect the vibration displacement extreme and supply power to drive the switches synchronously. This approach does not require any additional piezoelectric elements to generate the switch control signal. However, it introduces a phase lag in the control signal and an extra energy consumption to power the PKDs, which reduces the harvested power compared to the ideal case. These effects are particularly studied in this chapter.

Since the required switch closing duration is not critical in the OSECE approach, mechanical switches can also be used to replace the electronic switches. This kind of switches are usually passively controlled by the vibration itself, avoiding the complex switch control strategies especially in the case of wideband random vibrations [121]. We propose two identical synchronized mechanical switches dedicated to the OSECE circuit, the switches are composed of the two mechanical stoppers and the moving part of the PEG. As a result, the added stoppers introduce a piecewise-linear stiffness in the mechanical oscillating system. This nonlinear stiffness significantly increases the operating bandwidth of the PEG, as analyzed in chapter 2.

In this chapter, the operating principle of the above two self-powered approaches for the OSECE EEC are presented and experimentally realized: an electronic self-powered OSECE EEC as well as a mechanical one. Advantages and drawbacks of these two approaches are also compared and discussed.

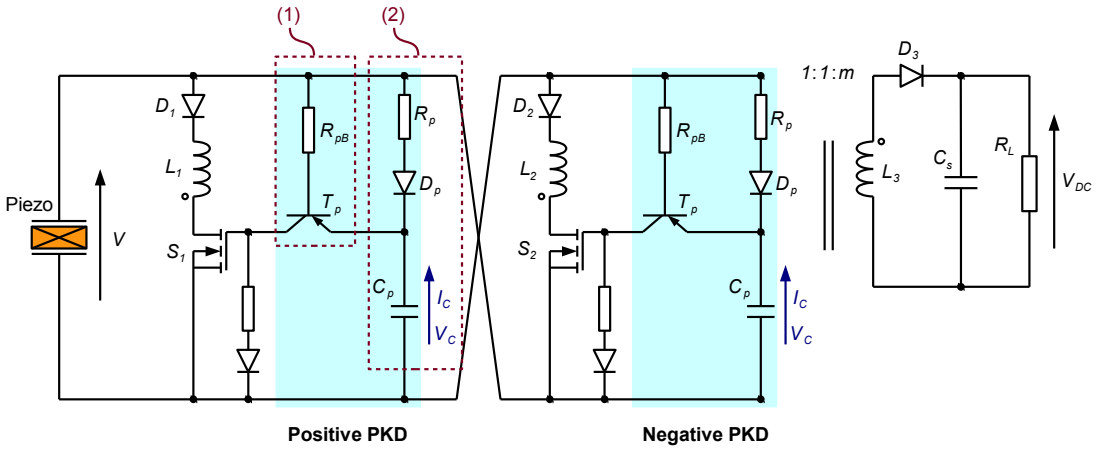

Figure 4.1: Self-powered OSECE circuit: (1) comparator circuit (2) envelope detector

4.2 Electronic self-powered OSECE circuit

4.2.1 Operating principle

According to the principle of the OSECE technique, the switches S_1 and S_2 are driven to reverse the piezoelectric voltage at the displacement extrema. The electronic switches require power and control signal to be correctly driven. In the proposed circuit, the switches are driven by two identical PKD circuits, whose inputs share the common piezoelectric element that is used for energy harvesting, as shown in Figure 4.1. Two N-channel MOSFETs are selected for S_1 and S_2. Their low on-state voltage drops do not drastically hinder the quality factor Q_I of the circuit. In addition, MOSFETs are voltage controlled, that require a smaller storage capacitor C_p. This characteristic reduces the energy consumption of the PKD.

The schematic of the self-powered OSECE circuit is shown in Figure 4.1. Two identical PKD circuits are used, save for the reversed polarities of the piezoelectric voltage between the positive and the negative PKDs. Each PKD consists of a simple comparator (1) and an envelope detector (2).

A traditional envelope detector is an electronic circuit that provides an output V_c which is the envelope of the input alternative signal V [116]. Here, for the positive PKD, the electric energy stored in the capacitor C_p is used to maintain the MOSFET S_1 in the steady-on condition . Moreover, the input impedance of the comparator is far lower than those of a traditional operational amplifier comparators. Consequently, the value of V_c will decrease instead of enveloping the input signal when S_1 is closed. However, this characteristic is especially suitable for the OSECE technique.

Figure 4.2 presents the typical waveforms in the self-powered OSECE circuit. The switch control signal S_1 (S_2) is the output of the positive (negative) PKD. The MOSFET

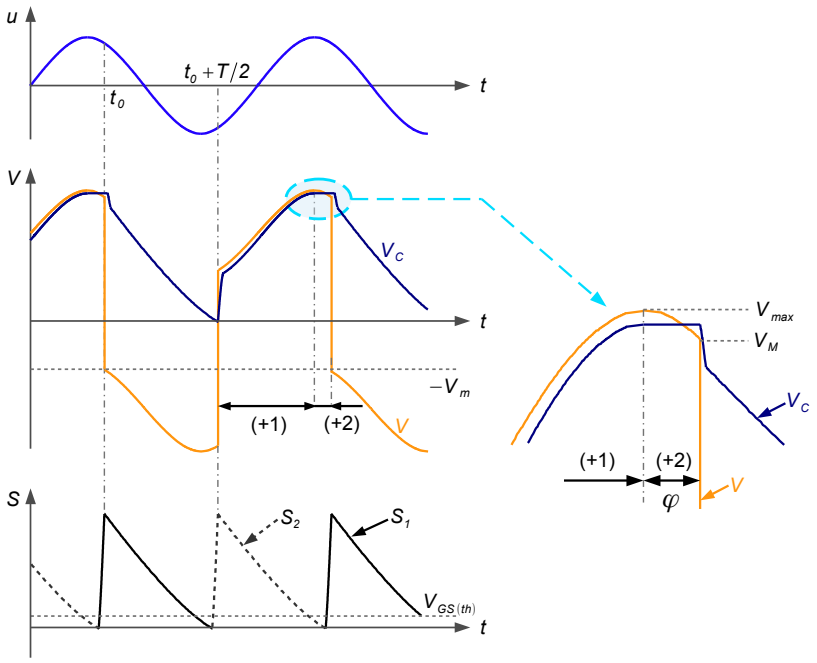

Figure 4.2: Self-powered OSECE waveforms of structure displacement (u), piezoelectric voltage (V), voltage across the capacitor C_p (V_C), and switch control signal (S)

switches will be driven to close as soon as their control signal value is larger than the gate-source threshold voltage $V_{GS(th)}$. In this subsection, V_{max} is the extreme piezoelectric voltage value, V_M and V_m are the values just before and just after the energy extraction phase. It is worthy of note that using this type of PKDs induces a systematic phase lag between the peak voltage and the actual switching time [118]. This is mainly due to the threshold voltages of the diode D_p and the BJT T_p. The phase lag cannot be ignored, and is noted as φ.

Just before stage '+1' (see Figure 4.2), the electric charge stored in the small storage capacitor C_p should be almost or over discharged, so that the voltage V_c is lower than $V_{GS(th)}$ or even negative, to ensure that the switch cannot stay closed more than half a vibration period. With the modern transistor technology, the minimum of $V_{GS(th)}$ can be as low as 1 V. In this chapter, for the sake of clarity, we assume the value of V_c is 0 at this time.

Stage '+1' starts at the beginning of the positive piezoelectric voltage V, C_p begins to be charged by the piezoelectric element. Because of the diode threshold voltage, V_c is always lower than V, as shown by the zoomed waveforms in Figure 4.2. Under this condition, the BJT T_p is reverse biased. Stage '+1' ends as V reaches its positive maximum V_{max}. Considering that the time constant $\tau \approx R_p C_p$ in the envelope detector is much shorter than the vibration period, V_c also reaches its maximum. However, in a strict sense, the piezoelectric element during stage '+1' cannot be completely considered as in open-circuit condition, the outgoing electric charge of the piezoelectric element can be expressed by

the approximate value C_pV_{max}. This charge flows into the small capacitor C_p of the positive PKD circuit. Integrating equation 2.3 over stage '+1' (shown in equation 4.1) leads to equation 4.2 that gives the relationship between the peak voltage V_{max} and the displacement amplitude u_M. At the end of stage '+1', the voltage V_{max} is slightly lower as it would be if the piezoelectric element was in a true open-circuit condition. The energy stored in the piezoelectric element, given in equation 4.3, is then lower than that in the ideal OSECE case, the lost energy is mainly due to PKD circuits, and is expressed by equation 4.4.

$$C_pV_{max} = \alpha \int_{\frac{3\pi}{2}+\varphi}^{\frac{5\pi}{2}} \dot{u}\,\mathrm{d}(\omega t) - C_0 \int_{\frac{3\pi}{2}+\varphi}^{\frac{5\pi}{2}} \dot{V}\,\mathrm{d}(\omega t) \tag{4.1}$$

$$\left(1 + \frac{C_p}{C_0}\right) V_{max} = V_m + \frac{\alpha u_M}{C_0}\left(1 + \cos\varphi\right) \tag{4.2}$$

$$E_{max} = \frac{1}{2} C_0 V_{max}^2 \tag{4.3}$$

$$E_p = \left(2 + \frac{C_p}{C_0}\right) \frac{1}{2} C_p V_{max}^2 \tag{4.4}$$

From another standpoint, the energy consumption in the PKD circuit can also be evaluated by equation 4.4, as the difference between the stored energy in C_0 if the piezoelectric element was in a true open-circuit condition and equation 4.3. Assuming in a reasonable manner that C_p is about 3% of the piezoelectric clamped capacitance, it can be easily calculated that such PKD consumes about 6% of the total electrostatic energy available on the piezoelectric element. This equation then provides a theoretical validation for the conclusion of previous work by Lallart and Guyomar [117].

Stage '+2' occurs as soon as V starts to decrease. At this moment, the diode D_p is no longer in conduction state. However, there are no charging and discharging current paths for the capacitor C_p, V_c will then be kept constant. During this stage, the piezoelectric element is totally open-circuited, the outgoing current I is null, integrating equation 2.3 over the time leads to equation 4.6.

Stage '+2' ends when V decrease to V_M, the difference $(V_c - V_M)$ is then larger than the threshold voltage of the BJT T_p, which starts conducting. The difference $(V_{max} - V_M)$* matches the total threshold voltages of the transistor D_p and T_p. According to equation 4.6, the theoretical expression of the phase lag φ can then be expressed as in equation 4.7.

$$\alpha \int_{\frac{5\pi}{2}}^{\frac{5\pi}{2}+\varphi} \dot{u}\,\mathrm{d}(\omega t) - C_0 \int_{\frac{5\pi}{2}}^{\frac{5\pi}{2}+\varphi} \dot{V}\,\mathrm{d}(\omega t) = 0 \tag{4.5}$$

*$(V_{max} - V_M)$ can be estimated according to the datasheets of the diode D_p and the transistor T_p, typically 1.2 V

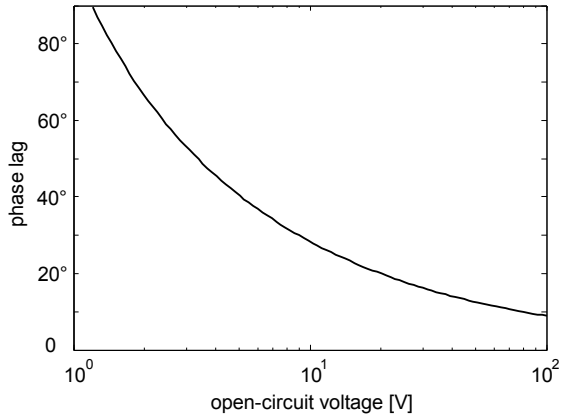

Figure 4.3: Switching phase lag as a function of the piezoelectric open-circuit voltage

$$V_{max} = V_M + \frac{\alpha u_M}{C_0}\left(1 - \cos\varphi\right) \tag{4.6}$$

$$\varphi = \arccos\left(1 - \frac{\left(V_{max} - V_M\right) C_0}{\alpha u_M}\right) \tag{4.7}$$

Figure 4.3 shows the relationship between the switching phase lag and the piezoelectric open-circuit voltage $(\alpha u_M)/C_0$. In this figure, the voltage difference $(V_{max} - V_M)$ is set at 1.2 V. The lower the open-circuit voltage, the larger the phase lag. When the open-circuit voltage is lower than 10 V, the phase lag can be decreased by increasing the voltage; when the open-circuit voltage is larger than 100 V, the phase lag converges to about 10°.

It is worthy of note that the phase lag in this electronic self-powered approach cannot be neglected in any case, even by maximizing the piezoelectric open-circuit voltage. In practical application, the output voltage of the piezoelectric element exhibits high frequency noise, whose magnitude will increase proportionally to the piezoelectric voltage. If the noise amplitude is larger than $(V_{max} - V_M)$, the PKD will become over sensitive. In this case, the value of the resistor R_p must be increased for filtering purpose to make sure the phase lag is bounded in an appropriate range. Equation 4.7 is then not valid in this particular case. However, from the authors experience, the noise amplitude for most PEGs remains low, in this thesis, we consider that equation 4.7 is accurate enough.

As soon as the BJT T_p starts conducting, the gate voltage of the switch S_1 will immediately equal the output voltage of the envelope detector V_c. S_1 will be closed whenever V_c is higher than $V_{GS(th)}$. At this moment, the electric charges accumulated on the piezoelectric element start to be extracted under the principle of the OSECE approach. Considering the energy lost due to the quality factor Q_I of the $r_I L_1 C_0$ oscillating circuit, the harvested energy, transferred to the $\{C_s\ R_L\}$ load, equals the energy stored in the inductor L_1 just after the energy extraction phase. From the work in chapter 3, the harvested energy can be expressed by equation 4.8, and the DC voltage across the load resistor is given by equation

4.9.

$$E_L = \frac{1}{2} C_0 V_M^2 \sin^2(\omega_I t_m)\, e^{-\frac{\omega_I t_m}{Q_I}} = \frac{V_{DC}^2}{R_L}\frac{\pi}{\omega} \tag{4.8}$$

$$V_{DC} = mV_m = -mV_M \cos(\omega_I t_m)\, e^{-\frac{\omega_I t_m}{2Q_I}} \tag{4.9}$$

After the energy extraction phase, the piezoelectric voltage is reversed. The base voltage of T_p is much lower than its emitter voltage. Since the input impedance of the BJT is low, the remaining charges stored in C_p will be discharged to the positive pole of the piezoelectric element through the base emitter junction of T_p. V_c decreases, and the energy stored in this capacitor is dissipated in the resistor R_{pB}.

The minimal piezoelectric voltages are detected using the negative PKD circuit, and energy is extracted in a similar way.

Electronic self-powered OSECE circuit in case u_M:

In the self-powered OSECE circuit, the theoretical expression of the energy extraction phase is the same as that in the ideal OSECE approach. However, taking into account the switching phase lag and the energy lost in the PKD circuits, the harvested power in this case is finally given by equation 4.10.

$$\begin{cases} P_u^{self} = \frac{2\alpha^2\omega}{\pi C_0} \frac{\sin^2(\omega_I t_m) e^{-\frac{\omega_I t_m}{Q_I}}}{\left[1+\frac{C_p}{C_0}+\cos(\omega_I t_m) e^{-\frac{\omega_I t_m}{2Q_I}}\right]^2} u_M^2 \left[2\cos\varphi + \frac{C_p}{C_0}(\cos\varphi - 1)\right]^2 \\ \omega_I t_m = \arctan\left(-m\sqrt{\frac{2\pi}{R_L C_0 \omega}}\right) + \pi \end{cases} \tag{4.10}$$

Electronic self-powered OSECE circuit in case F_M:

During half a vibration period defined between t_0 and $t_0 + T/2$, considering the electromechanical system's energy balance, the external mechanical energy provided to the system is distributed into the mechanical loss, the lost energy due to the PKDs and the energy extracted when the primary side is connected. Equation 4.11 is then obtained from the energy balance. The displacement amplitude u_M can then be expressed as a function of the external force amplitude F_M, and the harvested power can be calculated using equation 4.10 eventually. An analytical expression can be obtained though it will not be given here for conciseness.

$$\int_{t_0}^{t_0+T/2} F\dot{u}\,\mathrm{d}t = D\int_{t_0}^{t_0+T/2} \dot{u}^2\,\mathrm{d}t + E_p + \frac{1}{2}C_0(V_M^2 - V_m^2) \tag{4.11}$$

Table 4.1: Dimensionless parameters

Parameter	Expression	Definition
ξ_R	$\frac{2R_L C_0 \omega}{\pi}$	Load resistance coefficient
$k_m^2 Q_m$	$\frac{\alpha^2}{C_0 D_0 \omega}$	Figure of merit of the electromechanical structure
Q_I	$\frac{1}{r_I}\sqrt{\frac{L_1}{C_0}}$	Quality factor of the $r_I L_1 C_0$ oscillating circuit
ε_{v1}	$\frac{(V_{max}-V_M)C_0}{\alpha u_M}$	Voltages ratio in case u_M
ε_{v2}	$\frac{(V_{max}-V_M)\alpha}{k_m^2 Q_m F_M}$	Voltages ratio in case F_M
ε_c	$\frac{C_p}{C_0}$	Capacitances ratio

Table 4.2: Normalized harvested powers in case u_M

EECs	Case u_M
Ideal OSECE	$\bar{P}_u^{OSECE} = 4\frac{\sin^2(\omega_I t_m)\mathrm{e}^{-\frac{\omega_I t_m}{Q_I}}}{\left[1+\cos(\omega_I t_m)\mathrm{e}^{-\frac{\omega_I t_m}{2Q_I}}\right]^2}$
self. OSECE	$\bar{P}_u^{self} = (2-2\varepsilon_{v1}-\varepsilon_{v1}\varepsilon_c)^2\frac{\sin^2(\omega_I t_m)e^{-\frac{\omega_I t_m}{Q_I}}}{\left[1+\varepsilon_c+\cos(\omega_I t_m)e^{-\frac{\omega_I t_m}{2Q_I}}\right]^2}$

4.2.2 Theoretical performance comparison

The aim of this subsection is to compare the theoretical harvested powers for the ideal OSECE EEC and its self-powered EEC in the two excitation cases. In order to make the comparison as generic as possible, several dimensionless parameters are defined in Table 4.1.

Comparison in case u_M:

Using the same procedure as in chapter 3, the harvested powers are normalized with respect to the maximal power using the standard EEC. The results are finally given in table 4.2, where the value of $\omega_I t_m$ is shown in equation 4.12.

$$\omega_I t_m = \arctan\left(-\frac{2m}{\sqrt{\xi_R}}\right) + \pi \tag{4.12}$$

Figure 4.4 shows the curves of the normalized harvested power as a function of the load resistance coefficient ξ_R. ε_{v1} and ε_c are chosen to be 0.1 and 0.03, respectively. These values are chosen to be representative of practical cases. Although the maximal powers still depends on ξ_R in the OSECE approaches, the dependency is much lower than that with the standard EEC (the larger m, the lower the dependency). In addition, the discrepancy

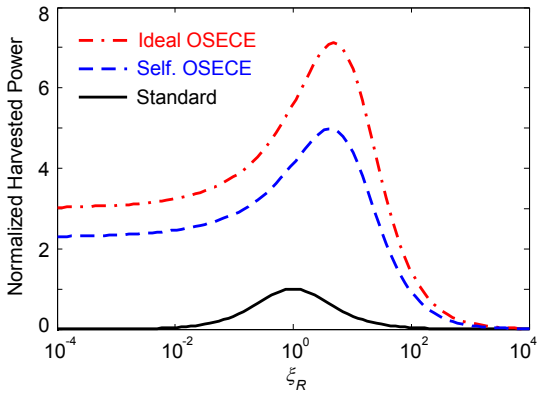

Figure 4.4: Normalized harvested powers in case u_M ($Q_I = 5.5$, $m = 1$)

Table 4.3: Normalized harvested powers in case F_M

EECs	Case F_M
Ideal OSECE	$\bar{P}_u^{OSECE} = \dfrac{\pi k_m^2 Q_m}{\left[\frac{\pi}{4} + \frac{1-\cos(\omega_I t_m)e^{-\frac{\omega_I t_m}{2Q_I}}}{1+\cos(\omega_I t_m)e^{-\frac{\omega_I t_m}{2Q_I}}} k_m^2 Q_m\right]^2} \dfrac{\sin^2(\omega_I t_m)e^{-\frac{\omega_I t_m}{Q_I}}}{\left[1+\cos(\omega_I t_m)e^{-\frac{\omega_I t_m}{2Q_I}}\right]^2}$
self. OSECE	$\bar{P}_u^{self} = \dfrac{\pi k_m^2 Q_m}{\left[\frac{\pi}{4}+X k_m^2 Q_m\right]^2} \dfrac{\sin^2(\omega_I t_m)e^{-\frac{\omega_I t_m}{Q_I}}}{\left[1+\varepsilon_c+\cos(\omega_I t_m)e^{-\frac{\omega_I t_m}{2Q_I}}\right]^2} \dfrac{(2-2\varepsilon_{v2}-\varepsilon_{v2}\varepsilon_c)^2}{4}$

between the self-powered and the ideal OSECE approaches is due to the switching phase lag and the energy losses in the PKDs.

Comparison in case F_M:

Still using the same procedure as in chapter 3, the harvested powers are normalized with respect to the maximal power using the standard EEC. The results are finally given in table 4.3, where an intermediate variable X is defined by equation 4.13.

$$X = \frac{\varepsilon_c\varepsilon_{v2}(4+2\varepsilon_c-2\varepsilon_{v2}-\varepsilon_c\varepsilon_{v2})}{4(1+\varepsilon_c)} + \frac{1+\varepsilon_c-\cos(\omega_I t_m)e^{-\frac{\omega_I t_m}{2Q_I}}}{1+\varepsilon_c+\cos(\omega_I t_m)e^{-\frac{\omega_I t_m}{2Q_I}}} \times \left[1-\varepsilon_{v2}+\frac{\varepsilon_{v2}^2}{2}+\frac{(2+2\varepsilon_c+\varepsilon_c^2)(\varepsilon_{v2}^2-2\varepsilon_{v2})}{4(1+\varepsilon_c)}\right] \tag{4.13}$$

Figure 4.5 shows the maximal normalized powers as a function of $k_m^2 Q_m$ (which means that the value of ξ_R is optimized for both OSECE and standard approaches, respectively). The normalized harvested powers are always lower or equal to 1, which is in accordance with the limit power given in chapter 3. The limit power cannot be obtained using nonlinear OSECE EECs because of the energy loss due to the quality factor Q_I of the oscillating

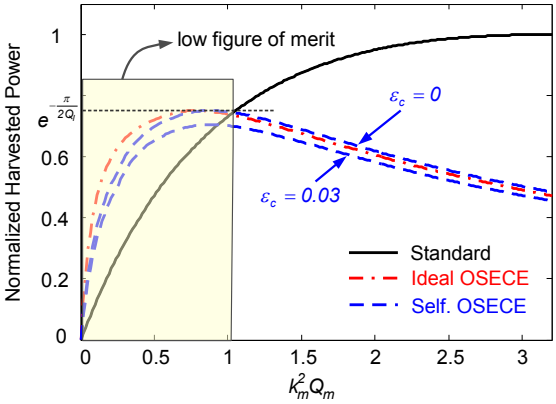

Figure 4.5: Normalized harvested powers in case F_M ($Q_I = 5.5$)

circuit as well as the energy consumption in the PKD circuits. However, as many PEGs exhibit figures of merit lower than 1 [47], the interest of the OSECE approaches is clearly demonstrated: an harvested power equals to the one obtained using the standard approach can be reached, but for much lower value of $k_m^2 Q_m$.

It is worthy of note that the phase lag in this case does not reduce the maximal harvested power, as shown by the curve corresponding to $\varepsilon_c = 0$ ($\varepsilon_c = 0$ amounts to assume that the PKDs energy consumption is null). On the contrary, the energy lost in the PKDs reduces the maximal harvested power from 0.752 to 0.706 as the capacitance ratio ε_c increases from 0 to 0.03. This appears to be a key parameter for the self-powered OSECE circuit optimization.

4.2.3 Experimental validation and discussion

Figure 4.6 show the experimental setup for the electronic self-powered OSECE approach. The PEG and the programmable resistance box are the same as that presented in chapter 3. The waveforms of the piezoelectric voltage, the positive switch control signal and voltage across the small storage capacitor in the self-powered OSECE circuit are all shown by an oscilloscope (DSO1014A Oscilloscope, Agilent Technologies©). The voltage V_{DC} is acquired by the dSPACE solution to calculate the harvested power and is also shown by a handheld digital multimeter (Agilent Technologies©).

Switching phase lag:

The theoretical as well as experimental values of the switching phase lag φ as a function of the vibration amplitude u_M are shown in Figure 4.7. Here, u_M is proportional to the piezoelectric open-circuit voltage. Both the theoretical (plain line) and experimental (dots) phase lags are in good agreement, they can be optimized by increasing the vibration amplitude in a given PEG. Nevertheless, from the experimental result, phase lag lower than 30° is shown to be hardly achievable in this validation system.

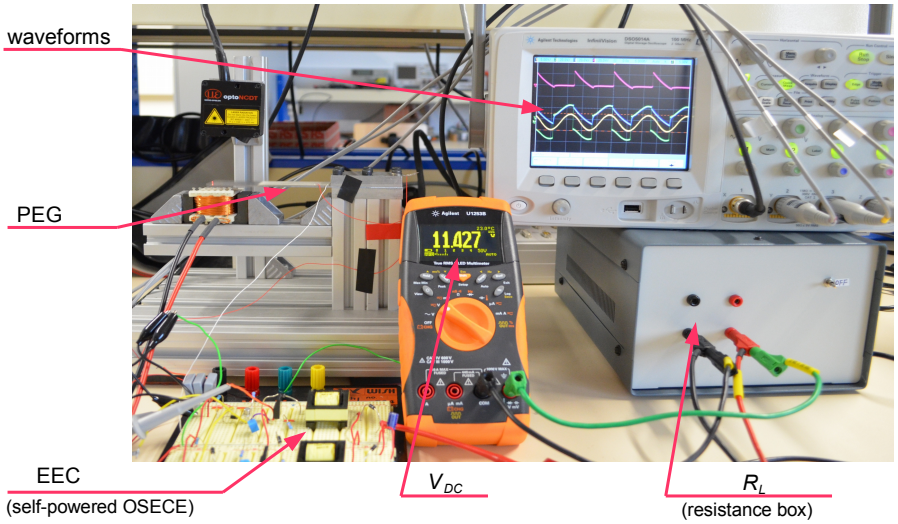

Figure 4.6: Experimental setup for electronic self-powered OSECE approach

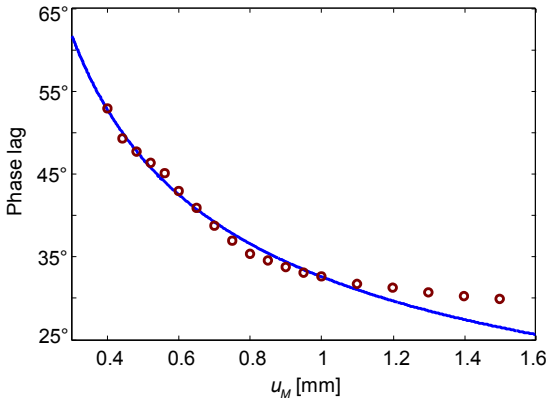

Figure 4.7: Phase lag as a function of vibration amplitude

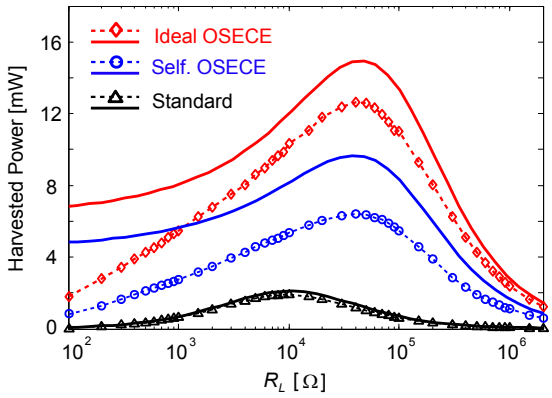

Figure 4.8: Harvested powers as a function of load resistance

Harvested powers in case u_M:

The beam is driven so as to get a constant 1.2 mm displacement amplitude. A 168 nF capacitor is connected in parallel with the piezoelectric element, in this case the figure of merit $k_m^2 Q_m$ of the PEG is 0.44. Experimental measurements of the electrical quality factor Q_I and turns ratio m are 5.5 and 0.95, respectively. The values are slightly different from the former values given in chapter 3*.

Harvested powers are plotted in Figure 4.8 as a function of the load resistance R_L, where the plain lines are the theoretical predictions, the lines with dots are the experimental measurements. Comparing the experimental curves with the theoretical predictions, some energy losses are still not taken into account in the OSECE models, especially for low load resistances. They are mainly due to the diodes threshold voltage and the equivalent resistance in the secondary winding of the transformer. A detailed analysis of these losses has been proposed in chapter 3 for the ideal OSECE EEC.

For the standard circuit, the impedance matching issue is clearly underlined, and the maximal harvested power amounts to 1.9 mW. Using the OSECE techniques, the harvested powers stay dependent on the load while being always higher than 1.9 mW for almost the whole range of load resistance, which confirms the potential of the proposed approach. The difference of the harvested powers between the self-powered and ideal OSECE EECs is mainly due to the switching phase lag and the energy consumption in the PKDs. However, the energy balance between the extracted energy and the energy consumed by the PKDs appears to be always positive.

Power consumption of PKD circuits:

Figure 4.9(a) shows the simulated power extracted from the PEG, the harvested power and the power consumption of the PKDs. Simulations were carried out using the SPICE

*We think that the main reason is because the two pieces of the heavy circular steel mass were removed from the PEG frame.

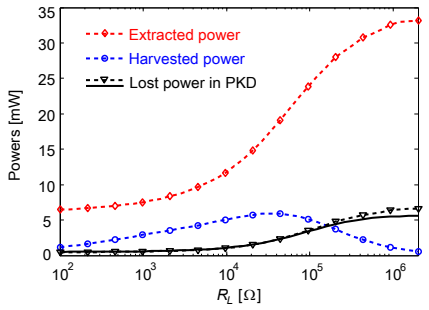

(a) extracted power, harvested power and PKD power consumption

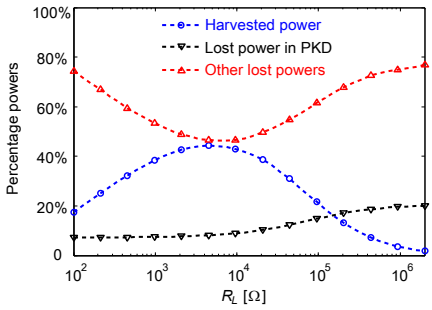

(b) harvested power and PKD power consumption as a percentage of the extracted power

Figure 4.9: Simulation powers as a function of the load resistance

software. The simulated harvested power is very similar to the experimental results shown in Figure 4.8, which confirm the reliability of the simulations. In Figure 4.9(a), the simulated power consumption of the PKD circuits is also compared to the theoretical power consumption calculated from equation 4.4 (plain line). This confirms that equation 4.4 is a good evaluation of the energy consumption of the PKD circuits. To stress out the self-powered additional consumption, Figure 4.9(b) presents the harvested power, the PKDs supplied power and the power lost in the OSECE circuit itself (except for the PKD circuits), as percentages of the extracted power. Using a load resistance lower than 100 kΩ, the PKD circuits consumption ratio adds up to less than 20%. In addition, a maximum of 45% of the extracted energy is actually harvested in this experiment. In fact, the difference between the extracted and the harvested powers is mainly due to the power lost in the OSECE circuit itself, as detailed in the last part of chapter 3.

Harvested powers in case F_M:

In this experiment, the beam is driven at its resonance frequency, and the external exciting force amplitude is constant and equal to 152 mN. In order to vary the figure of merit of the PEG, various capacitors are chosen and connected in parallel with the piezoelectric element.

Theoretical calculations and experimental results are depicted in Figure 4.10. The load resistance is optimized for each figure of merit. The differences between theoretical and experimental results are once more due to the other nonlinear behaviors in the OSECE EECs. As expected, OSECE techniques allows harvesting more energy for low value of $k_m^2 Q_m$, thus requiring less piezoelectric material (k_m is roughly proportional to the amount of piezoelectric material) for the same amount of power and/or allow to enhance the bandwidth reducing the value of Q_m.

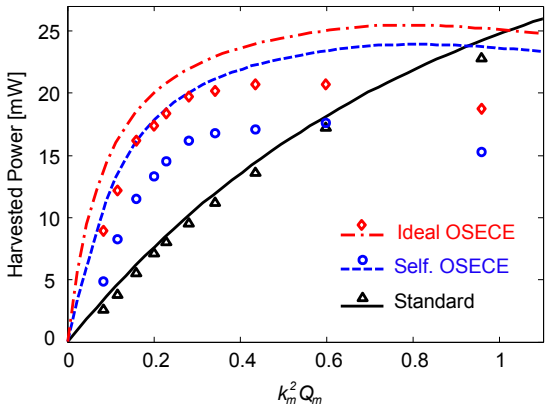

Figure 4.10: Harvested powers as a function of electromechanical structure's figure of merit

4.2.4 Optimization of the self-powered approach

In order to optimize the effectiveness of the self-powered circuit, based on the above analysis, some key electronic parameters are point out in this subsection, see Table 4.4. Recommendations for optimization are listed in the following:

- To get enough initial energy to drive the MOSFET switch, the electric charge stored in the capacitor C_p should be larger than $N\frac{V_{GS(th)}}{V_{max}}(C_{gs}+C_{gd})$*; considering the disappeared charge in the PKD circuit and the variable piezoelectric maximal voltage V_{max}, a safety margin N ($N = 50$) is selected in this optimization. Still, the value of N cannot be chosen to be too large because larger value of C_p will increase the energy consumption in PKDs.
- Considering the MOSFET, according to Meyer's capaitance model, the total intrinsic gate charge Q_g should be as small as possible. But for a given MOSFET technology, the on-state resistance R_{ON} and Q_g are opposite to each other, R_{ON} will reduce the quality factor Q_I of the oscillating circuit at the same time, so it is more relevant to choose a MOSFET with a small value of figure of merit**.
- The phase lag is proportional to the total threshold voltage in the PKD circuit, so the diode and BJT should exhibit the lowest threshold voltages as possible.
- The resistor R_p should be as small as possible because it is a dissipative element. From our exprience, piezoelectric voltage usually exhibits a spike noise just after the energy extraction phase, so it is better to keep the time constant τ larger than t_m.
- The value of the resistor R_{pB} affects the discharging speed of C_p. It should be as large as possible to minimize the power consumption but small enough to let C_p be fully discharged in half a period of the vibration.

*C_{gs} and C_{gd} are the MOSFET gate-source and gate-drain lumped capacitances, respectively.
**figure of merit equals to $R_{ON} \times Q_g$

Table 4.4: Optimized value of the electronic elements

Name	Optimized value	Selected value
C_p	Larger than $N\frac{V_{GS(th)}}{V_{max}}(C_{gs}+C_{gd})$	4.7 nF
MOSFET	Small figure of merit	6.6×10^{-11} ΩC
D_p	Low threshold voltage	0.65 V (for 100 mA)
T_p	Low threshold voltage	1.3 V (max)
R_p	As small as possible and $\tau \geqslant t_m$	$2\sim16.5$ kΩ
R_{pB}	$500\sim1000$ kΩ	776 kΩ

Anyway, apart from the electronic optimization, electromechanical structure also has to be considered as an important part. An advanced PEG with high force-voltage coefficient and large clamped capacitance will also improve the efficiency of the self-powered circuit.

4.3 Mechanical self-powered OSECE circuit

Traditionally, the electronic switches in the electronic circuits are driven by a voltage or current signal, and their states are definite. Nevertheless, the voltage drop due to BJTs or the on-resistance of MOSFETs induces electrical losses during the energy extraction process, especially in the case of low piezoelectric voltage. This appears to be critical in the case of MEMS PEG (e.g. the piezoelectric output voltage is very low). Moreover, if the PEG is excited by random vibrations, it may become difficult to generate the control signal from the piezoelectric signal itself, while the switches need to be driven synchronously and properly.

For this reasons, the use of mechanically driven synchronous switches dedicated to the OSECE EEC is proposed hereafter. The switches consist in stoppers and the moving part of the oscillator which is passively driven by the vibration itself, avoiding complex switching control strategies.

4.3.1 Operating principle

Figure 4.11 shows a mechanical self-powered OSECE circuit as well as a piecewise-linear PEG presented in chapter 2. Most of the time, the piezoelectric element in the cantilever beam is in open-circuit condition, so the piezoelectric voltage is proportional to the vibration displacement. When the tip of the beam hits one of the stoppers, the vibration displacement reaches the bounded stroke (maximum or minimum), so do the piezoelectric voltage. Since the metal beam and the metal stoppers compose the mechanical switches in the OSECE EEC, the corresponding synchronous switch in the circuit is then closed. The electric charges accumulated on the piezoelectric element are transferred to the primary

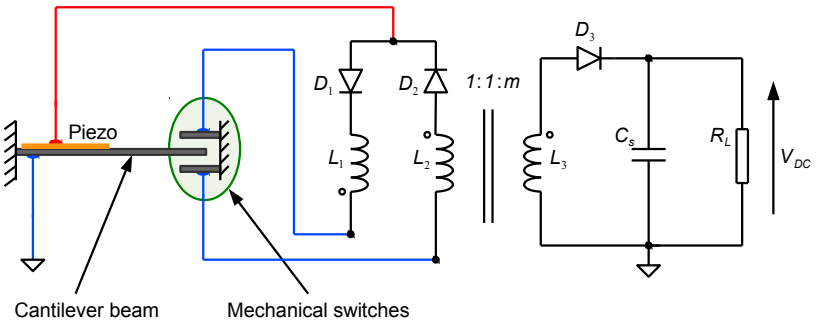

Figure 4.11: Mechanical self-powered OSECE circuit

inductor L_1 (or L_2), leads to the energy extraction phase of the OSECE approach as presented in the former chapter. After this phase, even the stopper and the beam are still engaged, the diode in series with the closed switch is reversed biased. The extracted energy stored in the magnetic field of the transformer is then transferred to the $\{C_s\ R_L\}$ load circuit. In addition, the symmetrical mechanical stoppers here limit the vibration amplitude of the PEG, this kind of VEHDs amounts to harvest energy in case u_M which is proposed in chapter 3, the constant vibration amplitude u_M roughly equals the limited distance d.

Figure 4.12 shows the operating stages of the mechanical self-powered OSECE circuit. Stage '+' ('-') stands for that the piezoelectric element is in open-circuit condition and its voltage is positive (negative). Stage '1' corresponds to the energy extraction and charging phases occurs in the OSECE approach. The two phases are very short compared to the vibration period.

As soon as stage '2' occurs, the voltage V_{pri} across the inductor L_1 will drop to 0 (See stage '-' in Figure 3.8). Consequently, although the vibration displacement still increases (the piezoelectric voltage recovers) a little bit, and the stopper and the beam are engaged, the diode D_1 is deeply reversed, the piezoelectric element is kept in open-circuit condition. However, from the waveform of the piezoelectric voltage, it is clearly shown that, due to the stage '2', the mechanical self-powered approach introduces a switching phase advance in the OSECE technique. It has the same effect as the switching phase lag in the electronic self-powered approach. The value of the phase advance corresponds to half of the engaging duration. Assuming that the vibration displacement of the PEG remains sinusoidal, the phase advance is then expressed by equation 4.14.

$$\varphi = \arcsin\left(\frac{d}{u_M}\right) - \frac{\pi}{2} \tag{4.14}$$

It is worthy of note that this phase advance can be neglected if the stiffness of the stopper is hard enough, because the real vibration amplitude u_M is more close to the limited distance d. In addition, we think this kind of mechanical switches are particularly

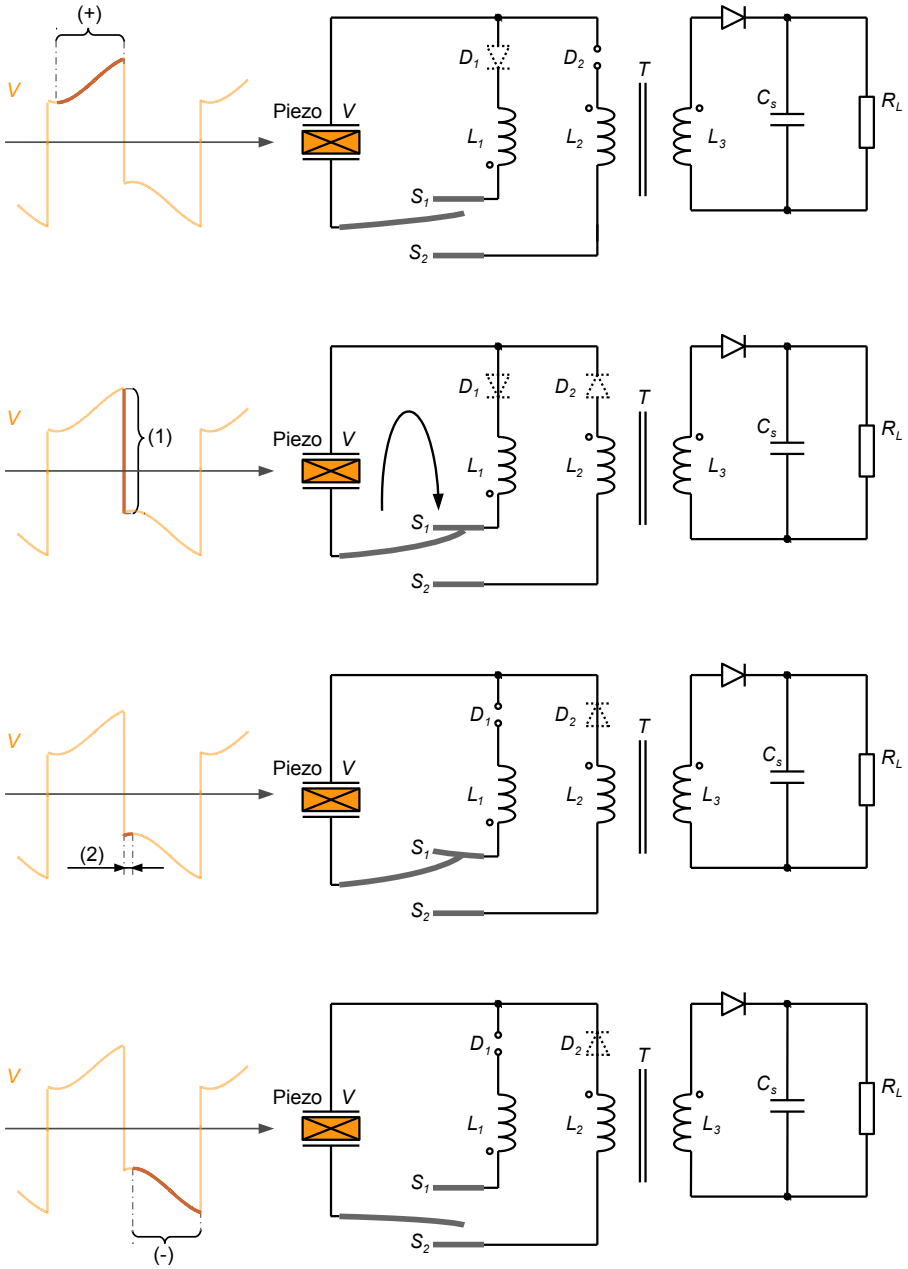

Figure 4.12: Energy extraction principle of the mechanical self-powered OSECE circuit,, stage (+): piezoelectric element is in open-circuit condition and its voltage is positive; stage (1): energy extraction and charging phases; stage (2): piezoelectric element is in open-circuit condition and the beam and the stopper are engaged; stage (-): piezoelectric element is in open-circuit condition and its voltage is negative

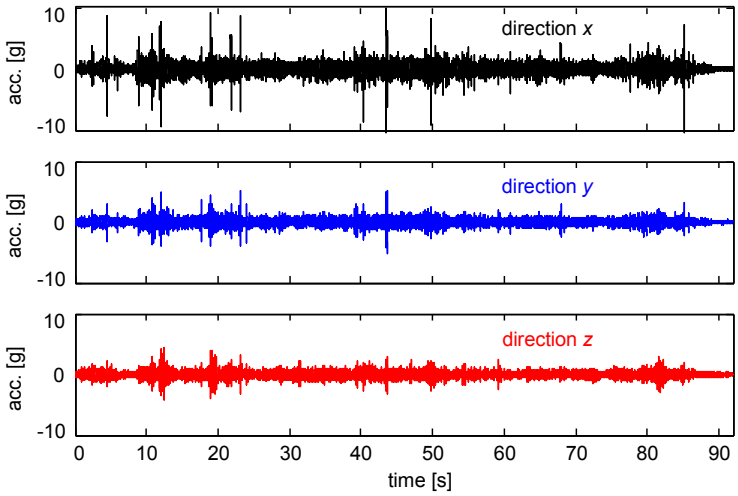

Figure 4.13: Time history of a real vibration of the car in three directions

suitable for random vibrations. The value of the phase advance is then insignificant to be calculated if the vibration displacement of the PEG is not the sinusoidal signal. Anyway, we should keep on mind that this switching phase advance in the mechanical self-powered EEC reduces the extraction effectiveness compared to the ideal OSECE EEC.

4.3.2 Simulation of the performance for random vibrations

The aim of this subsection is to verify the feasibility of the mechanical self-powered OSECE EEC in random vibrations. Some simulated random signals such as exponentially correlated noises, periodic forces and Gaussian white noises are usually used in the laboratory experimental environment [135]. These signals are good approximations of real-world vibrations in some cases. However, in this subsection, a real environment vibration is selected to test the performance of the presented self-powered approach.

Fortunately, a lot of real vibration data is kindly made available by the NiPS laboratory* [135]. For each vibration signal, it is possible to download the time series data, structured in a tab delimited text file with four column (time and acceleration for each axis). Figure 4.13 shows a typical vibration in a car (Renault Clio, Renault©), where the accelerometer is fixed near a wheel, and the direction x is set along the gravity. In addition, the signal is measured under the condition of the urban roads. From the figure, the acceleration values in the directions y and z are very close, the RMS values of them are 0.43g and 0.42g, respectively. The acceleration in the direction x is larger (0.77g), especially the peak values.

Figure 4.14 gives the power spectrum of the selected vibration. It is related to the correlation function through the Fourier transform, which reveals the repetitive and correlated patterns of the vibration signal. According to this figure, it is clearly shown that the

*http://realvibrations.nipslab.org/

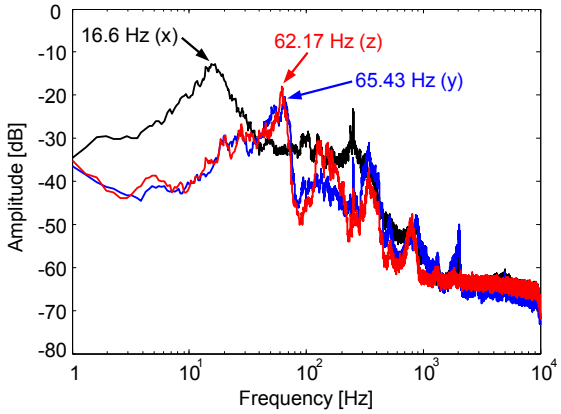

Figure 4.14: Power spectrum of the vibration in three directions

measured vibration energy is roughly distributed over a [10 Hz, 100 Hz] frequency band. Anyway, the vibration signal in each direction still has a main peak spectral density, which is noted in the figure.

Because the vibration in direction x has a larger RMS value, it is selected to excite the piecewise-linear PEG. In order to fit for the excitation, the first resonance frequency of the cantilever beam is set as 16 Hz, and the limited distance is 3 mm. Hence, the vibration displacement of the PEG can easily reach its limitation and hit the stoppers, the corresponding mechanical switches are passively closed. Moreover, in the OSECE circuit, a 47 µF capacitor C_s is used to store the voltage V_{DC}, and the equivalent load resistance is set as 20 kΩ.

The simulated waveforms of the mechanical self-powered OSECE approach are shown in Figure 4.15. Due to the mechanical stoppers, the maximal vibration amplitude of the PEG is limited at 3 mm. As soon as the beam impacts one of the stoppers, the electric charges accumulated on the piezoelectric element are immediately extracted to the $\{C_s\ R_L\}$ load circuit using the OSECE approach. The voltage V_{DC} across the capacitor C_s jumps to a higher value, leads to store the more harvested energy in the capacitor. However, there exists some moments where the beam can not hit the stoppers, see the small circles in the detailed waveforms (local extremes). In these moments, the OSECE EEC cannot extract any electric charge. In the $\{C_s\ R_L\}$ load circuit, since the value of the resistance R_L is not large, V_{DC} keeps on decreasing due to the time constant. That is the reason the voltage V_{DC} varies as a function of the time in the figure.

Finally, the simulated result shows that the mechanical self-powered OSECE circuit totally harvest 93 mJ electrical energy in one minute, which means the average harvested power of the VEHD is 1.55 mW.

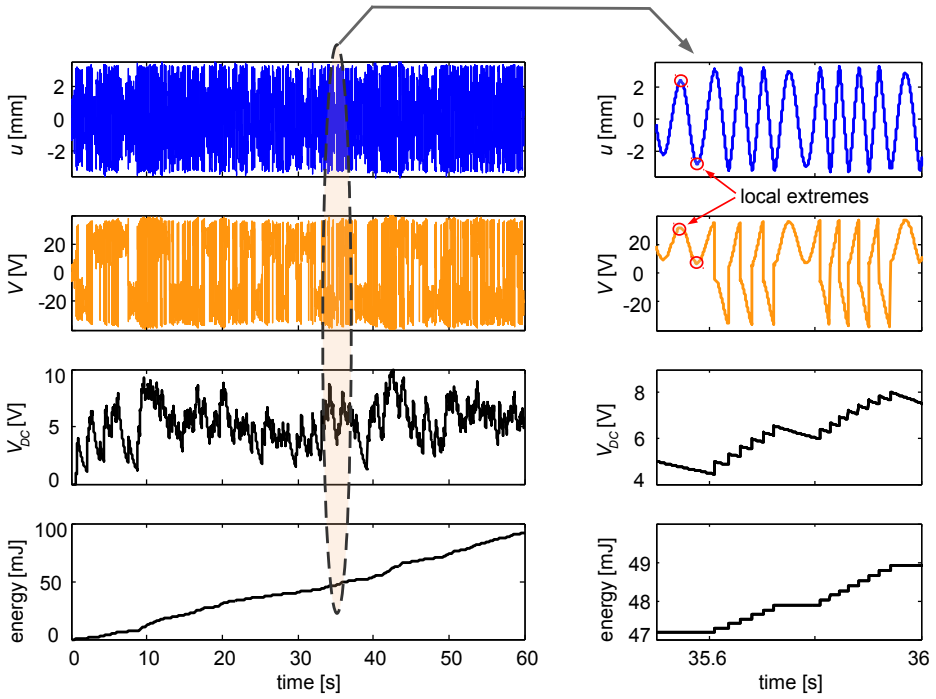

Figure 4.15: Simulation waveforms of the mechanical self-powered OSECE EEC: vibration displacement (u), piezoelectric voltage (V), DC voltage across the load circuit (V_{DC}) and the accumulated harvested energy of the EEC

4.4 Experimental comparison and discussion

Three kinds of autonomous VEHDs are compared in this section: linear PEG plus standard EEC, linear PEG plus electronic self-powered OSECE EEC, as well as piecewise-linear PEG plus mechanical self-powered OSECE EEC.

As presented in chapter 2, the stoppers induce the stiffness-hardening effect on the original oscillator so that it is capable of increasing the bandwidth for the forward sweep excitations. For the reverse sweep, no benefit is exhibited, but the low-energy orbit can be jumped to the high-energy orbit by changing the initial condition or applying a short and strong impact [136]. In order to simplify the comparison, only the performances for the forward excitation are investigated in this section.

4.4.1 Experimental setup

The schematic of the experimental setup is shown in Figure 4.16(a), and the experimental VEHD prototype is shown in Figure 4.16(b). The piecewise-linear PEG is composed of a steel cantilever beam clamped at one end and two identical stoppers symmetrically fixed on the frame. A piezoelectric layer is bonded on the surface of the beam, close to the clamped edge. The mechanical stoppers are made from plastic screws and copper beams, which can be tuned to adjust the limited distance d. For practical reason, the OSECE

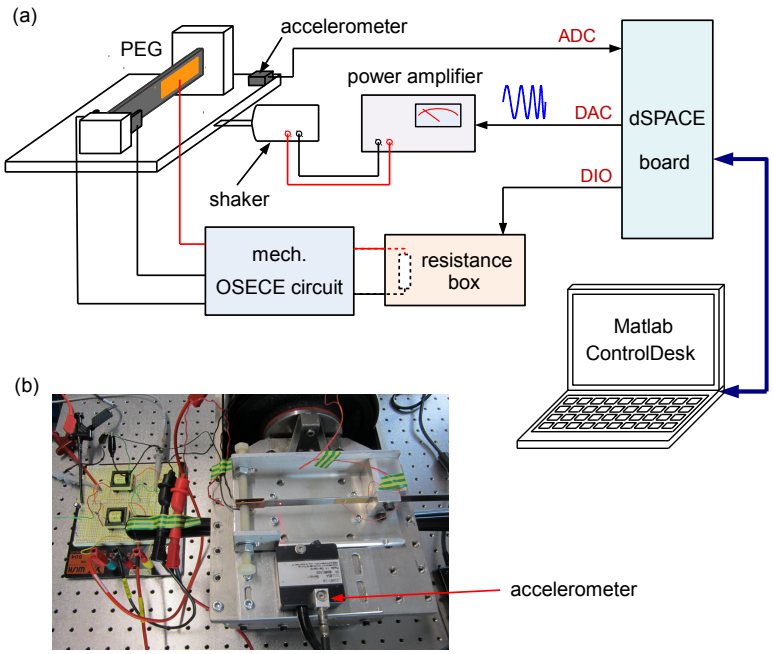

Figure 4.16: Experimental setup: (a) schematic of the experimental setup, (b) VEHD prototype

circuit is implemented using two flyback transformers, each of them having single primary and secondary windings. The behavior is exactly same as the implementation illustrated in the schematic OSECE circuit, provided that both secondary windings are followed by a rectifying diode and connected in parallel. In addition, for the linear PEG, it is composed of the same piezoelectric cantilever beam, only the stoppers are removed from the frame. The resonance frequency of the beam is 87 Hz, and its figure of merit $k_m^2 Q_m$ is 0.44 ($k_m^2 = 0.0067$, $Q_m = 65.85$).

The PEG frame is fixed on a shaker which produces the vibrations in the horizontal direction. The dSPACE solution provides the external acceleration signal, it is a forward sweep signal whose frequency interval is (80 Hz, 100 Hz). An accelerometer allows the acceleration amplitude to be measured and a proportional-integral-derivative (PID) controller is used to adjust the amplitude of the output signal of the dSPACE solution, hence the external exciting acceleration amplitude is automatically kept constant at 1.2g.

4.4.2 Experimental harvested powers and their comparison

Figure 4.17 gives the vibration amplitude frequency response of the cantilever beam under the three different cases. The curves clearly show that for the piecewise-linear PEG, due to the mechanical stoppers, the amplitude around the resonance frequency is limited at the benefit of a wider bandwidth. From the curves of the two linear PEGs, it is shown that using the OSECE technique, the vibration amplitude near the resonance frequency is always lower than that using the standard approach. This is because the OSECE approach

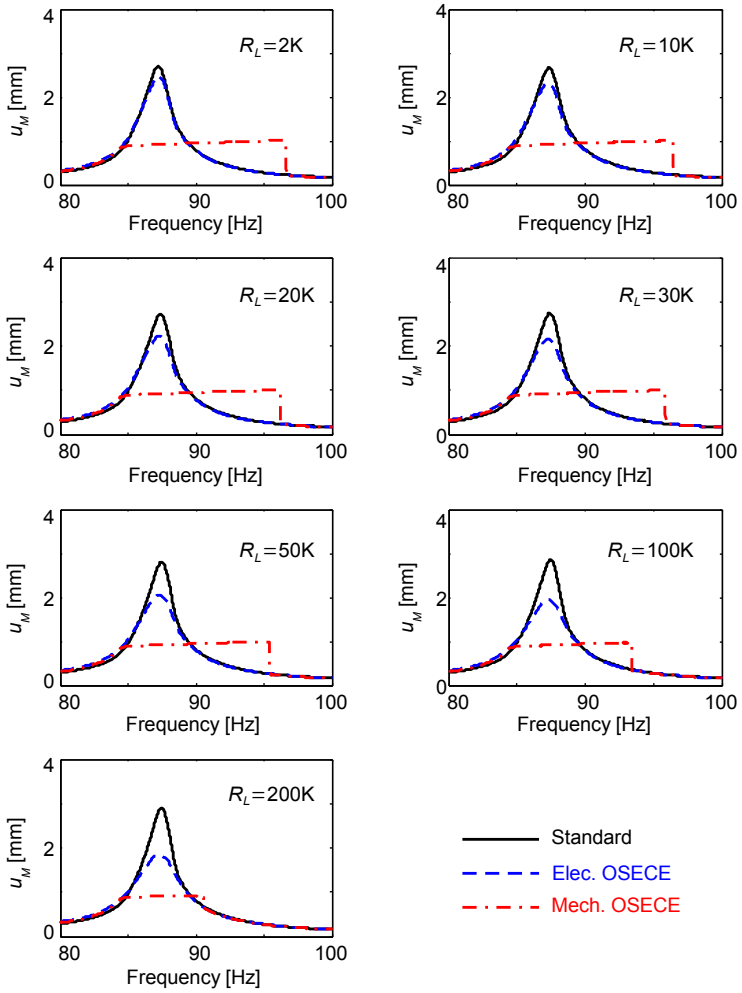

Figure 4.17: The comparison of the vibration amplitudes using different EECs

induces a stronger damping effect that leads to a reduction of the vibration amplitude, especially when the load resistance is large. The damping effect also reduces the operating bandwidth of the piecewise-linear PEG. However, when the load resistance is not so large (lower than 100 kΩ), the piecewise-linear PEG can still significantly increase the operating bandwidth.

Figure 4.18 shows the harvested powers in the cases of the three different EESs as a function of the exciting frequency. Comparing the 7 subfigures, it is clearly shown that the harvested power using the standard EEC strongly depends on the load, while using the OSECE technique, the dependencies are much more weak. Moreover, due to the advanced OSECE technique, the harvested power using the electronic self-powered approach is higher than that using the standard EEC; for the mechanical self-powered approach, even if the vibration amplitude is limited, higher power can be harvested especially when the load resistance is larger than 50 kΩ.

It is worthy of note that, considering a typical practical application of a VEHD, the

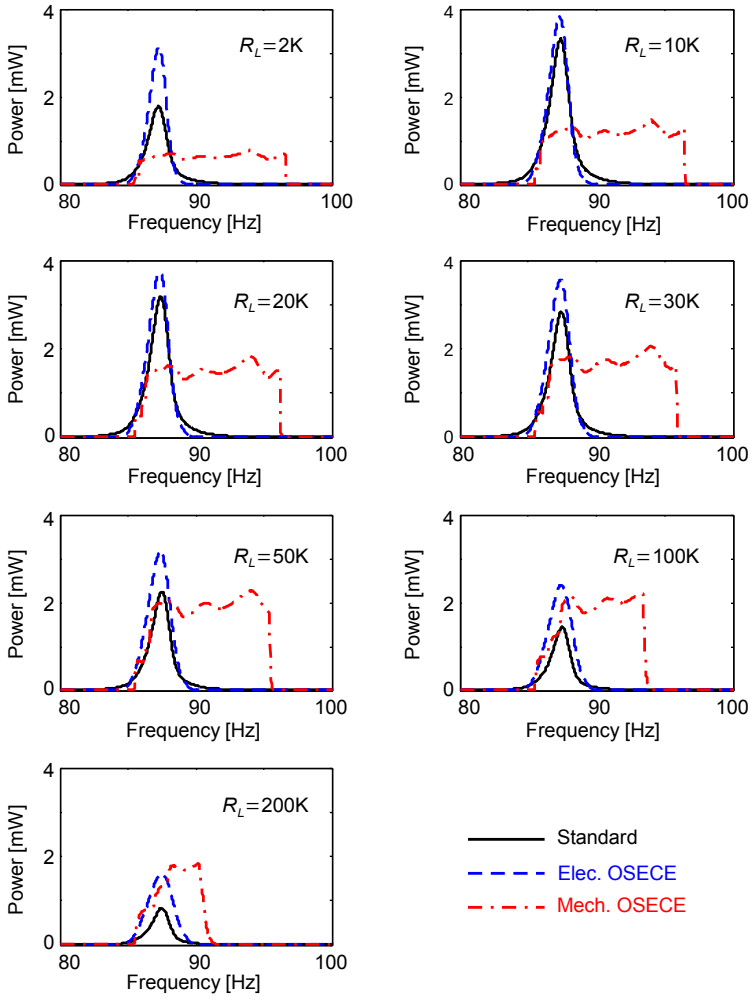

Figure 4.18: The comparison of the harvested powers using different EECs

powered electronic modules would often stay in the ultra-low power condition during significant periods of time. These periods correspond to large load resistance (typically much larger than 50 kΩ), since the current supplied to the load is very low (typically a few μA). Using the mechanical self-powered OSECE EEC in this condition allows to optimize the energy harvesting process and then to maximize the voltage on the storage capacitor C_s. When the supplied electronic module will operate in a high power consumption situation, it will then be able to operate for a longer time.

Finally, Figure 4.19 shows the harvested power using the mechanical self-powered OSECE EEC as a function of the vibration frequency and the load resistance. Due to the characteristic of the piecewise-linear PEG, the operating bandwidth of the VEHD is wide under the forward sweep acceleration signal; due to the load-weakly-dependent characteristic of the OSECE technique, the harvested power is relatively constant with respect to the different load resistances.

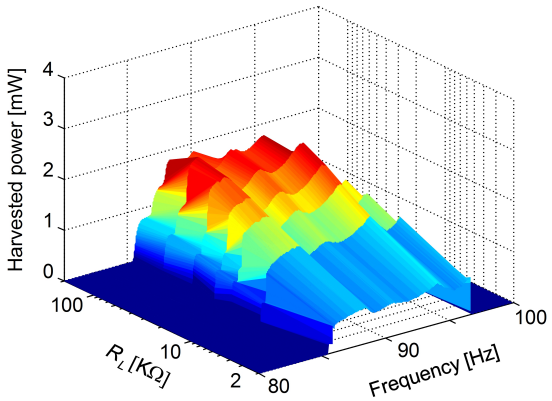

Figure 4.19: The harvested power using mechanical self-powered OSECE EEC

4.5 Conclusion

Two self-powered approaches based on the OSECE technique are proposed in this chapter: an electronic self-powered approach as well as a mechanical one. The different operating principles are theoretical analyzed, the harvested powers are experimentally compared.

Finally, advantages and drawbacks of the two self-powered approaches can be highlighted: compared to the electronic self-powered approach, the mechanical approach simplifies the switching control strategy especially in the case of random vibrations, it also allows to increase the operating bandwidth of the VEHDs; but it decreases the maximal harvested power when the exciting frequencies are close to the electromechanical structure resonances; if the exciting acceleration level is too low, no energy can be harvested at all. Consequently, defining the best approach depends on the practical application.

5

Self-powered wireless sensor nodes: prominent application for vibration energy harvesting technologies

Contents

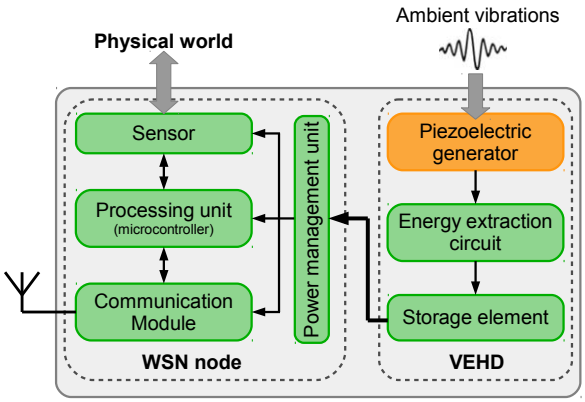

Figure 5.1: The architecture of a self-powered wireless sensor node

5.1 Introduction

The rising number of VEHD prototypes have been proposed in these years, at the same time, several applications have been projected for these VEHDs covering wide range of civilian and defense components [7]. Out of these different applications, the prominent use is to power the nodes in the WSNs.

The WSN nodes collect information about and offers service to the physical environment, increasing requirements support the development of WSNs, structure healthcare monitoring, traffic control, industry measurement, to name a few. Figure 5.1 shows a typical architecture of autonomous WSN node which is powered by the ambient vibration energy. The conventional battery is replaced by a classical piezoelectric based VEHD. Since a potentially perpetual electrical energy can be generated by the PEG, the lifespan of these nodes is no longer limited by the storage energy.

There are three major sources of energy usage in a WSN node:

- Inactive stage, i.e. the node stays in the sleep or idle modes, only waits for some special commands in a very low frequency.
- Normal operation in active stage, i.e. the node samples, stores and possibly processes the data from the sensor.
- Radio communication in active stage, i.e. the node receives or sends data packets in the WSN.

Traditionally, thanks to the modern advanced semiconductor technology, WSN nodes have been designed as ultra low power devices. So in the first two energy consumption sources, WSN nodes usually use very little power, but in the third source, the energy consumption is significantly higher, often larger than the harvested power from environments. Further, the harvested energy typically varies with time in a non-deterministic environment. In the other side, different nodes may have different harvesting opportunity in the same WSN, while there should be at least 2 nodes stay in the active stage together during

Table 5.1: Operating voltage of the ICs

ICs	Operating voltage (V)	
	min	max
BMA222	1.62	3.6
PIC18LF14K50	1.8	3.6
MRF49XA	2.2	3.8

the radio communication phase. Hence, a deliberate smart power management unit in an autonomous WSN node plays an important role between the VEHD and the powered modules.

In this chapter, we focus on designing a demonstration platform of the self-powered wireless sensor node, so we select the simplest WSN, where a typical sensor node only communicate with a coordinator node connected to the computer. This autonomous sensor node consists of a triaxial acceleration sensor (BMA222, Bosch©), a microcontroller (PIC18LF14K50, Microchip©), a radiofrequency (RF) transceiver (MRF49XA, Microchip©) as well as a power management unit. In addition, as a demo application of the energy harvesting technique, the power management unit in the sensor has not been designed to have a complex algorithms to address the issues of the distributed WSN.

5.2 Power management unit

In our self-powered wireless sensor node, an electrolytic capacitor is selected to store the harvested energy because it can support higher storage voltage than that of the normal supercapacitors. Since the harvested power and the consumed power vary with time non-determinately in the system, the storage voltage V_{DC} also varies in a large range. However, the integrated circuit (IC) chips in the node must operate roughly at their nominal supply voltage. Table 5.1 gives the operating voltage of these ICs, which means the output voltage of the power management unit should stay between 2.2 V and 3.6 V.

5.2.1 Voltage regulator and UVLO functions

To obtain a relatively constant supply voltage of the power management unit, voltage regulator is the most important part in the unit. It provides a constant DC voltage, controls power fluctuations and prevents damage to the connected ICs, which means the output voltage of the power management unit remains constant regardless of changes to its input voltage or load conditions [137]. Nevertheless, in the self-powered WSN nodes, if the required power is higher than the harvested power for quite a long time, the input voltage of the power management unit will decrease as the stored energy decreases in the capacitor. As a matter of fact, most of the voltage regulators have the operating limitations about the minimum input voltages. If the input value is close to the minimum value, the

output voltage of the regulator cannot be determined. This phenomenon may lead to a big trouble in the self-powered node, especially when the harvested power roughly equals the consumed power. In this case, a voltage comparator with hysteresis is selected to control the regulator [109]. Using this comparator, the regulator will begin to operate when the input voltage value is sufficiently higher than the minimum limit value, making sure a portion of the stored energy can be efficiently transferred to the output.

There are two types of voltage regulators: linear and switching. A linear regulator employs an active (BJT or MOSFET) pass device (series or shut) controlled by a high gain differential amplifier. It compares the output voltage with a precise reference voltage and adjusts the pass device to maintain a constant output voltage. A switching regulator converts the input voltage to a switched voltage applied to a power MOSFET or BJT switch. The filtered power switch output voltage is fed back to a circuit that controls the power switch on and off times so that the output voltage remains constant regardless of input voltage or load current changes [138]. In our project, in order to get a high efficiency of voltage conversion and simplify the development of the node, a switching type voltage regulator IC is selected to design the power management unit.

There are many IC productions (e.g. LTC3470 and LTC3525 from Linear Technology©, TPS61100 from Texas Instruments©, ADP2503 from Analog Devices©) corresponding to our regulated requirements, however, almost none of them integrates a voltage comparator with hysteresis inside the chip. Additional peripheral electronic components must be selected to realize this function, that induces the complexity of the design and more power losses.

Fortunately, a special IC named LTC3588-1 from Linear Technology© integrates both of these two functions [139]. The voltage comparator with hysteresis function is defined and named as UVLO with hysteresis window in its datasheet [140]. Our power management unit mainly consists of LTC3588-1 IC and its peripheral components. In addition, the energy extraction interfaces can directly connect the input pin of this IC, which provides the harvested energy to input of the power management unit. Consequently, the input impedance of the power manage unit equals the load resistance R_L in the EECs.

5.2.2 Specifications of LTC3588-1

In fact, the LTC3588-1 integrates a low-loss standard EEC inside the chip, which gives a complete piezoelectric energy harvesting solution for self-powered systems. See Figure 5.2, the standard EEC can directly interface with a PEG, rectify an alternative voltage waveform and store energy in an external storage element connected with the VIN pin. However, in order to harvest power more efficiently, the use of the standard EEC may not be the better choice. In our project, we use the OSECE EEC to replace the integrated standard EEC, this part will be discussed in the next subsections.

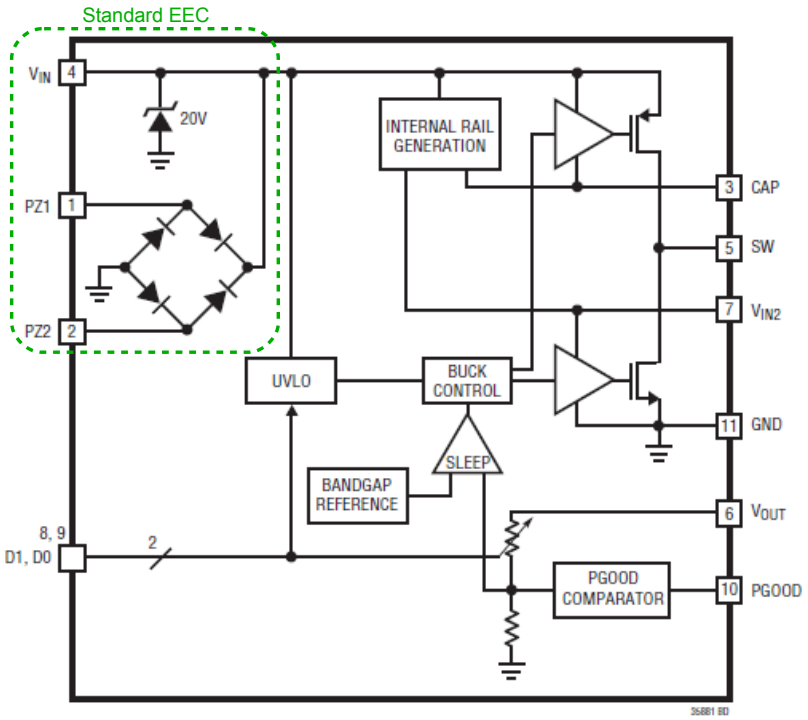

Figure 5.2: Internal block diagram of LTC3588-1 [140]

Some main pin functions of the LTC3588-1 IC are presented in the following [140]:

- **CAP (Pin 3):** Internal rail referenced to VIN to serve as gate drive for buck P-channel MOSFET switch. A 1 µF capacitor should be connected between CAP and VIN pins.
- **VIN (Pin 4):** Input voltage (equals to V_{DC}). This voltage is internally clamped to a maximum of 20 V for the sake of protection. A storage capacitor is usually connected to this pin. The value of the capacitance should be selected according to the practical energy requirements of the application. Moreover, the external EEC can directly connect to this pin, which provides the harvested energy to the storage capacitor.
- **SW (Pin 5):** Switch pin for the buck switching regulator. An inductor should be connected between SW and VOUT pins. In addition, a large value of inductor (e.g. 100 µH) can improve the efficiency of voltage conversion when the input voltage becomes high.
- **VOUT (Pin 6):** Output regulated voltage pin. This voltage is internally sense and adjust through internal feedback. The powered module and a smoothing capacitor are connected with this pin in parallel.
- **VIN2 (Pin 7):** Internal low voltage rail to serve as gate drive for buck N-channel MOSFET switch. Also serves as a logic high rail for output voltage select bits D0 and D1. A 4.7 µF capacitor should be connected from VIN2 to GND.

Table 5.2: Output voltage selection [140]

D1	D0	VOUT
0	0	1.8 V
0	1	2.5 V
1	0	3.3 V
1	1	3.6 V

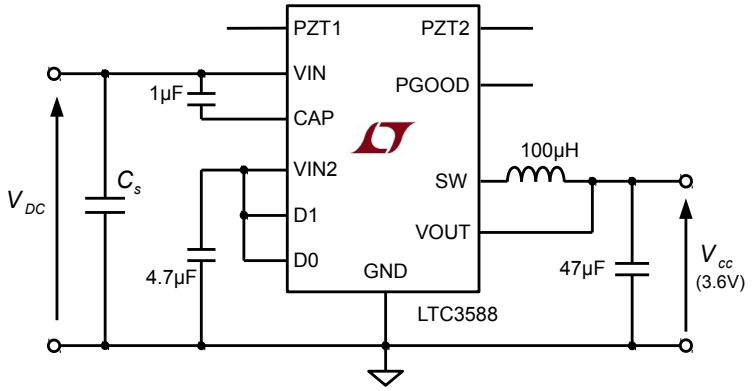

Figure 5.3: Typical schematic circuit of the power management unit

- **D1 & D0 (Pins 8 & 9):** Output voltage select bits. They should be tied high to VIN2 or low to GND to select desired VOUT (See table 5.2).
- **PGOOD (Pin 10):** The pin is logic high when VOUT is about 92% of the target value. The logic high is referenced to the VOUT rail and this signal can be used to enable an inactive micro-processor or other circuitry.
- **GND (Exposed Pad Pin 11):** Ground. The exposed pad should be connected to a continuous ground plane of the printed circuit board by several vias directly under the LTC3588-1 IC.

Figure 5.3 shows a typical schematic circuit of the power management unit based on the LTC3588-1 IC. The capacitor C_s stores the energy obtained from the EEC, whose equivalent load resistance R_L equals to the input impedance of the LTC3588-1. The D0 and D1 pins are tied high to VIN2, which means the output voltage is fixed at 3.6 V. In addition, the peripheral components can be easily selected according to the datasheet.

However, the value of the storage capacitor C_s connected with the VIN pin needs to be specially calculated based on the practical power consumption*. As required, the storage energy should be enough to provide output power for the length of desired time. This may involve using a large capacitor C_s, and/or letting input voltage V_{DC} charge to a high

*Since the output voltage need to be kept constant when the system operates, the capacitor connected with the VOUT pin is only considered a smoothing capacitor in this thesis.

Table 5.3: UVLO thresholds for different outputs [140]

	V_{UVLO1}(V)			V_{UVLO2}(V)		
	min	type	max	min	type	max
1.8V	2.66	2.87	3.08	3.77	4.04	4.30
2.5V	2.66	2.87	3.08	3.77	4.04	4.30
3.3V	3.42	3.67	3.91	4.73	5.05	5.37
3.6V	3.75	4.02	4.28	4.73	5.05	5.37

voltage. So that the IC does not quickly reach the UVLO falling threshold V_{UVLO1} which would halt energy transfer to the output. In general:

$$\begin{cases} P_L t_L = \frac{1}{2}\eta C_s \left(V_{DC}^2 - V_{UVLO1}^2\right) \\ V_{UVLO1} \leqslant V_{DC} \leqslant 20 \end{cases} \tag{5.1}$$

Where η is the average efficiency of the voltage conversion, P_L is the average consumed power, t_L is the desired operating time. This equation can be used to size the storage capacitor C_s to meet the power requirement of the output for the desired duration, assuming that the harvested energy is negligible during this time.

It is worthy of note that in the stand-alone VEHD system, the maximal storage voltage V_{DC} strongly depends on the external excited condition, the figure of merit of the PEG, the EECs, etc.. The value of V_{DC} also affects the harvested efficiency of the system. Hence, the optimal range of V_{DC} is smaller than that given in equation 5.1.

Anyway, if the ambient excitation remains low for a very long time, it is possible that the required energy is larger than the energy stored on C_s during this time, the storage voltage V_{DC} then becomes lower than the UVLO falling threshold V_{UVLO1}, disabling the voltage regulator. In this case, almost all the harvested electric charges are accumulated on the storage capacitor, the voltage V_{DC} rises again. As soon as its value increases above the UVLO rising threshold V_{UVLO2}, the regulator is enabled, making sure at least a portion of the stored energy expressed by equation 5.2 can be transferred to the output, no matter how much the harvested power is. Figure 5.4 gives the schematic diagram of the UVLO function, it clearly gives the relationship between the input and output voltages of the LTC3855-1 IC.

$$E_{tras} = \frac{1}{2} C_s \left(V_{UVLO2}^2 - V_{UVLO1}^2\right) \tag{5.2}$$

For different output voltages, the values of the UVLO thresholds are different. Table 5.3 shows these values, the width of the hysteresis window is about 1.27 V. Assuming, for instance of 3.6 V output voltage, Figure 5.5 shows the simulated waveforms of the input and output voltages, where simulation circuit of the power management unit is shown in Figure 5.3. The SPICE model of the LTC3588-1 IC can be directly downloaded from the

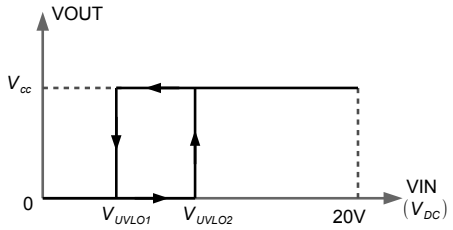

Figure 5.4: UVLO function in LTC3588-1

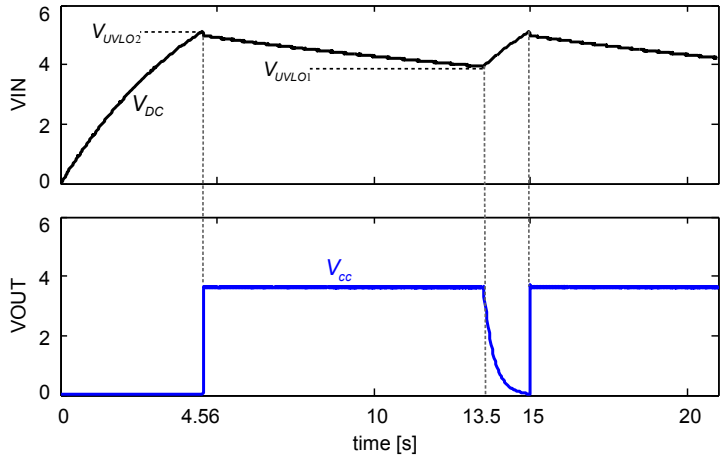

Figure 5.5: Input and output voltage waveforms of LTC3588-1

demo given in the official website*. An equivalent circuit model of the PEG presented in chapter 2 and the standard EEC (full-bridge rectifier) integrated inside the chip are used to charge a 470 µF input capacitor C_s. A 7 kΩ resistor is connected to the output capacitor in parallel.

At the beginning (time lower than 4.56 s), the voltage regulator is disabled, the output voltage is 0, almost all the harvested charges from the VEHD are stored on the capacitor C_s, the storage voltage V_{DC} keeps on increasing until it reaches the V_{UVLO2}.

After 4.56 s, the voltage regulator is enabled, the output voltage is a constant value of 3.6 V, leading to a 1.85 mW output power, which is however higher than the harvested power (1.7 mW). The stored energy decreases.

As soon as the V_{DC} decreases lower to V_{UVLO1} (at time 13.5 s), the regulator is disabled again due to the UVLO function, the output power becomes 0, and the power management unit repeats the first step until the V_{DC} reaches the V_{UVLO2}.

*http://www.linear.com/product/LTC3588-1

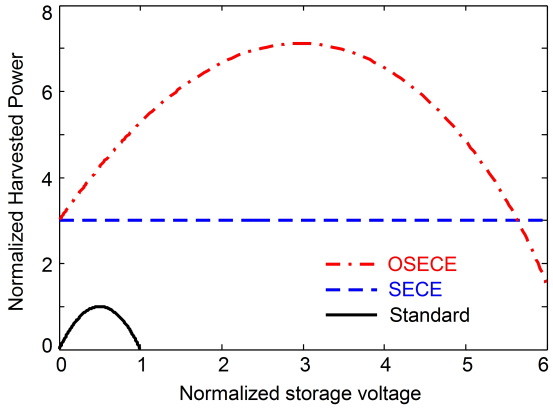

Figure 5.6: Normalized harvested powers of various EECs $Q_I = 5.5$, $m = 1$

5.2.3 Modified application of LTC3588-1

From the previous study of the standard EEC, it is clearly known that the harvested powered is limited and strongly depends on the load resistance under the case of constant vibration amplitude (case u_M proposed in chapter 3). Here, the load resistance corresponds to the input impedance of the power management unit. Since the input impedance is an abstract parameter in the system, according to the theoretical analysis in chapter 3, Figure 5.6 shows the normalized harvested powers as a function of the normalized storage voltage expressed by equation 5.3, where V_{open} is the amplitude of the piezoelectric open-circuit voltage in case u_M.

$$\overline{V}_{DC} = \frac{V_{DC}}{V_{open}} = \frac{C_0 V_{DC}}{\alpha u_M} \tag{5.3}$$

The figure clearly shows that the harvested efficiency of the standard EEC is the minimum one, whatever the storage voltage is. In addition, the maximal storage voltage using the standard EEC cannot be larger than V_{open}, which reduces the potential storage energy if V_{open} is lower than 20 V. From Figure 5.6, it can be seen that using the OSECE EEC, the harvested efficiency is always the maximum one in a wide range of the storage voltage. Moreover, the capacitor C_s can store much more energy since it is proportional to the squared storage voltage.

5.2.4 Experimental validation of the improved power management unit

The experimental setup is composed of a linear PEG, a electronic self-powered OSECE EEC, a power management unit and a simulated load of a typical WSN node, as shown in Figure 5.7(a). The linear PEG is driven to get a constant 1.4 mm displacement amplitude of its free end, and the piezoelectric open-circuit voltage V_{open} is 6.37 V.

The experimental prototype of the power management unit is shown in Figure 5.7(b), electrolytic capacitors are selected to store the harvested energy and smooth the output

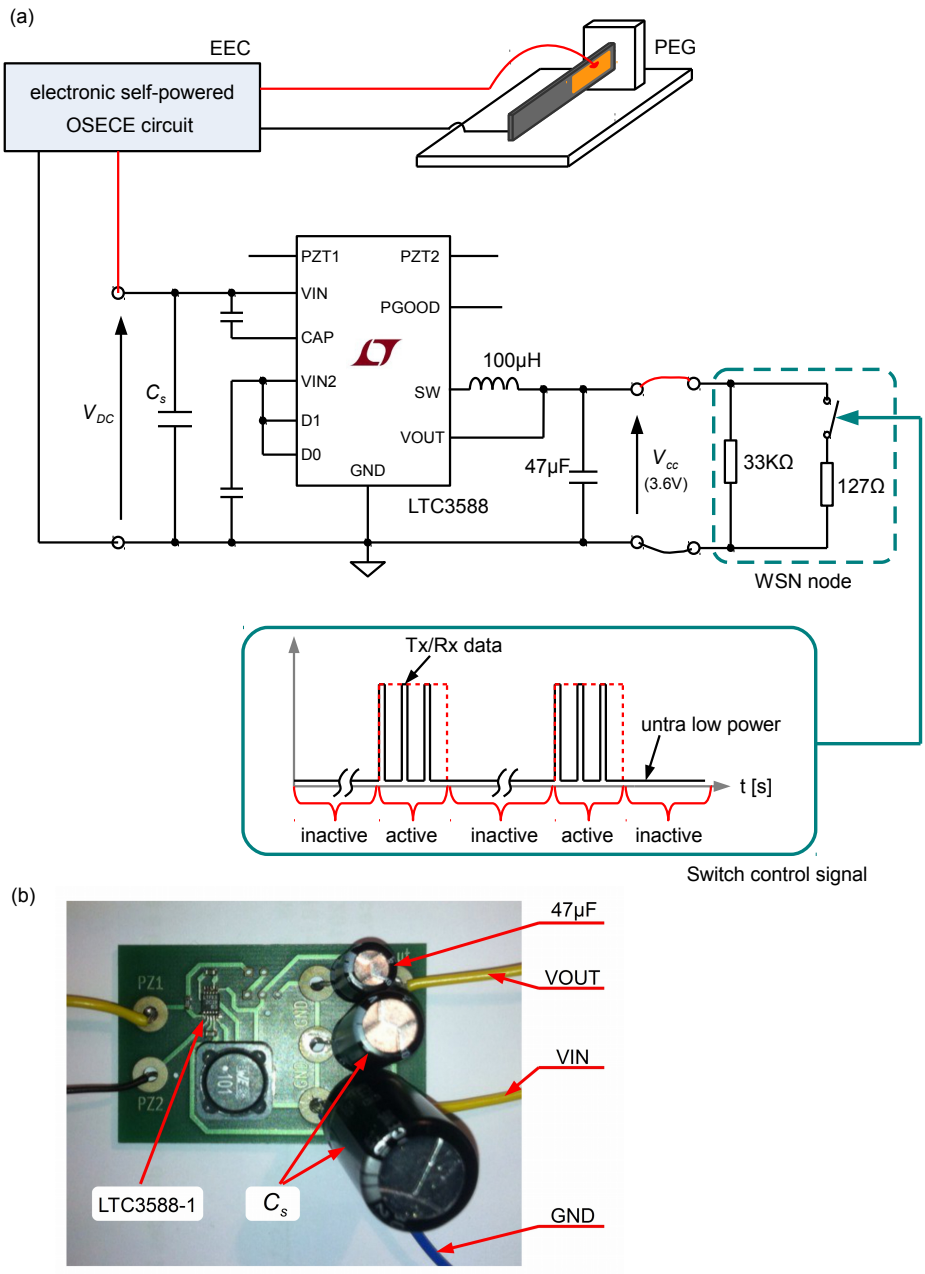

Figure 5.7: Simulated autonomous wireless sensor node: (a) simulated load impedance of a typical sensor node, (b) power management unit prototype

voltage. In order to store more energy, two electrolytic capacitors (1220 μF) are connected in parallel to the VIN pin. The integrated standard EEC can be directly used in the prototype, so that we can compare these results with those using the self-powered OSECE EEC in this experiment.

Because the WSN nodes are powered by DC voltages, their input impedances exhibit linear behaviors, a simple resistors can represent them. In this experiment, two different values of the resistors shown in Figure 5.7(a) simulate a typical wireless sensor node. The large resistor always consumes the energy (when the power management unit has the output voltage), while the small resistor in series with a electronic switch is connected to the output pin periodically. The switch control signal is shown in Figure 5.7(a). In the simulated inactive stage, the switch is in open state, and the "WSN node" stays in low power consumption (0.39 mW); in the simulated active stage, the "WSN node" receives or sends data packets intermittently, which consumes a significant energy, the switch is then closed intermittently to represent this high power consumption (102.44 mW).

Figure 5.8(a) shows the experimental results of the power management unit, where the inactive time of the "WSN node" is 30 s, the active time is 3 s for the standard and the OSECE EECs, respectively. Most of the time, the "WSN node" stays in the inactive stage, when it is enabled, the switch is driven to close every 1 s, and the switch closing time is 0.01 s. At the beginning, both of the storage voltages increase. As soon as they are higher than the UVLO rising threshold, the power management units output the standard DC voltage (3.6 V). However, due to the higher harvesting effectiveness of the OSECE EEC, the increasing rate of its storage voltage is faster, and the LTV3588-1 IC can supply the output much earlier. In addition, the average harvested power using the OSECE EEC is also larger than the average consumed power of the load, the energy stored on the capacitor keeps on increasing all the time.

If the active time is changed to 4 s, of course the average power consumption of the "WSN node" is larger. In this case, the VEHD that uses the standard EEC can not harvest enough energy to provide to the power management unit. Consequently, the voltage regulator inside the unit is disabled intermittently, as shown by the output voltage VOUT in the left side of Figure 5.8(b). During this duration, the "WSN node" can not stay in the operating stage, which limits its performances in some applications. However, form the right side of the figure, it is clearly shown that using the OSECE EEC the power management unit outputs a continuous standard DC voltage, and the stored energy keeps on rising.

Assuming a special application where the minimal active time of the "WSN node" is required to be as long as 30s, it is impossible to select the standard EEC. While using the OSECE EEC under the same conditions, the self-powered system still operates correctly, as shown in Figure 5.8(c).

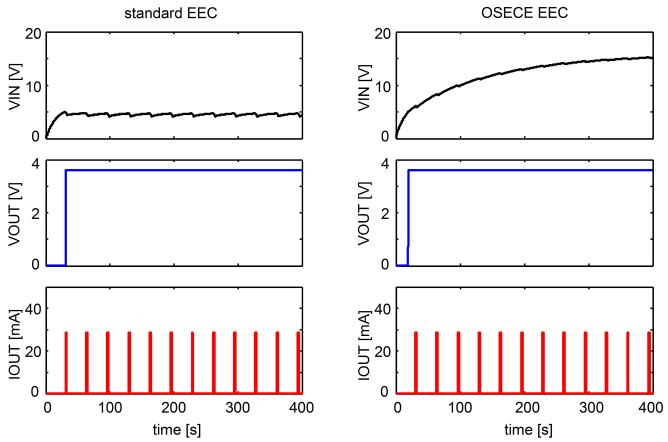

(a) Inactive time 30 s, active time 3 s

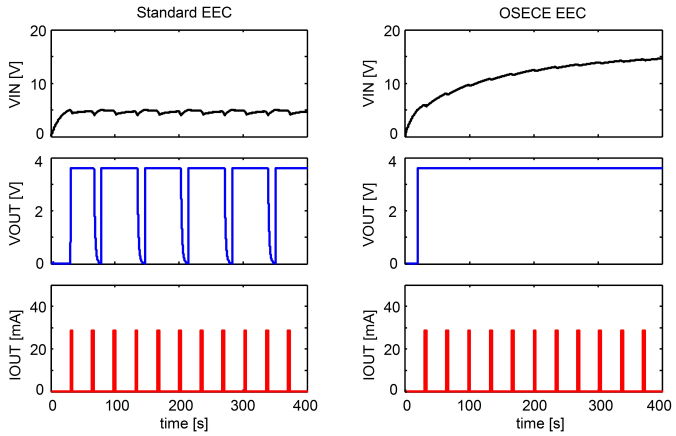

(b) Inactive time 30 s, active time 4 s

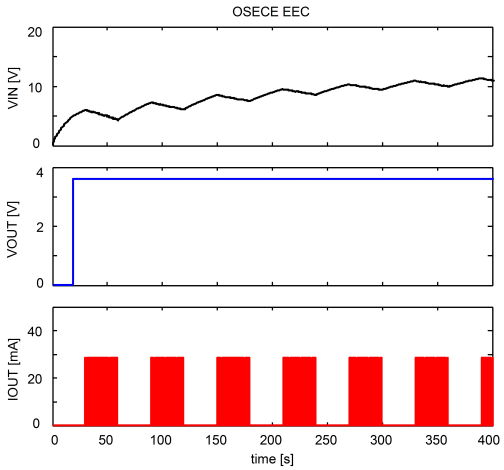

(c) Inactive time 30 s, active time 30 s

Figure 5.8: The time history of the input and output voltages of the power management unit

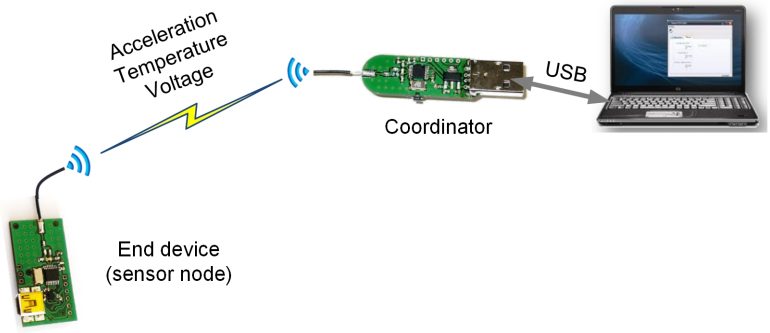

Figure 5.9: Schematic diagram of the star sensor network

5.3 Self-powered sensor node and its demonstration platform

5.3.1 Self-powered demonstration platform

As introduced at the beginning of this chapter, the proposed self-powered WSN developed in the thesis is the simplest star sensor network composed of two nodes: one coordinator node and one end device node*. The end device node directly receives the command from and sends the sensor data to the coordinator node, without any router nodes. For wireless communication, two RF transceiver ICs named MRF49XA are selected in both nodes, work in the unlicensed 868 MHz frequency band.

Figure 5.9 shows the schematic diagram of this network. The coordinator node is connected to the PC using USB port, and also powered by the power line of USB. The sensor node is powered by the autonomous energy harvesting device. After the sensor node receive the command data from the coordinator node, it will parse the data packet firstly, acquire the corresponding sensor data, and send the processed physical data back to the coordinator node. Finally, physical quantities are displayed on the user interface (UI) on the computer.

Figure 5.10 shows the UI of the system, where the user can easily set the information of the measurement in the configuration interface and obtain the physical quantities in the measurement interface. The values of the physical quantities will be refreshed as soon as the coordinator node receives the sensor data, in which the refreshed period equals the measured time plus the inactive duration of the sensor node.

The self-powered sensor node can measure three physical quantities: 3d acceleration, temperature, and supply voltage, according to the commands of the user. Figure 5.11 gives the schematic diagram of the wireless data packet in the view of the sensor node. Normally, the received packet includes 6 useful bytes. The configuration commands take 4 bytes (byte 3 to 6) as shown in the figure. Detailed explanation is presented in the following:

*The original platform was developed by Mickael MOREY, a master student in Polytech Annecy-Chambéry.

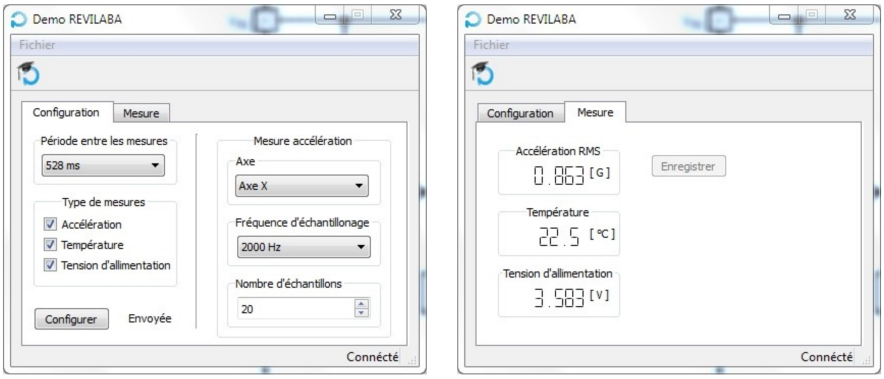

Figure 5.10: UI of the star sensor network system

Received data packet

Byte 1	Byte 2	Byte 3	Byte 4	Byte 5	Byte 6
Size of packet	Command	Configure 1	Configure 2	Configure 3	

Configure 1

Byte	3							
Bit	7	6	5	4	3	2	1	0
	Sleep_time				-	Volt_en	Tem_en	Acc_en

Configure 2

Byte	4							
Bit	7	6	5	4	3	2	1	0
	-	-	Z_en	Y_en	X_en	Sample_freq		

Configure 3

Byte	5								6							
Bit	7	6	5	4	3	2	1	0	7	6	5	4	3	2	1	0
	Sample_point															

Transmit data packet

Byte 1	Byte 2	Byte 3	Byte 4	Byte 5
Size of packet	Command	Acc_data	Tem_data	Volt_data

Figure 5.11: Communication data packets between the two nodes

- **Sleep_time:** inactive duration between 2 cycles of measurement.
  (0000b $\sim$ 1111b: 4 ms $\sim$ 131.072 s)
- **Volt_en:** enable to measure the supply voltage.
  (1: enable; 0: disable)
- **Tem_en:** enable to measure the temperature.
  (1: enable; 0: disable)
- **Acc_en:** enable to measure the alleleration.
  (1: enable; 0: disable)
- **Z_en:** measure the acceleration along with axis z.
  (1: enable; 0: disable)
- **Y_en:** measure the acceleration along with axis y
  (1: enable; 0: disable)
- **X_en:** measure the acceleration along with axis x
  (1: enable; 0: disable)
- **Sample_freq:** the sampling frequency of the acceleration measurement.
  (000b $\sim$ 111b: 15.63 Hz $\sim$ 2000 Hz)
- **Sample_point:** the number of the sampling points of the acceleration, finally the node will calculate the average RMS value based on the whole sample.
  (0000 0000 0000 0000b $\sim$ 1111 1111 1111 1111b: 0 $\sim$ 65535)

The maximal useful transmitted packet is composed of 5 bytes. If all the measured quantities are enabled, the data packet is transmitted as shown in the figure, where each physical quantity is pre-processed in the node and presented by an 8-bit character type data.

5.3.2 Self-powered wireless sensor node

Figure 5.12 shows the schematic diagram of the WSN node including the presented power management unit. Since it is a demo device, the output voltage selection pins D0, D1 of the chip can be easily selected to connect high or low voltage levels by two 2.54 mm pin jumpers. The triaxial acceleration sensor IC named BMA222 is fix in the node. It senses the 3d acceleration of the node and its ambient environment temperature. For the RF transceiver working in 868 MHz frequency band, a balun circuit for 50 Ω antenna is designed according to the datasheet [141].

As a demonstration, the operating program of the self-powered node is very simple. It is shown in Figure 5.13. When the power management chip LTC3588-1 has an output voltage V_{cc}, the power-on reset (POR) pulse is generated on-chip due to the POR hardware circuit. This event is captured by the $\overline{\text{POR}}$ bit of the reset control register and allows the micro-controller to start in the initialized state ('Initial PIC'). In addition, because the node

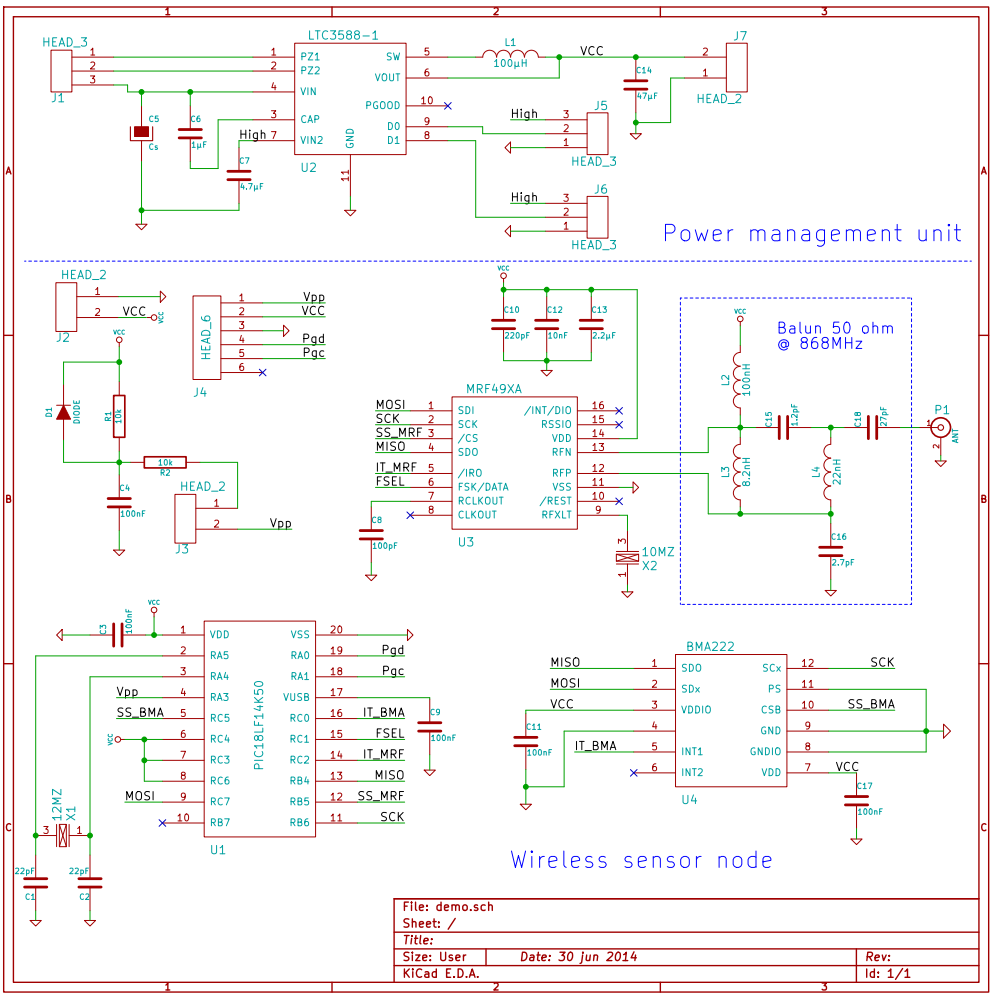

Figure 5.12: Schematic diagram of the sensor node

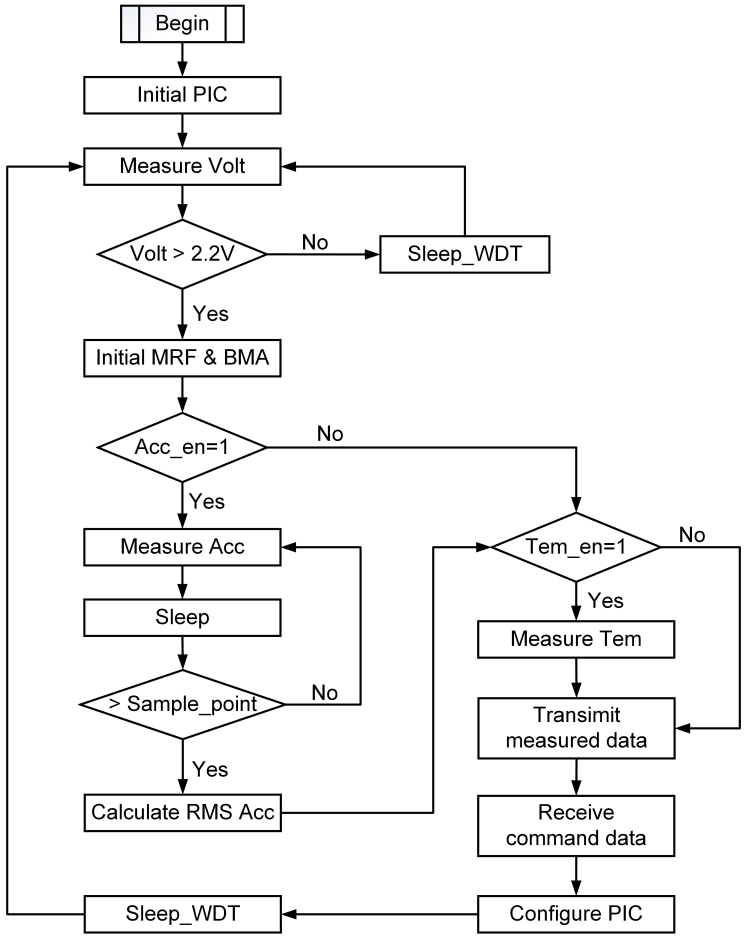

Figure 5.13: Operating program flowcharts of the sensor node

is an autonomous self-powered device, and the power management unit has the UVLO function, in order to start the micro-controller in the following POR pulse, the $\overline{\text{POR}}$ bit of the register should be set to '1' in the 'Initial PIC' program [142].

After the initialized state, the sensor node will first measure the supply voltage V_{cc}. If the value is lower than 2.2 V, the RF transceiver in the node cannot operate normally, the micro-controller will enter the sleep mode, almost all the clock sources will be shut down to reduce the power consumption. However, a low frequency internal oscillator used for a watchdog timer (WDT) will still continue to operate, so that the micro-controller will return back to measure the supply voltage periodically as soon as the timeout interruption is generated by the WDT [142]. If the value of the voltage is adequate for the whole sub-modules' operation, the micro-controller will start to initialize the RF transceiver and the acceleration sensor ICs ('Initial MRF & BMA'). Then, the sensor chip will begin to measure the corresponding physical quantities.

As soon as the sensor node finishes the measurement, it will transmit the data packet to the coordinator node. The coordinator will then immediately send a new data packet to the sensor node to refresh the measurement command for the following operation period.

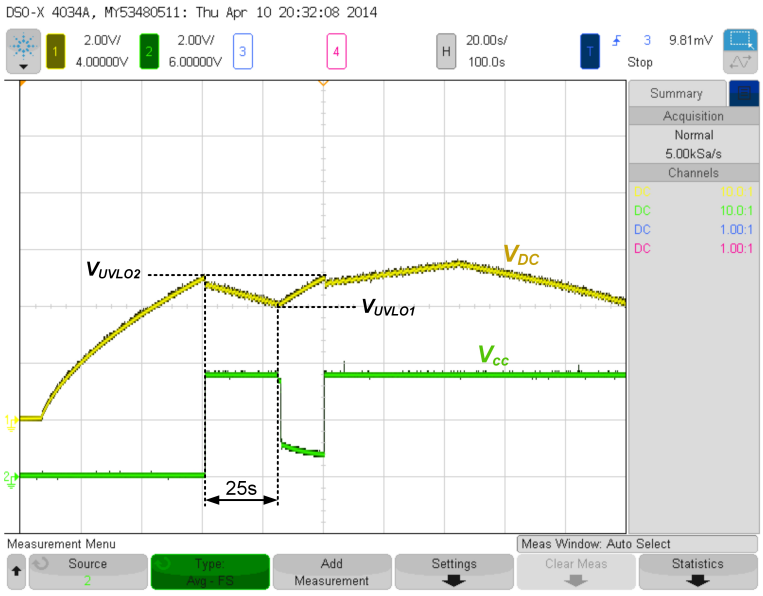

Figure 5.14: Waveforms of the storage and supply voltages in the sensor node

Figure 5.14 shows the waveforms of the storage and supply voltages in the sensor node. At the beginning, the energy stored in the storage capacitor of the node is 0. The output voltage of the power management unit is then 0 ($V_{cc} = 0$). The sensor node cannot operate and stay in the inactive state. When the VEHD starts to harvest energy, the storage voltage begins to increase. In this case, all the harvested energy is stored in the capacitor until the storage voltage reaches the value of rising threshold voltage V_{UVLO2}.

As soon as the storage voltage rises up to V_{UVLO2}, the power management unit starts to provide the supply voltage to the whole device immediately, this event leads to a POR pulse that enable the micro-controller in the node, the self-powered sensor starts to operate as described in Figure 5.13. After operating, if the power consumption of the sensor node is larger than the harvested power of the VEHD, the power management system will use the stored energy in the capacitor in order to satisfy the output power. So the voltage across the storage capacitor will decrease. However, due to the UVLO function, the power management unit will keep on outputting until the voltage is lower than the value of V_{UVLO1} (e.g. the sensor can operate for 25 s as shown in the figure).

When the storage voltage decreases to V_{UVLO1}, the voltage regulator in the power management unit is disabled, and the supply voltage is cut off. After that, if the VEHD still works, the storage capacitor will be totally charged until the powered sensor node restart to operate.

Figure 5.15 shows the waveforms of the output current I_{cc} of the power management system as well as the storage and output voltages. In this configuration, the sensor node operates continuously. The sampling points and frequency of the acceleration are 200 and 500 Hz, respectively. The inactive duration ('Sleep_WDT', WDT timeout period) between

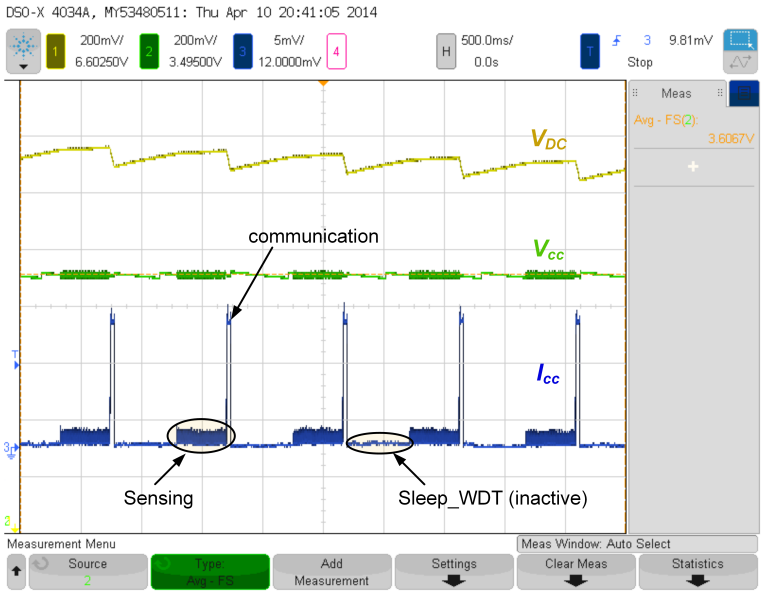

Figure 5.15: Waveforms of the voltages and current in the normal operating sensor node

the 2 cycles of the measurement is set to be 512 ms. Here, we use a current probe from Tektronix© (TCPA300) and an oscilloscope form Agilent Technologies© (DSO-X 4034A) to get the current waveform. It is clearly seen that the maximal power consumption in the wireless sensor node is due to the wireless communication, the current value is about 7 times larger than that due to the sensing measurement. Every times corresponding to the wireless communication, the storage voltage V_{DC} of the device drops drastically. However, during the inactive duration or even the measurements, the average harvested power is higher than the consumption (V_{DC} increase).

5.3.3 Power consumption characteristics of the self-powered node

According to the measured current waveform in the previous subsection, Figure 5.16 gives the simplified power consumption model in the presented sensor node. When the sensor node operates normally, the operation period roughly equals the measurement time plus the inactive duration ('Sleep_WDT') . Based on the simplified assumption shown in the figure, the estimated value of the average power consumption P_{avg} is expressed in equation 5.4, where E_{samp} and E_{RF} is the consumed energy for one sampling point and wireless communication (receive & transmit), respectively. From the equation, it is clearly shown that to reduce the average power consumption, we can enlarge the inactive duration t_{WDT}, and/or decrease the sampling frequency F_{samp}. The influence due to the sampling points N_{samp} depends on the major part of the energy consumption: if the wireless sensor node has not the inactive time ($t_{WDT} = 0$), larger number of the sampling points will help to reduce the frequency of the wireless communication, leads to reduce the average power consumption; if the energy consumption of the sensing process takes an important part, small number of the sampling points will help to decrease the average power consumption.

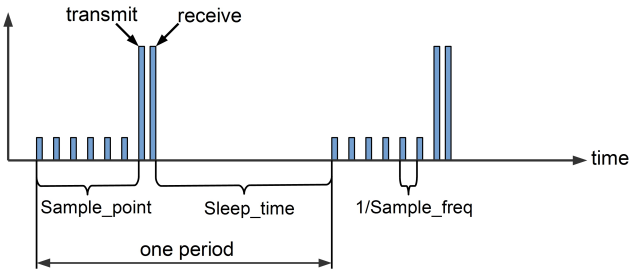

Figure 5.16: Major power consumption in the sensor node

$$P_{avg} = \frac{E_{samp} + \frac{E_{RF}}{N_{samp}}}{\frac{1}{F_{samp}} + \frac{t_{WDT}}{N_{samp}}} \tag{5.4}$$

Experimental power consumptions are presented in Figure 5.17. It shows the detailed values of the node power consumption in different cases. The results are in an agreement with the above equation. Nevertheless, The power consumption in Figure 5.17(c) seems to be much more stable than that in Figure 5.17(a), this is because the range value of the denominator in the equation 5.4 is (51.7 ms, 84.5 ms), which is much smaller than (0.2005 s, 20.005 s) in Figure 5.17(a). Still from Figure 5.17(a), it can be seen that when the inactive duration of the sensor node is longer than 2 s, the average power consumption of the node will be lower than 1 mW under both kinds of supply voltages. So in the practical application, to realize a real self-powered WSN node, it is very important to optimize the duration of 'sleep mode' between 2 cycles of wireless communications. In addition, for a given sensor node device, lower value of the supply voltage allows to reduce the power consumption.

5.4 Experimental comparison in the demonstration platform

The experimental setup in this section is composed of a linear PEG and an electronic self-powered OSECE EEC, shown in Figure 4.6, a power management unit shown in Figure 5.7, as well as a real self-powered WSN node and its coordinator node shown in Figure 5.9. The experiment will compare the harvested performances between the conventional power management unit and the improved one.

The cantilever beam is driven at the frequency of 83 Hz, which is sensitively larger than the resonance frequency (78 Hz). So although the external exciting force amplitude is a constant value, the vibration amplitude of the beam cannot easily be suppressed due to the harvesting process. This case also corresponds to the case u_M presented in chapter 3, and the input power of the PEG can be considered as constant.

In the experiment, as soon as the sensor node is enabled, it operates with the following configuration: the inactive duration is 2.048 s, the sampling points and frequency are 20

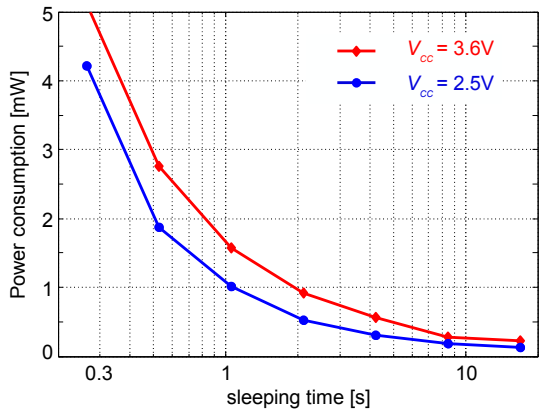

(a) Power consumption as a function of inactive duration (sampling points are 20, sampling frequency is 2000 Hz)

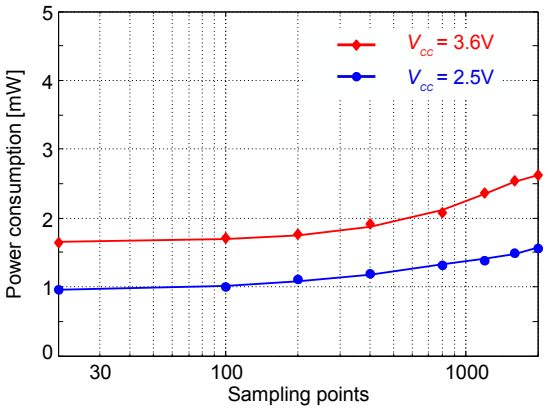

(b) Power consumption as a function of sampling points (inactive duration is 1.024 s, sampling frequency is 2000 Hz)

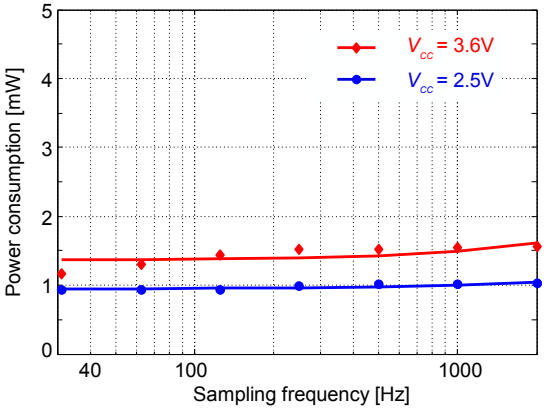

(c) Power consumption as a function of sampling frequency (inactive duration is 1.024 s, sampling points are 20)

Figure 5.17: Classical power consumption characteristics of the sensor node

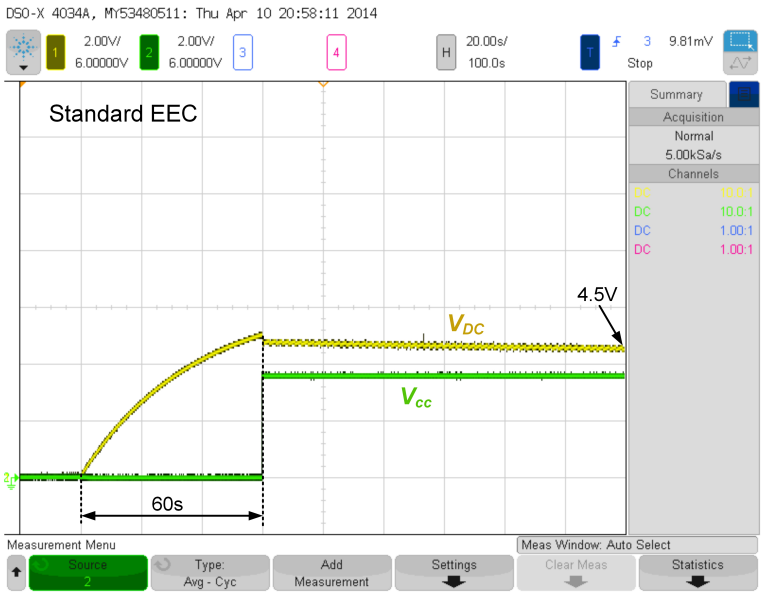

(a) The time history of the storage and supply voltages using the standard EEC

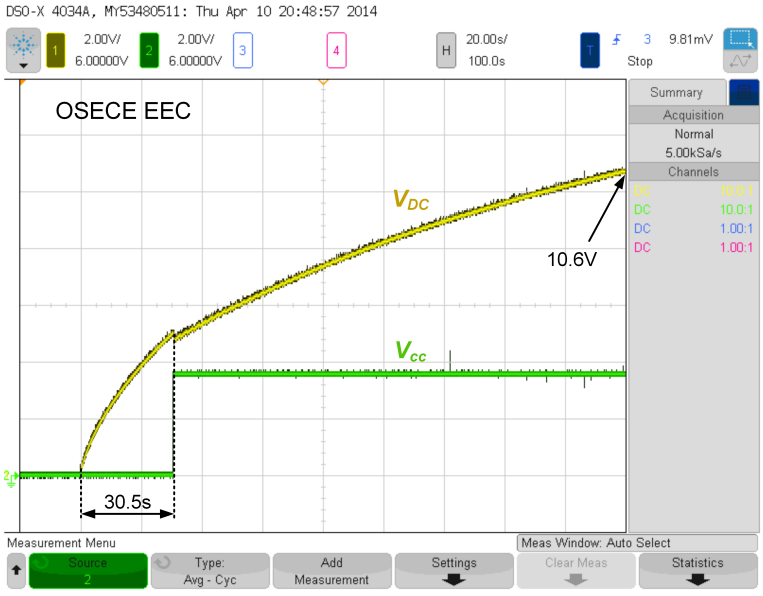

(b) The time history of the storage and supply voltages using the OSECE EEC

Figure 5.18: The time history of the storage and supply voltages in the self-powered node under the same external input power condition

and 2000 Hz, respectively. According to the measured results in the previous section, the average power consumption in the node is about 1 mW ($V_{cc} = 3.6$ V).

Figure 5.18 gives the comparison of these two kinds of power management units. In Figure 5.18(a), we select the standard interface circuit to extract the generated energy, when the VEHD starts to harvest energy, the power management unit cannot supply the output power within 60 s due to the low harvesting effectiveness. After the powered sensor node is enabled, the energy stored in the storage capacitor decreases because the required power is a bit larger than the harvested power. If the harvested power of the VEHD and the power consumption of the sensor node cannot reach a balance point in the range of the operating voltage, or if the required power of the sensor node becomes larger, the power management unit will enter into UVLO mode which disables the powered electronic modules. In Figure 5.18(b), using the improved power management unit interfacing the OSECE EEC, the harvested power is always higher than the consumed power, which leads to an increasing storage voltage. If the required power of the sensor node becomes much larger, the large stored energy can supply the electronic modules for a much longer time.

5.5 Conclusion

This chapter presents a demonstration platform for energy harvesting technologies, it includes a power management unit used to supply a standard DC voltage and a self-powered WSN. In the power management unit, we benefit from the two important functions of the power management chip LTC 3588-1: UVLO and voltage regulator. The first one is one of the key techniques in the self-powered autonomous system that can avoid the uncertain states during the POR event of the sensor device. The second one provides a stable DC voltage to the electronic submodules, makes sure that each submodule can operate normally. It is also shown that combining the LTC 3588-1 chip with the OSECE EEC leads to drastically improve the power management unit.

The main demonstration platform is a very simple WSN (star sensor network), and the power consumption characteristics of the sensor node are theoretically studied. Finally, the demonstration shows a great application potential of the proposed vibration energy harvesting technologies.

General conclusion

Among the potential various energy sources, harvesting ambient vibration energy surrounding a system has been considered as one of the most promising technologies by many researchers. Such technology has received increasing research interest over the last decade. Early investigations mainly focused on optimizing the linear electromechanical structures and the advanced energy extraction interfaces. However, in the vast majority of practical scenarios, ambient vibrations are frequency-varying or totally random with energy distributed over a wide frequency range. Hence, the idea of developing wideband band vibration energy harvesters becomes more and more popular.

This thesis mainly investigates an advanced energy extraction technique named OSECE which is also suitable for wideband vibrations. It is a drastic enhancement from the original SECE technique: the switch control strategy and the circuit are much simpler; the energy conversion effectiveness is enhanced. The harvested powers of them are calculated and compared under two sinusoidal excitation cases. Under the case u_M, the maximal harvested power using the OSECE approach is 2.3 times higher than that using the SECE approach (assuming the quality factor Q_I of the EEC is 5.5). Moreover, the load dependency of the OSECE circuit can be easily reduced by increasing the secondary-primary turns ratio m of the transformer. It is worthy of note that, comparing the experimental results with the theoretical predictions, there exists some energy losses in the SECE and OSECE EECs. Because these losses are mainly due to the nonlinear behaviors of the electronic elements in the circuits, a SPICE software is selected to evaluate the nonlinear energy losses. The results show that the losses can be minimized when the value of the load resistance is in a large medium range [1 kΩ, 500 kΩ].

Since the switch control strategy of the OSECE approach is much simpler, in order to implement the OSECE circuit in practical applications, two self-powered approaches are developed and investigated. If the synchronized switches are realized using electronic switches, an electronic approach using PKD circuits is proposed. The PKD circuits can detect the vibration displacement extreme and provide the electrical energy to drive the corresponding switches synchronously. This approach does not require any additional piezoelectric elements to generate the switch control signal and/or electrical energy. But comparing to the ideal OSECE EEC, a switching phase lag appears on the switch control signal, and the PKD circuits consume a portion of the extracted energy. Based on our

research, it is shown that the switching phase lag does not reduce the maximum harvested power under the case F_M, the power consumption of the PKD circuit strongly depends on the value of the capacitor C_p in the envelope detector. Finally, routes and rules for the optimization of the PKD circuit are summarized.

A mechanical self-powered approach dedicated to the OSECE EEC is also proposed in the thesis. The synchronized switches here are composed of a steel vibrating beam and two copper stoppers. When the tip of the beam hits the stopper, the corresponding switch is closed. So the mechanical switches are passively controlled by the vibration itself, avoiding complex switch control strategies especially in the case of random vibrations. The additional stoppers also introduce a piecewise-linear stiffness in the PEG system, which is also thoroughly studied in the thesis. Such nonlinear stiffness can significantly enlarge the operating bandwidth of the PEG, especially under the external acceleration forward sweep.

In the last chapter, a demonstration platform developed to demonstrate energy harvesting technology is presented. It includes a power management unit used to supply a standard DC voltage and a self-powered WSN. A professional integrated chip named LTC 3588-1 is selected to compose the power management unit, so the unit has the high efficient UVLO and voltage regulator functions. However, for the energy extraction interface, which extracts the electric charges and stores them in the input capacitor of the power management unit, we select the OSECE EEC instead of the standard EEC integrated in the chip. The enhanced power management unit exhibits a higher harvesting effectiveness and stores more electrical energy. The self-powered WSN here is simply composed of a personal computer, a coordinator node and a self-powered sensor node. The power consumption characteristics of the self-powered node thoroughly studied. Finally, the demonstration platform shows a great application potential for the VEHDs.

Bibliography

[1] S. Boisseau, G. Despesse, and B. A. Seddik. Electrostatic Conversion for Vibration Energy Harvesting. In *Small-Scale Energy Harvesting*.

[2] G. W. Hunter, J. R. Stetter, P. J. Hesketh, and C. C. Liu. Smart sensor systems. *The Electrochemical Society Interface*, 19(4):29, 2010.

[3] W. Staszewski, C. Boller, and G. R. Tomlinson. *Health monitoring of aerospace structures: smart sensor technologies and signal processing*. John Wiley & Sons, 2004.

[4] M. Satyanarayanan. Avoiding dead batteries. *IEEE Pervasive Computing*, 4(1):2–3, 2005.

[5] Y. Liu. *Active energy harvesting*. PhD thesis, The Pennsylvania State University, 2006.

[6] C. B. Williams and R. B. Yates. Analysis of a micro-electric generator for microsystems. *Sensors and Actuators A: Physical*, 52:8–11, 1996.

[7] S. Beeby and N. White. *Energy harvesting for autonomous systems*. Artech House, 2010.

[8] S. J. Roundy. *Energy scavenging for wireless sensor nodes with a focus on vibration to electricity conversion*. PhD thesis, University of California, 2003.

[9] F. Ruan, X. Sun, J. Zhang, and C. Li. Battery-free Green Energy Sensor Applied in Wireless Communication Network. *Journal of Network and Information Security*, 4:329–335, 2013.

[10] A. Harb. Energy harvesting: State-of-the-art. *Renewable Energy*, 36(10):2641–2654, October 2011.

[11] Wikipedia. http://en.wikipedia.org/wiki/Energy_harvesting.

[12] S. Roundy, E. S. Leland, J. Baker, E. Carleton, E. Reilly, E. Lai, B. Otis, J. M. Rabaey, V. Sundararajan, and P. K. Wright. Improving Power Output for Vibration-Based Energy Scavengers. *IEEE Pervasive Computing*, 4(1):28–36, January 2005.

[13] Z. Abdin, M.A. Alim, R. Saidur, M.R. Islam, W. Rashmi, S. Mekhilef, and A. Wadi. Solar energy harvesting with the application of nanotechnology. *Renewable and Sustainable Energy Reviews*, 26:837–852, October 2013.

[14] M. Grätzel. Solar energy conversion by dye-sensitized photovoltaic cells. *Inorganic chemistry*, 44(20):6841–51, October 2005.

[15] V. Raghunathan, A. Kansal, J. Hsu, J. Friedman, and M. Srivastava. Design considerations for solar energy harvesting wireless embedded systems. In *Proceedings of the 4th international symposium on Information processing in sensor networks*, page 64. IEEE Press, 2005.

[16] A. Hande, T. Polk, W. Walker, and D. Bhatia. Indoor solar energy harvesting for sensor network router nodes. *Microprocessors and Microsystems*, 31(6):420–432, September 2007.

[17] C. Alippi and C. Galperti. An Adaptive System for Optimal Solar Energy Harvesting in Wireless Sensor Network Nodes. *IEEE Transactions on Circuits and Systems I: Regular Papers*, 55(6):1742–1750, July 2008.

[18] X. Gou, H. Xiao, and S. Yang. Modeling, experimental study and optimization on low-temperature waste heat thermoelectric generator system. *Applied Energy*, 87(10):3131–3136, October 2010.

[19] N. S. Hudak and G. G. Amatucci. Small-scale energy harvesting through thermoelectric, vibration, and radiofrequency power conversion. *Journal of Applied Physics*, 103(10):101301, 2008.

[20] G. J. Snyder and E. S. Toberer. Complex thermoelectric materials. *Nature materials*, 7(2):105–114, 2008.

[21] De C. Marqui and A. Erturk. Airfoil-Based Linear and Nonlinear Electroaeroelastic Energy Harvesting. In *Advances in Energy Harvesting Methods*, pages 269–294. Springer, 2013.

[22] S. Priya, C. T. Chen, D. Fye, and J. Zahnd. Piezoelectric Windmill: A Novel Solution to Remote Sensing. *Japanese Journal of Applied Physics*, 44(3):L104–L107, January 2005.

[23] R. Myers, M. Vickers, H. Kim, and S. Priya. Small scale windmill. *Applied Physics Letters*, 90(5):054106, 2007.

[24] D. Rancourt, A. Tabesh, and L. G. Fréchette. Evaluation of centimeter-scale micro windmills: aerodynamics and electromagnetic power generation. *Proc. PowerMEMS*, pages 93–96, 2007.

[25] F. J. Xu, F. G. Yuan, J. Z. Hu, and Y. P. Qiu. Design of a miniature wind turbine for powering wireless sensors. In *SPIE Smart Structures and Materials+ Nondestructive Evaluation and Health Monitoring*, page 764741. International Society for Optics and Photonics, 2010.

[26] S. Meninger, J. O. Mur-Miranda, R. Amirtharajah, A. P. Chandrakasan, and J. H. Lang. Vibration-to-electric energy conversion. *Very Large Scale Integration (VLSI) Systems, IEEE Transactions on*, 9(1):64–76, 2001.

[27] F. Cottone, P. Basset, H. Vocca, and L. Gammaitoni. Electromagnetic buckled beam oscillator for enhanced vibration energy harvesting. In *2012 IEEE International Conference on Green Computing and Communications, Conference on Internet of Things, and Conference on Cyber, Physical and Social Computing*, pages 624–627,

2012.

[28] E. Arroyo and A. Badel. Electromagnetic vibration energy harvesting device optimization by synchronous energy extraction. *Sensors and Actuators A: Physical*, 171(2):266–273, 2011.

[29] A. Badel. *Récupération d'énergie et contrôle vibratoire par éléments piézoélectriques suivant une approche non linéaire*. PhD thesis, Université de Savoie, 2005.

[30] Y. Y. Chen. *Piezoelectric power transducers and its interfacing circuitry on energy harvesting and structural damping applications*. PhD thesis, École normale supérieure de Cachan-ENS Cachan, 2013.

[31] F. Cottone, L. Gammaitoni, H. Vocca, M. Ferrari, and V. Ferrari. Piezoelectric buckled beams for random vibration energy harvesting. *Smart Materials and Structures*, 21(3):035021, March 2012.

[32] H. Liu, C. J. Tay, C. Quan, T. Kobayashi, and C. Lee. Piezoelectric MEMS Energy Harvester for Low-Frequency Vibrations With Wideband Operation Range and Steadily Increased Output Power. *Journal of Microelectromechanical Systems*, 20(5):1131–1142, October 2011.

[33] A. Erturk, J. M. Renno, and D. J. Inman. Modeling of piezoelectric energy harvesting from an L-shaped beam-mass structure with an application to UAVs. *Journal of intelligent material systems and structures*, 2008.

[34] A. Badel, D. Guyomar, E. Lefeuvre, and C. Richard. Piezoelectric Energy Harvesting using a Synchronized Switch Technique. *Journal of Intelligent Material Systems and Structures*, 17(8-9):831–839, May 2006.

[35] S. Boisseau, G. Despesse, S. Monfray, O. Puscasu, and T. Skotnicki. Semi-flexible bimetal-based thermal energy harvesters. *Smart Materials and Structures*, 22(2):025021, February 2013.

[36] O. Puscasu, S. Monfray, J. Boughaleb, P. J. Cottinet, D. Rapisarda, E. Rouvière, G. Delepierre, Pitone G., C. Maître, F. Boeuf, D. Guyomar, and T. Skotnicki. Flexible bimetal and piezoelectric based thermal to electrical energy converters. *Sensors and Actuators A: Physical*, 214(0):7–14, August 2014.

[37] F. Formosa, A. Badel, and J. Lottin. Equivalent electrical network model approach applied to a double acting low temperature differential Stirling engine. *Energy Conversion and Management*, 78:753–764, February 2014.

[38] F. Formosa and L. G. Fréchette. Scaling laws for free piston Stirling engine design: Benefits and challenges of miniaturization. *Energy*, 57:796–808, August 2013.

[39] H. D. Akaydin, N. Elvin, and Y. Andreopoulos. Flow-Induced Vibrations for Piezoelectric Energy Harvesting. In *Advances in Energy Harvesting Methods*, pages 241–267. Springer, 2013.

[40] C. A. Kitio Kwuimy, G. Litak, M. Borowiec, and C. Nataraj. Performance of a piezoelectric energy harvester driven by air flow. *Applied Physics Letters*, 100(2):024103, 2012.

[41] A. Erturk, O. Bilgen, M. Fontenille, and D. J. Inman. Piezoelectric energy harvesting from macro-fiber composites with an application to morphing-wing aircrafts. In *Proceedings of the 19th International Conference on Adaptive Structures and Technologies, Ascona, Switzerland, Oct*, pages 6–9, 2008.

[42] E. Arroyo, A. Badel, F. Formosa, Y. Wu, and J. Qiu. Comparison of electromagnetic and piezoelectric vibration energy harvesters: Model and experiments. *Sensors and Actuators A: Physical*, 183:148–156, August 2012.

[43] S. R. Anton and H. A. Sodano. A review of power harvesting using piezoelectric materials (2003–2006). *Smart Materials and Structures*, 16(3):R1–R21, June 2007.

[44] A. Erturk and D. J. Inman. An experimentally validated bimorph cantilever model for piezoelectric energy harvesting from base excitations. *Smart Materials and Structures*, 18(2):025009, February 2009.

[45] S. C. Lin and W. J. Wu. Fabrication of PZT MEMS energy harvester based on silicon and stainless-steel substrates utilizing an aerosol deposition method. *Journal of Micromechanics and Microengineering*, 23(12):125028, 2013.

[46] L. Tang, Y. Yang, and C. K. Soh. Broadband Vibration Energy Harvesting Techniques. In *Advances in Energy Harvesting Methods*, pages 17–61. Springer, 2013.

[47] D. Guyomar and M. Lallart. Recent Progress in Piezoelectric Conversion and Energy Harvesting Using Nonlinear Electronic Interfaces and Issues in Small Scale Implementation. *Micromachines*, 2(2):274–294, June 2011.

[48] Y.-Y. Chen, D. Vasic, Y.-P. Liu, and F. Costa. Study of a piezoelectric switching circuit for energy harvesting with bistable broadband technique by work-cycle analysis. *Journal of Intelligent Material Systems and Structures*, 24(2):180–193, September 2012.

[49] W. Liu, A. Badel, F. Formosa, Y. Wu, and A. Agbossou. Wideband energy harvesting using a combination of an optimized synchronous electric charge extraction circuit and a bistable harvester. *Smart Materials and Structures*, 22(12):125038, December 2013.

[50] S. Roundy and Y. Zhang. Toward self-tuning adaptive vibration based microgenerators. In Said F. Al-Sarawi, editor, *Smart Structures, Devices, and Systems II*, volume 5649, pages 373–384, February 2005.

[51] X. Wu, J. Lin, S. Kato, K. Zhang, T. Ren, and L. Liu. A frequency adjustable vibration energy harvester. *Proceedings of PowerMEMS*, pages 245–248, 2008.

[52] C. Eichhorn, F. Goldschmidtboeing, and P. Woias. A frequency tunable piezoelectric energy converter based on a cantilever beam. *Proceedings of PowerMEMS*, 9(12):309–312, 2008.

[53] M. Lallart, S. R. Anton, and D. J Inman. Frequency self-tuning scheme for broadband vibration energy harvesting. *Journal of Intelligent Material Systems and Structures*, 2010.

[54] S. J. Jang, E. Rustighi, M. J. Brennan, Y. P. Lee, and H. J. Jung. Design of a 2DOF

vibrational energy harvesting device. *Journal of Intelligent Material Systems and Structures*, 22(5):443–448, 2011.

[55] O. Aldraihem and A. Baz. Energy harvester with a dynamic magnifier. *Journal of Intelligent Material Systems and Structures*, page 1045389X11402706, 2011.

[56] Y. Tadesse, S. Zhang, and S. Priya. Multimodal energy harvesting system: piezoelectric and electromagnetic. *Journal of Intelligent Material Systems and Structures*, 20(5):625–632, 2009.

[57] Q. Ou, X. Chen, S. Gutschmidt, A. Wood, and N. Leigh. A two-mass cantilever beam model for vibration energy harvesting applications. In *Automation Science and Engineering (CASE), 2010 IEEE Conference on*, pages 301–306. IEEE, 2010.

[58] M. Arafa, W. Akl, A. Aladwani, O. Aldraihem, and A. Baz. Experimental implementation of a cantilevered piezoelectric energy harvester with a dynamic magnifier. In *SPIE Smart Structures and Materials+ Nondestructive Evaluation and Health Monitoring*, pages 79770Q–79770Q. International Society for Optics and Photonics, 2011.

[59] H. Wu, L. Tang, Y. Yang, and C. K. Soh. A novel 2-DOF piezoelectric energy harvester. In *22nd international conference on adaptive structures and technologies (ICAST)*, page 49, Corfu, 2011.

[60] D. F. Berdy, B. Jung, J. F. Rhoads, and D. Peroulis. Increased-bandwidth, meandering vibration energy harvester. In *Solid-State Sensors, Actuators and Microsystems Conference (TRANSDUCERS), 2011 16th International*, pages 2638–2641. IEEE, 2011.

[61] S. M. Shahruz. Design of mechanical band-pass filters for energy scavenging. *Journal of Sound and Vibration*, 292(3):987–998, 2006.

[62] H. Xue, Y. Hu, and Q. M. Wang. Broadband piezoelectric energy harvesting devices using multiple bimorphs with different operating frequencies. *Ultrasonics, Ferroelectrics and Frequency Control, IEEE Transactions on*, 55(9):2104–2108, 2008.

[63] M. Ferrari, V. Ferrari, M. Guizzetti, D. Marioli, and A. Taroni. Piezoelectric multifrequency energy converter for power harvesting in autonomous microsystems. *Sensors and Actuators A: Physical*, 142(1):329–335, 2008.

[64] J. Q. Liu, H. B. Fang, Z. Y. Xu, X. H. Mao, X. C. Shen, D. Chen, H. Liao, and B. C. Cai. A MEMS-based piezoelectric power generator array for vibration energy harvesting. *Microelectronics Journal*, 39(5):802–806, May 2008.

[65] A. Triplett and D. D. Quinn. The Effect of Non-linear Piezoelectric Coupling on Vibration-based Energy Harvesting. *Journal of Intelligent Material Systems and Structures*, 20(16):1959–1967, August 2009.

[66] Samuel C. Stanton, Alper Erturk, Brian P. Mann, and Daniel J. Inman. Nonlinear piezoelectricity in electroelastic energy harvesters: Modeling and experimental identification. *Journal of Applied Physics*, 108(7):074903, 2010.

[67] R. Ramlan, M. J. Brennan, B. R. Mace, and I. Kovacic. Potential benefits of a non-

linear stiffness in an energy harvesting device. *Nonlinear Dynamics*, 59(4):545–558, July 2009.

[68] A. Erturk, J. Hoffmann, and D. J. Inman. A piezomagnetoelastic structure for broadband vibration energy harvesting. *Applied Physics Letters*, 94(25):254102, 2009.

[69] W. Liu, A. Badel, F. Formosa, Y. Wu, and A Agbossou. Novel piezoelectric bistable oscillator architecture for wideband vibration energy harvesting. *Smart Materials and Structures*, 22(3):035013, March 2013.

[70] F. Cottone, H. Vocca, and L. Gammaitoni. Nonlinear energy harvesting. *Physical Review Letters*, 102(8):80601, 2009.

[71] L. Gammaitoni, I. Neri, and H. Vocca. Nonlinear oscillators for vibration energy harvesting. *Applied Physics Letters*, 94(16):164102, 2009.

[72] M. F. Daqaq, R. Masana, A. Erturk, and D. D. Quinn. On the Role of Nonlinearities in Vibratory Energy Harvesting: A Critical Review and Discussion. *Applied Mechanics Reviews*, 66(4):40801, 2014.

[73] Samuel C Stanton, Clark C McGehee, and Brian P Mann. Reversible hysteresis for broadband magnetopiezoelastic energy harvesting. *Applied Physics Letters*, 95(17):174103, 2009.

[74] D. D. Quinn, A. L. Triplett, L. A. Bergman, and A. F. Vakakis. Comparing linear and essentially nonlinear vibration-based energy harvesting. *Journal of vibration and acoustics*, 133(1):11001, 2011.

[75] B. P. Mann, D. A. W. Barton, and B. A. M. Owens. Uncertainty in performance for linear and nonlinear energy harvesting strategies. *Journal of Intelligent Material Systems and Structures*, page 1045389X12439639, 2012.

[76] M. F. Daqaq. Response of uni-modal duffing-type harvesters to random forced excitations. *Journal of Sound and Vibration*, 329(18):3621–3631, 2010.

[77] C. R. McInnes, D. G. Gorman, and M. P. Cartmell. Enhanced vibrational energy harvesting using nonlinear stochastic resonance. *Journal of Sound and Vibration*, 318(4-5):655–662, December 2008.

[78] F. Formosa, T. Büssing, A. Badel, and S. Marteau. Energy harvesting device with enlarged frequency bandwidth based on stochastic resonance. *Proceedings of PowerMEMS*, pages 229–232, 2009.

[79] W. Liu, A. Badel, F. Formosa, Y. Wu, and A. Agbossou. A wideband integrated piezoelectric bistable generator: experimental performances evaluation and potential for real environmental vibrations. *Journal of Intelligent Material Systems and Structures*, 2014.

[80] B. Andò, S. Baglio, C. Trigona, N. Dumas, L. Latorre, and P. Nouet. Nonlinear mechanism in MEMS devices for energy harvesting applications. *Journal of Micromechanics and Microengineering*, 20(12):125020, December 2010.

[81] M. Ferrari, M. Baù, M. Guizzetti, and V. Ferrari. A single-magnet nonlinear piezoelectric converter for enhanced energy harvesting from random vibrations. *Sensors*

and Actuators A: Physical, 172(1):287–292, December 2011.

[82] B. Andò, S. Baglio, F. Maiorca, and C. Trigona. Analysis of two dimensional, wide-band, bistable vibration energy harvester. *Sensors and Actuators A: Physical*, 202:176–182, November 2013.

[83] A. F. Arrieta, P. Hagedorn, A. Erturk, and D. J. Inman. A piezoelectric bistable plate for nonlinear broadband energy harvesting. *Applied Physics Letters*, 97(10):104102, 2010.

[84] R. Masana and M. F. Daqaq. Relative performance of a vibratory energy harvester in mono- and bi-stable potentials. *Journal of Sound and Vibration*, 330(24):6036–6052, November 2011.

[85] W. Liu, A. Badel, F. Formosa, Y. Wu, and A. Agbossou. Design and optimization of a novel bistable power generator for autonomous sensor nodes. In *Design, Test, Integration and Packaging of MEMS/MOEMS (DTIP), 2013 Symposium on*, pages 1–4. IEEE, 2013.

[86] M. S. M. Soliman, E. M. Abdel-Rahman, E. F. El-Saadany, and R. R. Mansour. A wideband vibration-based energy harvester. *Journal of Micromechanics and Microengineering*, 18(11):115021, November 2008.

[87] L. C. J. Blystad, E. Halvorsen, and S. Husa. Piezoelectric MEMS energy harvesting systems driven by harmonic and random vibrations. *IEEE transactions on ultrasonics, ferroelectrics, and frequency control*, 57(4):908–19, April 2010.

[88] H. Liu, C. Lee, T. Kobayashi, C. J. Tay, and C. Quan. Investigation of a MEMS piezoelectric energy harvester system with a frequency-widened-bandwidth mechanism introduced by mechanical stoppers. *Smart Materials and Structures*, 21(3):035005, March 2012.

[89] W. Liu, F. Formosa, A. Badel, Y. Wu, and A. Agbossou. Self-powered nonlinear harvesting circuit with a mechanical switch structure for a bistable generator with stoppers. *Sensors and Actuators A: Physical*, 216(0):106–115, September 2014.

[90] M. J. Guan and W. H. Liao. On the efficiencies of piezoelectric energy harvesting circuits towards storage device voltages. *Smart Materials and Structures*, 16(2):498–505, April 2007.

[91] G. K. Ottman, H. F. Hofmann, A. C. Bhatt, and G. A. Lesieutre. Adaptive piezoelectric energy harvesting circuit for wireless remote power supply. *IEEE Transactions on Power Electronics*, 17(5):669–676, September 2002.

[92] G. K. Ottman, H. F. Hofmann, and G. A. Lesieutre. Optimized piezoelectric energy harvesting circuit using step-down converter in discontinuous conduction mode. *IEEE Transactions on Power Electronics*, 18(2):696–703, March 2003.

[93] D. Vasic and Y. Yao. Pwm interface for piezoelectric energy harvesting. *Electronics Letters*, 49(13):843–845, June 2013.

[94] D. Guyomar, A. Badel, E. Lefeuvre, and C. Richard. Toward energy harvesting using active materials and conversion improvement by nonlinear processing. *IEEE trans-*

actions on ultrasonics, ferroelectrics, and frequency control, 52(4):584–595, 2005.

[95] A. Badel, A. Benayad, E. Lefeuvre, L. Lebrun, C. Richard, and D. Guyomar. Single crystals and nonlinear process for outstanding vibration-powered electrical generators. *Ultrasonics, Ferroelectrics and Frequency Control, IEEE Transactions on*, 53(4):673–684, 2006.

[96] C. Richard, D. Guyomar, D. Audigier, and G. Ching. Semi-passive damping using continuous switching of a piezoelectric device. In *1999 Symposium on Smart Structures and Materials*, pages 104–111. International Society for Optics and Photonics, 1999.

[97] Y. C. Shu, I. C. Lien, and W. J. Wu. An improved analysis of the SSHI interface in piezoelectric energy harvesting. *Smart Materials and Structures*, 16(6):2253–2264, December 2007.

[98] L. Garbuio, M. Lallart, D. Guyomar, C. Richard, and D. Audigier. Mechanical Energy Harvester With Ultralow Threshold Rectification Based on SSHI Nonlinear Technique. *IEEE Transactions on Industrial Electronics*, 56(4):1048–1056, April 2009.

[99] J. Liang and W. H. Liao. On the Influence of Transducer Internal Loss in Piezoelectric Energy Harvesting with SSHI Interface. *Journal of Intelligent Material Systems and Structures*, 22(5):503–512, March 2011.

[100] I. C. Lien, Y. C. Shu, W. J. Wu, S. M. Shiu, and H. C. Lin. Revisit of series-SSHI with comparisons to other interfacing circuits in piezoelectric energy harvesting. *Smart Materials and Structures*, 19(12):125009, December 2010.

[101] X. Wang and L. Lin. Dimensionless optimization of piezoelectric vibration energy harvesters with different interface circuits. *Smart Materials and Structures*, 22(8):085011, August 2013.

[102] J. Qiu, H. Jiang, H. Ji, and K. Zhu. Comparison between four piezoelectric energy harvesting circuits. *Frontiers of Mechanical Engineering in China*, 4(2):153–159, March 2009.

[103] E. Lefeuvre, A. Badel, C. Richard, L. Petit, and D. Guyomar. A comparison between several vibration-powered piezoelectric generators for standalone systems. *Sensors and Actuators A: Physical*, 126(2):405–416, February 2006.

[104] M. Deterre, E. Lefeuvre, and E. Dufour-Gergam. An active piezoelectric energy extraction method for pressure energy harvesting. *Smart Materials and Structures*, 21(8):085004, August 2012.

[105] W. J. Wu, A. M. Wickenheiser, T. Reissman, and E. Garcia. Modeling and experimental verification of synchronized discharging techniques for boosting power harvesting from piezoelectric transducers. *Smart Materials and Structures*, 18(5):055012, May 2009.

[106] M. Lallart, C. Richard, L. Garbuio, L. Petit, and D. Guyomar. High efficiency, wide load bandwidth piezoelectric energy scavenging by a hybrid nonlinear approach.

Sensors and Actuators A: Physical, 165(2):294–302, February 2011.

[107] E. Lefeuvre, A. Badel, C. Richard, and D. Guyomar. Piezoelectric Energy Harvesting Device Optimization by Synchronous Electric Charge Extraction. *Journal of Intelligent Material Systems and Structures*, 16(10):865–876, October 2005.

[108] M. Lallart, L. Garbuio, L. Petit, C. Richard, and D. Guyomar. Double synchronized switch harvesting (DSSH): a new energy harvesting scheme for efficient energy extraction. *IEEE transactions on ultrasonics, ferroelectrics, and frequency control*, 55(10):2119–30, October 2008.

[109] H. Shen, J. Qiu, H. Ji, K. Zhu, and M. Balsi. Enhanced synchronized switch harvesting: a new energy harvesting scheme for efficient energy extraction. *Smart Materials and Structures*, 19(11):115017, November 2010.

[110] M. Lallart and D. Guyomar. Piezoelectric conversion and energy harvesting enhancement by initial energy injection. *Applied Physics Letters*, 97(1):014104, 2010.

[111] P. Becker, E. Hymon, B. Folkmer, and Y. Manoli. High efficiency piezoelectric energy harvester with synchronized switching interface circuit. *Sensors and Actuators A: Physical*, 202:155–161, November 2013.

[112] Y. Wu, A. Badel, F. Formosa, W. Liu, and A. Agbossou. Piezoelectric vibration energy harvesting by optimized synchronous electric charge extraction. *Journal of Intelligent Material Systems and Structures*, 24(12):1445–1458, December 2013.

[113] Y. Wu, A. Badel, F. Formosa, W. Liu, and A. Agbossou. Self-powered optimized synchronous electric charge extraction circuit for piezoelectric energy harvesting. *Journal of Intelligent Material Systems and Structures*, page 1045389X13517315, 2014.

[114] S. Shimose, K. Makihara, and J. Onoda. Energy Harvesting Using an Analog Circuit under Multimodal Vibration. *Smart Materials Research*, 2013:1–6, 2013.

[115] M. Lallart, E. Lefeuvre, C. Richard, and D. Guyomar. Self-powered circuit for broadband, multimodal piezoelectric vibration control. *Sensors and Actuators A: Physical*, 143(2):377–382, May 2008.

[116] Wikipedia. http://en.wikipedia.org/wiki/Envelope_detector.

[117] M. Lallart and D. Guyomar. An optimized self-powered switching circuit for nonlinear energy harvesting with low voltage output. *Smart Materials and Structures*, 17(3):035030, June 2008.

[118] J. Liang and W. H. Liao. Improved design and analysis of self-powered synchronized switch interface circuit for piezoelectric energy harvesting systems. *Industrial Electronics, IEEE Transactions on*, 59(4):1950–1960, 2012.

[119] Y. P. Liu and D. Vasic. Self-Powered Electronics for Piezoelectric Energy Harvesting Devices. In *Small Scale Energy Harvesting*, pages 327–346. 2012.

[120] Y. Y. Chen, D. Vasic, F. Costa, W. J. Wu, and C. K. Lee. Self-powered piezoelectric energy harvesting device using velocity control synchronized switching technique. In *IECON 2010 - 36th Annual Conference on IEEE Industrial Electronics Society*, pages 1785–1790, Phoenix, USA, November 2010. Ieee.

[121] F. Giusa, A. Giuffrida, C. Trigona, B. Andò, A. R. Bulsara, and S. Baglio. "Random Mechanical Switching Harvesting on Inductor": A novel approach to collect and store energy from weak random vibrations with zero voltage threshold. *Sensors and Actuators A: Physical*, 198:35–45, August 2013.

[122] Y. Wu, A. Badel, F. Formosa, W. Liu, and A. Agbossou. Nonlinear vibration energy harvesting device integrating mechanical stoppers used as synchronous mechanical switches. *Journal of Intelligent Material Systems and Structures*, page 1045389X14533437, 2014.

[123] L. Mateu, C. Codrea, N. Lucas, M. Pollak, and P. Spies. Human body energy harvesting thermogenerator for sensing applications. In *Sensor Technologies and Applications, 2007. SensorComm 2007. International Conference on*, pages 366–372. IEEE, 2007.

[124] P. D. Mitcheson and T. T. Toh. Power management electronics. In *Energy Harvesting for Autonomous Systems*, pages 159–209. Artech House Publishers, 2010.

[125] H. Yang and Y. Zhang. Analysis of Supercapacitor Energy Loss for Power Management in Environmentally Powered. 28(11):5391–5403, 2013.

[126] H. Kim, Y. Tadesse, and S. Priya. Piezoelectric energy harvesting. In *Energy Harvesting Technologies*, pages 3–39. Springer, 2009.

[127] E. Lefeuvre, A. Badel, C. Richard, and D. Guyomar. Energy harvesting using piezoelectric materials: Case of random vibrations. *Journal of Electroceramics*, 19(4):349–355, February 2007.

[128] M. Pozzi and M. Zhu. Plucked Piezoelectric Bimorphs for Energy Harvesting. In *Advances in Energy Harvesting Methods*, pages 119–140. Springer, 2013.

[129] H. Liu, C. Lee, T. Kobayashi, C. J. Tay, and C. Quan. Piezoelectric MEMS-based wideband energy harvesting systems using a frequency-up-conversion cantilever stopper. *Sensors and Actuators A: Physical*, 186:242–248, October 2012.

[130] F. Maiorca, F. Giusa, C. Trigona, B. Andò, A. R. Bulsara, and S. Baglio. Diodeless mechanical H-bridge rectifier for "zero threshold" vibration energy harvesters. *Sensors and Actuators A: Physical*, 201:246–253, October 2013.

[131] E. Lefeuvre, A. Badel, L. Petit, C. Richard, and D. Guyomar. Semi-passive piezoelectric structural damping by synchronized switching on voltage sources. *Journal of Intelligent Material Systems and Structures*, 17(8-9):653–660, 2006.

[132] Y. Wang and D. J. Inman. A survey of control strategies for simultaneous vibration suppression and energy harvesting via piezoceramics. *Journal of Intelligent Material Systems and Structures*, 23(18):2021–2037, May 2012.

[133] H. Ji, J. Qiu, P. Xia, and D. Inman. Coupling analysis of energy conversion in multimode vibration structural control using a synchronized switch damping method. *Smart Materials and Structures*, 21(1):015013, January 2012.

[134] H. Ji, J. Qiu, P. Xia, and D. Inman. Analysis of energy conversion in switched-voltage control with arbitrary switching frequency. *Sensors and Actuators A: Phys-*

ical, 174:162–172, February 2012.

[135] I. Neri, F. Travasso, R. Mincigrucci, H. Vocca, F. Orfei, and L. Gammaitoni. A real vibration database for kinetic energy harvesting application. *Journal of Intelligent Material Systems and Structures*, 23(18):2095–2101, May 2012.

[136] A. Erturk and D. J. Inman. Broadband piezoelectric power generation on high-energy orbits of the bistable Duffing oscillator with electromechanical coupling. *Journal of Sound and Vibration*, 330(10):2339–2353, May 2011.

[137] Wikipedia. http://en.wikipedia.org/wiki/Voltage_regulator.

[138] Analog devices. http://www.analog.com/en/content/ta_fundamentals_of _voltage_regulators/fca.html.

[139] Linear technology. http://www.linear.com/product/LTC3588-1.

[140] Linear technology. Piezoelectric energy harvesting power supply, LTC3588-1 datasheet.

[141] Microchip. Ism band sub-ghz rf transceiver, MRF49XA datasheet.

[142] Microchip. 20-pin usb flash microcontrollers with nanowatt xlp technology, PIC18F/LF1XK50 datasheet.

[143] A. Badel, M. Lagache, D. Guyomar, E. Lefeuvre, and C. Richard. Finite element and simple lumped modeling for flexural nonlinear semi-passive damping. *Journal of intelligent material systems and structures*, pages 727–742, 2007.

List of publications

International journals

[1] **Yipeng WU**, Adrien Badel, Fabien Formosa, Weiqun Liu and Amen Agbossou. Piezoelectric vibration energy harvesting by optimized synchronous electric charge extraction. *Journal of Intelligent Material Systems and Structures*, vol 24, no. 12, pp. 1445-1458, December 2012.

[2] **Yipeng WU**, Adrien Badel, Fabien Formosa, Weiqun Liu and Amen Agbossou. Self-powered optimized synchronous electric charge extraction circuit for piezoelectric energy harvesting. *Journal of Intelligent Material Systems and Structures*, 2014.

[3] **Yipeng WU**, Adrien Badel, Fabien Formosa, Weiqun Liu and Amen Agbossou. Nonlinear vibration energy harvesting device integrating mechanical stoppers used as synchronous mechanical switches. *Journal of Intelligent Material Systems and Structures*, 2014.

[4] Emmanuelle Arroyo, Adrien Badel, Fabien Formosa, **Yipeng WU** and Jinhao Qiu. Comparison of electromagnetic and piezoelectric vibration energy harvesters: model and experiments. *Sensors and Actuators A: Physical*, vol 183, pp. 148-156, August 2012.

[5] Weiqun Liu, Adrien Badel, Fabien Formosa, **Yipeng WU** and Amen Agbossou. Novel piezoelectric bistable oscillator architecture for wideband vibration energy harvesting. *Smart Materials and Structures*, 2013: 035013.

[6] Weiqun Liu, Adrien Badel, Fabien Formosa, **Yipeng WU** and Amen Agbossou. Wideband energy harvesting using a combination of an optimized synchronous electric charge extraction circuit and a bistable harvester. *Smart Materials and Structures*, 2013: 125038.

[7] Weiqun Liu, Fabien Formosa, Adrien Badel, **Yipeng WU** and Amen Agbossou. Self-powered nonlinear harvesting circuit with a mechanical switch structure for a bistable generator with stoppers. *Sensors and Actuators A: Physical*, vol 216, pp. 106-115, September 2014.

[8] Weiqun Liu, Adrien Badel, Fabien Formosa, **Yipeng WU** and Amen Agbossou. A wideband integrated piezoelectric bistable generator: experimental performances evaluation and potential for real environmental vibrations. *Journal of Intelligent Material Systems and Structures*, 2014.

International conferences

[9] **Yipeng WU**, Adrien Badel, Fabien Formosa, Weiqun Liu and Amen Agbossou. Vibration energy extraction circuit optimization by optimized synchronous electric charge extraction and its self-powered circuit. *The 23rd International Conference on Adaptive Structures and Technologies (ICAST 2012)*, October 2012, Nanjing, China.

[10] **Yipeng WU**, Adrien Badel, Fabien Formosa, Weiqun Liu and Amen Agbossou. Two self-powered energy harvesting interfaces based on the optimized synchronous electric charge extraction technique. *The 13th International Conference on Micro and Nanotechnology for Power Generation and Energy Conversion Applications (PowerMEMS 2013)*, December 2013, London, UK.

[11] Weiqun Liu, Adrien Badel, Fabien Formosa, **Yipeng WU** and Amen Agbossou. Design and optimization of a novel bistable power generator for autonomous sensor nodes. *Design, Test, Integration and Packaging of MEMS/MOEMS (DTIP 2013)*, April 2013, Barcelona, Spain.

[12] Weiqun Liu, Adrien Badel, Fabien Formosa, **Yipeng WU** and Amen Agbossou. Integrated bistable generator for wideband energy harvesting with optimized synchronous electric charge extraction circuit. *The 13th International Conference on Micro and Nanotechnology for Power Generation and Energy Conversion Applications (PowerMEMS 2013)*, December 2013, London, UK.

[13] Adrien Badel, Fabien Formosa, Emmanuelle Arroyo, **Yipeng WU** and Weiqun Liu. Wide band vibration energy harvesting for wireless sensor nodes. *2nd Symposium Japanese-French Frontiers of Engineering (JFFoE 2012)*, February 2012, Kyoto, Japan.

List of Figures

List of Tables

A

Initial energy injection interface circuit

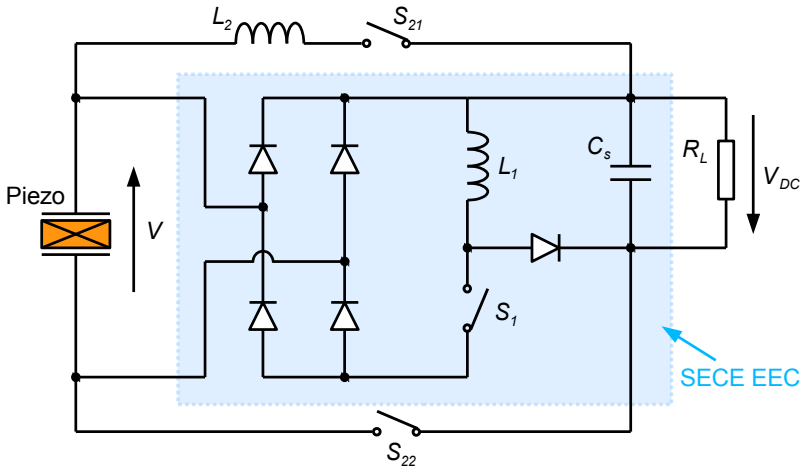

Figure A.1: Initial energy injection circuit

The OSECE and the initial energy injection approaches are both improvements of the former SECE technique. The energy extraction stages in these two EECs are similar, and the harvested powers are almost the same, but the electronic circuitries and the synchronous switching control strategies between them are very different. In this appendix, the theoretical operating principle of the initial energy injection approach will be presented and compared with the OSECE approach.

A.1 Presentation of the initial energy injection EEC

The initial energy injection EEC is shown in Figure A.1. It includes a SECE circuit and an energy injection circuit. The operation processes in this EEC can be divided into 3 stages:

- Stage '1': Energy extraction using the SECE technique;
- Stage '2': Energy injection from the storage element to the piezoelectric element;
- Stage '-' or '+': Piezoelectric element is open-circuited, the piezoelectric voltage is proportional to the PEG displacement ('-' and '+' correspond to the polarity of the voltage).

The above stages are noted in Figure A.2, which also shows the waveforms of the displacement, the piezoelectric voltage, as well as the piezoelectric outgoing current [110].

Most of the time, the piezoelectric element is open-circuited (in stage '+'). As soon as the displacement of the PEG reaches a maximum, so do the voltage on the piezoelectric element (V_M). Stage '1' starts, and the switch S_1 is closed for a short time t_{SECE}. All the electric charges accumulated on the piezoelectric element are then extracted by the SECE technique. From the presented study in chapter 3, the obtained energy can be expressed as equation A.1.

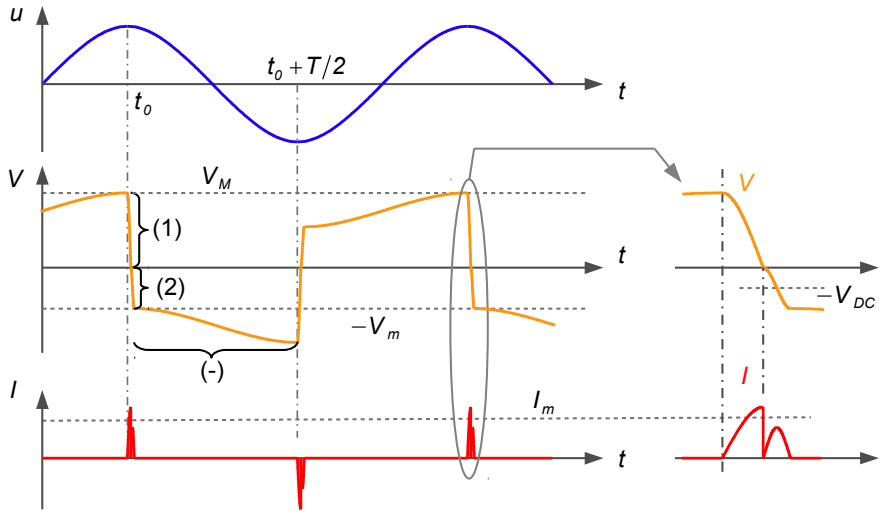

Figure A.2: Initial energy injection waveforms of displacement (u), voltage (V) and current (I)

$$E_{obt} = \frac{1}{2} C_0 V_M^2 \mathrm{e}^{-\frac{\pi}{2Q_I}} \tag{A.1}$$

After the SECE event, stage '2' occurs, energy is provided from the storage capacitance C_s to the piezoelectric element. In order to reduce the losses, the energy injection is done through the inductor L_2, this $\{L_2\ C_0\}$ circuit will reverse the piezoelectric voltage around $-V_{DC}$, leading to the value of the initial voltage at the beginning of stage '-', given in equation A.2, where Q_i is the quality factor of the energy injection circuit. Hence the injected energy outgoing from the storage capacitance C_s is expressed by equation A.3. The global harvested power using initial energy injection EEC is finally given in equation A.4.

During stage '-', the piezoelectric element is in open-circuit condition, the outgoing current I is null, integrating equation 2.3 over the time between instant t_0 and $t_0 + T/2$ leads to equation A.5 that gives the relationship between the maximum voltage V_M and the displacement amplitude u_M.

$$V_{init} = V_m = V_{DC}\left(1 + \mathrm{e}^{-\frac{\pi}{2Q_i}}\right) \tag{A.2}$$

$$E_{inj} = C_0 V_{DC}^2 \left(1 + \mathrm{e}^{-\frac{\pi}{2Q_i}}\right) \tag{A.3}$$

$$P^{init} = (E_{obt} - E_{inj})\frac{\omega}{\pi} = \frac{V_{DC}^2}{R_L} \tag{A.4}$$

$$V_M = V_m + 2\frac{\alpha}{C_0} u_M \tag{A.5}$$

Initial energy injection circuit in case u_M:

In this case, the PEG vibration amplitude u_M is constant, according to the above equations, the harvested power in then expressed as a function of the vibration amplitude u_M, the load resistance R_L, and the quality factors Q_I, Q_i of the SECE and energy injection circuits, as shown in equation A.6.

$$\begin{cases} P_u^{init} = \frac{2\alpha^2\omega\gamma_I}{\pi C_0}\left\{\frac{(1+\gamma_i)\sqrt{2\pi R_L C_0\omega\gamma_I}+\sqrt{4\pi R_L C_0\omega(1+\gamma_i)+4\pi^2}}{R_L C_0\omega[2-(1+\gamma_i)\gamma_I](1+\gamma_i)+2\pi}\right\}u_M^2 \\ \gamma_I = \mathrm{e}^{-\frac{\pi}{2Q_I}} \\ \gamma_i = \mathrm{e}^{-\frac{\pi}{2Q_i}} \end{cases} \tag{A.6}$$

Initial energy injection circuit in case F_M:

In this case, the VEHD system is excited at its resonance frequency undergoing a sinusoidal force $F = F_M \sin(\omega t)$. The vibration displacement of the linear structure is assumed as a sinusoidal signal $u = u_M \sin(\omega t + \varphi_u)$. According to equation 2.3 and the piezoelectric voltage waveform shown in Figure A.2, a piecewise piezoelectric voltage induced by the initial energy injection EEC is expressed as equation A.7. Where h is a crenel function defined in equation A.8. Only the first harmonic of the crenel is considered here since the displacement is assumed to remain sinusoidal [143].

$$V = \frac{\alpha}{C_0}u + h \tag{A.7}$$

$$h = \left(V_m + \frac{\alpha}{C_0}u_M\right)\mathrm{sign}(\dot{u}) \approx \left(V_m + \frac{\alpha}{C_0}u_M\right)\frac{4}{\pi}\cos(\omega t + \varphi_u) \tag{A.8}$$

The dynamic equilibrium equation A.9 is obtained from the original dynamic equation 2.5 given in chapter 2. Because the system operates at its resonance frequency, it can be assumed that the external force F and the velocity $\dot{u}$ are in phase. Hence, the relationship between the vibration amplitude u_M and the force amplitude F_M is given by A.10, which means that the energy scavenging process leads to a reduction of the vibration amplitude in this case. Finally, equation A.11 gives the expression of u_M as a function of the external force amplitude F_M. Substituting equation A.11 into equation A.6 can lead to the expression of the harvested power, although it will not be given here for conciseness.

$$F = M\ddot{u} + K_0 u + D_0\dot{u} + \frac{\alpha^2}{C_0}u + \alpha h \tag{A.9}$$

$$F_M = \left(D_0\omega + \frac{4\alpha^2}{\pi C_0}\right)u_M + \frac{4\alpha}{\pi}V_m \tag{A.10}$$

$$\begin{cases} u_M = \frac{F_M}{D_0\omega+\frac{4\alpha^2}{\pi C_0}\left\{1+2(1+\gamma_i)\frac{\gamma_I(1+\gamma_i)R_L C_0\omega+\sqrt{\gamma_I R_L C_0\omega[(1+\gamma_i)R_L C_0\omega+\pi]}}{[2-\gamma_I(1+\gamma_i)](1+\gamma_i)R_L C_0\omega+2\pi}\right\}} \\ \gamma_I = \mathrm{e}^{-\frac{\pi}{2Q_I}} \\ \gamma_i = \mathrm{e}^{-\frac{\pi}{2Q_i}} \end{cases} \tag{A.11}$$

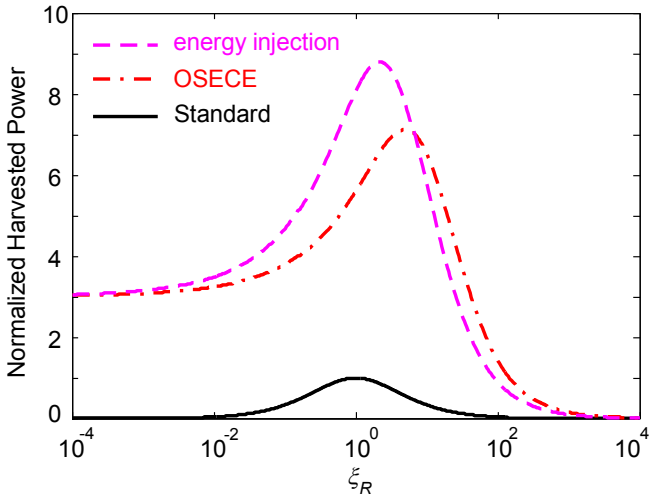

Figure A.3: Normalized harvested powers under the case u_M ($Q_I = 5.5,\ Q_i = 5.5,\ m = 1$)

A.2 Performances comparison between the two EECs derived from the SECE technique

The aim of this section is to compare the theoretical harvested power for the OSECE and initial energy injection EECs. The same normalization as that in chapter 3 is used in order to make the comparison as generic as possible.

Case u_M:

Figure A.3 shows the curves of the normalized harvested powers as a function of the load resistance coefficient ξ_R. The OSECE and initial energy injection EECs have similar characteristics: the harvested powers are enhanced; the load dependencies are much lower (compare with the standard EEC); and for low value of ξ_R, both the performances are very closed to the SECE approach, for high value of ξ_R, both the harvested powers tend to 0 as the great parts are lost due to the quality factors of the EECs. In this figure, the maximal power using the energy injection approach is slightly larger. However, the band of the load for the OSECE EEC can be easily designed by changing the turns ratio m of the flyback transformer, while the band of the load is a relative constant value in the initial energy injection EEC.

Case F_M:

Figure A.3 shows the maximal normalized powers as a function of $k_m^2 Q_m$, which means that the value of ξ_R is optimized for both the OSECE and initial energy injection approaches. Both the curves of the nonlinear EECs are very similar, and they are always lower to 1, which confirm the presented conclusion that the harvested powers in this case are always lower than the limit power due to the quality factors of the circuits. In addition, the limit power using initial energy injection EEC is only due to the quality factor Q_I of the SECE circuit. This is because when $k_m^2 Q_m$ raises, the initial energy injection

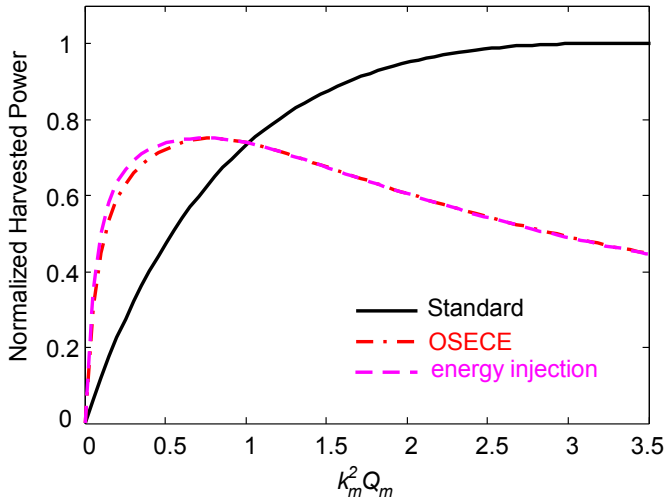

Figure A.4: Normalized harvested powers under the case F_M ($Q_I = 5.5$)

EEC induces stronger damping effect, the optimal value of ξ_R is then shifted to the lower value. In this case, almost no energy is injected to the piezoelectric element, leading to the same performance as that in the SECE EEC. However, in the low value of $k_m^2 Q_m$, the performance of the initial energy injection EEC is slightly better than that of the OSECE EEC, though its circuitry is much more complicated to be implemented.

B

Programmable load resistance box

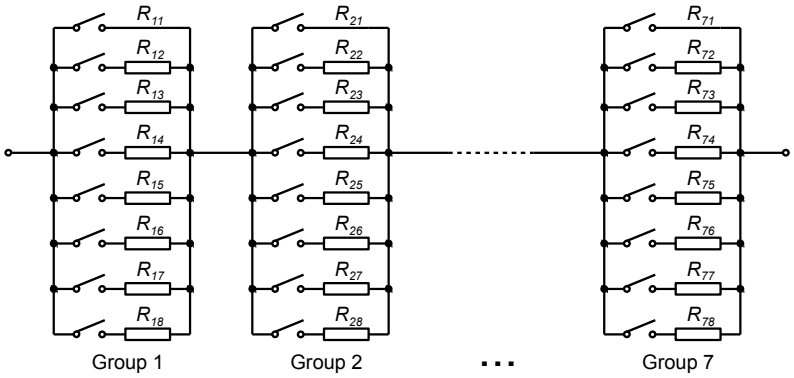

Figure B.1: Schematic representation of the resistor network

As discussed in the previous chapters, the input impedances of EECs usually affect the energy conversion of the PEGs. Since the input impedance of most EECs has a relationship with the equivalent load resistance R_L of the circuity to be supplied, the harvested powers of these EECs are load-dependent. Even in the load-independent EECs, some additional electrical losses are induced due to the nonlinear behaviors of the electronic components. The values of the losses are also fluctuant as a function of R_L. So we need to change the value of R_L and then measure the harvested powers in various EECs. This is an important evaluation among the different EECs, the more values the R_L, the more comprehensive the evaluation. Considering the general applications and requirements, the variation range of R_L should be broad, and each value in the range should be achievable.

For this reason, a programmable load resistance box is specially developed for our experimental evaluations. The technical index is: variation range of the resistance R_L is $0 \sim 2.09\ \mathrm{M}\Omega$ and minimum step is $1\ \Omega$. Because in the experiments, we usually use a prototyping solution dSPACE to generate and acquire the analog signals, or even to control the whole experimental process, the resistance box has to be also automatically controlled by this prototyping solution.

Figure B.1 shows the schematic of the resistor network inside the box. The network is divided into 7 groups, each group has 8 switches and resistors (the first resistance in each group is 0). Relay switches (TSC-105L3H, Tyco Electronics©) are selected their on-resistance can be neglected. In addition, the switches are controlled by the DIOs in the dSPACE solution through the darlington transistor arrays named ULN2003A (STMicroelectronics©).

In order to realize the presented technical requirements, the values of the resistors are given in equation B.1, where i is the group number between 1 to 7, and j is position number in each group. When the resistor network is operating, only one relay switch in each group is driven to close, the other 7 switches are in open condition. So the equivalent load resistance R_L is expressed by B.2, in which j is the position number of the closed

Table B.1: Real value of the selected resistors

j \ i	1	2	3	4	5	6	7
1	0	0	0	0	0	0	0
2	1	7.87	63.4	511	4.12k	33k	261k
3	2	16	127	1.02k	8.2k	64.9k	523k
4	3	24	191	1.54k	12.4k	97.6k	787k
5	4	32.4	255	2.05k	16.5k	130k	1M
6	5	40.2	316	2.55k	20.5k	165k	1.3M
7	5.9	47.5	383	3.09k	24.3k	196k	1.6M
8	7.15	56	442	3.57k	28.7k	232k	1.82M

switch. If the values of j are all 1 in each group, the load resistance R_L will become 0, and if the values of j are all 8, the load resistance R_L will reach its maximum $(2^{21}-1)\ \Omega$.

$$R_{ij} = (j-1)\,2^{3(i-1)} \tag{B.1}$$

$$R_L = \sum_{i=1}^{7} R_{ij} \quad (1 \leqslant j \leqslant 8) \tag{B.2}$$

However, in the practical development, it is complicated to directly buy the exact value of the resistor expressed in equation B.1. The closest values shown in Table B.1 are then considered in the real resistor network. Comparing with the exactly calculated value, these real values are irregular. So it is very difficult to find a simple relationship between the DIOs output control signal and the real equivalent load resistance R_L. For this reason, a table lookup method is selected in the program.

According to the technical index, the load resistance box has 2^{21} output resistances. Which means if all the outputs are listed in the same table, this table will be very huge, and it will take a very long time for looking up an accurate output resistance. For this reason, we divide the resistor network into two parts. The first part is a low resistance table (LowResTab) which consists of the first 4 groups of the resistors. The second part is a high resistance table (HigResTab) which consists of the last 3 groups of the resistors. The equivalent resistances in each part are listed in their own tables, the total listed number in the two tables is then reduced to 4608 ($8^4 + 8^3$). That decreases the lookup time of the programmable system very much. Figure B.2 gives the lookup algorithm as well as the flowcharts of the program. Where LowResTab(4096,8) is the maximal resistance (4075 Ω) in the low resistance table, HigResTab(2,8) is the minimal resistance (4120 Ω) in the high resistance table. HigResTab(1,8) is 0, which means the output of the resistance box mainly consists of the first 4 groups of the resistor, the high resistance part is short

circuited. LowResTab(:,1:4) plus HigResTab(:,5:7) are the dSPACE DIOs output control commands correspond to the load resistance R_L.

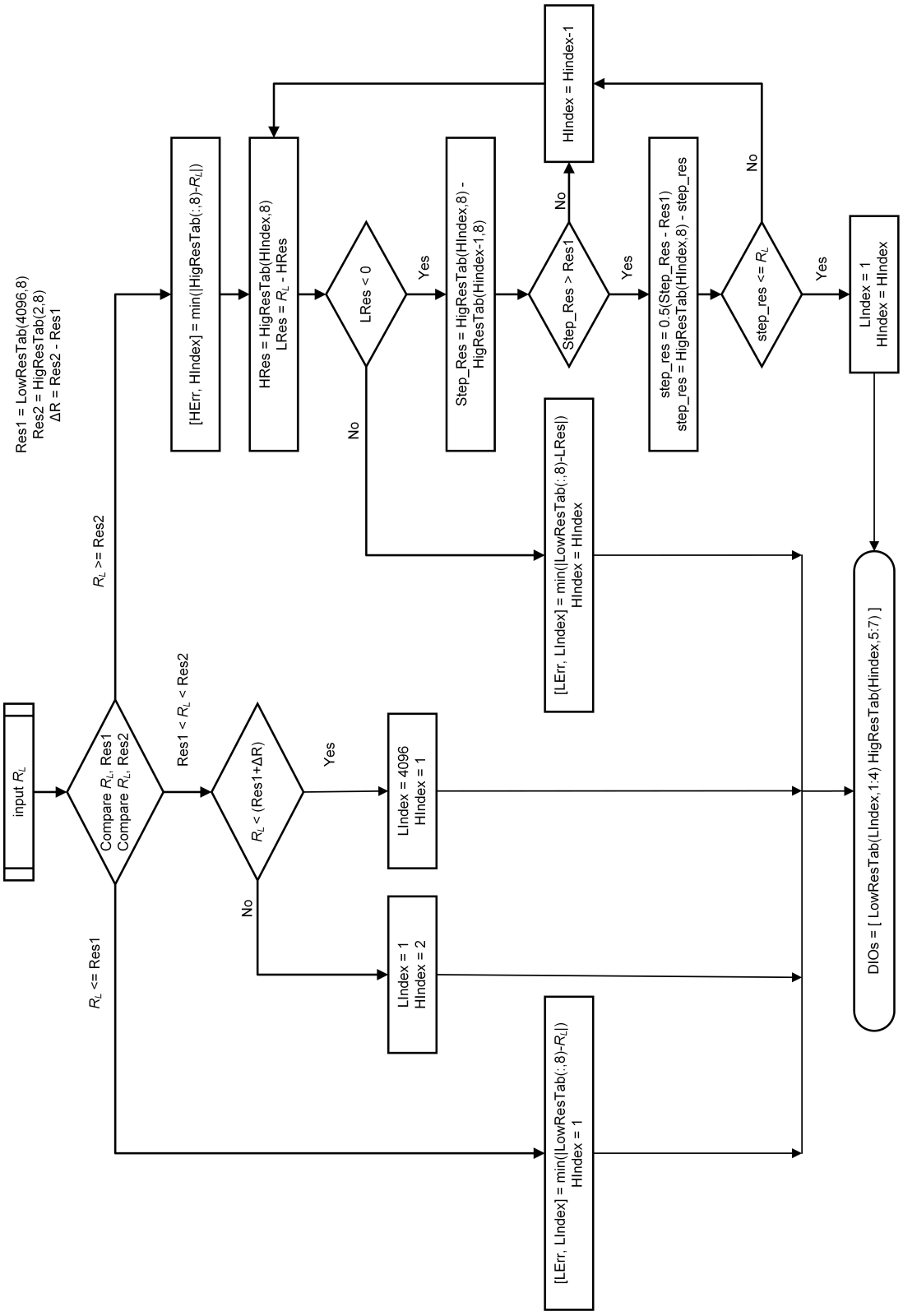

Figure B.2: Program flowcharts of the resistance box

Resistance range	0 ~ 2,084,775 Ω
Resistance step	1 Ω
Accuracy	<100 Ω: lower than 2% ≥100 Ω: lower than 1%
General data	
Operating time:	About 10 ms
Operating life:	1 million operations
Operating temperature:	0 ~ 30℃ (Best)
Power supply:	1.05 W
Dimensions:	280×200×135 mm
Weight:	0.5 kg
Interface type:	CP30 on DS1103 connecter panel (dSPACE©)

Figure B.3: Specifications of the programmable load resistance box

In addition, because the selected values of the resistors are not exactly equal to the theoretical values given in equation B.1, it is possible that the resistance box can not output the exact expected resistance R_L. However, using the table lookup method, the programmable system will select the closest resistance automatically, make sure the error between them is the minimum. It will also return the exact output value of the resistance box, which can be used to modified the experimental results finally.

Simple specifications of the programmable load resistance box are given in Figure B.3.